FUNCTIONAL NANOCOMPOSITE COATINGS FOR USE IN FOOD PACKAGING

A Thesis Project

presented to

the Faculty of the Polymers and Coating Science Department

California Polytechnic State University, San Luis Obispo

In Partial Fulfillment

of the Requirements for the Degree

Master of Science in Polymers and Coatings Science

By

Camden Webb

August 2023

COMMITTEE MEMBERSHIP

TITLE:	Functional Nanocomposite Coatings for Use in Food Packaging
AUTHOR:	Camden Neil Webb
DATE SUBMITTED:	August 2023
COMMITTEE CHAIR:	Shanju Zhang, Ph.D. Professor of Chemistry and Biochemistry
COMMITTEE MEMBER:	Dr. Erik Sapper, Ph.D. Associate Professor of Chemistry and Biochemistry
COMMITTEE MEMBER:	Dr. Ajay Kathuria, Ph.D. Associate Professor of Industrial Technology and Packaging

TABLE OF CONTENTS

List of Tables viii

List of Figures ix

Abstract xiii

Acknowledgements xv

1. Introduction 1

1.1. The Problem with Food Packaging 1

1.2. Biodegradable Polymers in Food Packaging 4

1.2.1. Polyesters 4

1.2.2. Polysaccharides 5

1.2.3. Functional Lipids and Proteins 8

1.2.4. Petroleum-derived 8

1.3. Composites 11

1.4. Nanomaterials 11

1.5. Nanocomposites 14

1.6. Active/Functional Nanocomposites 16

1.7. PVA/CNF/GO Nanocomposites for Food Packaging 17

2. Methods and Materials 20

2.1. Sample Preparation 20

2.1.1. Stock Solution Preparation 20

2.1.2. Liquid Sample Synthesis 23
2.1.3. Solid Sample Preparation 24
2.2. Basic Material Characterization 26
2.2.1. Thickness and Mass Testing 26
2.2.2. Polarized Optical Microscopy 26
2.2.3. Fourier-Transform Infrared Spectroscopy 27
2.2.4. Rheometry 27
2.2.5. Absorbance 27
2.2.6. Color and Gloss Testing 28
2.3. Thermal Analysis 28
2.3.1. Thermal Gravimetric Analysis 28
2.3.2. Differential Scanning Calorimetry 28
2.4. Mechanical Testing 28
2.5. Solvent Permeation 29
2.5.1. Water Vapor Transmission 29
2.5.2. Cobb Testing 31
2.5.3. Contact Angle Testing 31
2.5.4. Water and Oil Absorption 32
2.6. Oxygen Permeability 33
2.7. Microwave Testing 34

2.8. Bacterial Inhibition Testing 34

3. Results and Discussion 35

3.1. Sample Preparation and Solution Properties 35

3.1.1. Polarized Optical Microscopy 35

3.1.2. Fourier-Transform Infrared Spectroscopy 37

3.1.3. Rheometry 39

3.2. Structural Characterization 41

3.2.1. Fourier-Transform Infrared Spectroscopy 41

3.2.2. Absorbance 44

3.2.3. Color and Gloss Testing 46

3.2.4. Contact Angle Testing 48

3.3. Thermal Analysis 49

3.3.1. Thermal Gravimetric Analysis 49

3.3.2. Differential Scanning Calorimetry 53

3.4. Mechanical Testing 57

3.5. Solvent Permeation 61

3.5.1. Water Vapor Transmission 61

3.5.2. Cobb Testing 64

3.5.3. Water and Oil Absorption 66

3.6. Oxygen Permeability 68

3.7. Microwave Testing 72

3.8. Bacterial Inhibition 74

4. Conclusion 75

5. Future Work 77

6. Bibliography 79

List of Tables

Table		Page
1	Ratios of the solid content in each liquid sample……...	23
2	Sample composition with each stock solution……...	23
3	Oxygen permeation testing failure rate of each sample composition……	69
4	Water loss from boiling over 10 minutes at 10% microwave power…….	73

List of Figures

Figure		Page
1	Configuration of cellulose, hemicellulose, and lignin as part of a plant cell…….	7
2	The deacetylation reaction removes acetyl groups from chitin to form chitosan…….	7
3	Chemical structure for the repeat unit of poly(vinyl alcohol)……..	9
4	The hydrolyzation reaction is used to convert poly(vinyl acetate) to PVA……..	10
5	Some of the different dimensionalities of carbon, each having significantly different properties……...	12
6	Illustration of how filler particle shape relates to the tortuous path…….	13
7	Multicolored photoluminescent solutions using carbon nanodots……	15
8	Chemical structure of the repeat units for cellulose…….	18
9	Representation of the chemical structure of graphene oxide……	19
10	Graphene Oxide produced using the Hummer's method at three stages of the process, acid treating expanded graphite (a), oxidizing GO (b), and concentration through centrifuging (c)……..	21
11	Paper drawdown (a) and cast (b) nanocomposite samples……...	25
12	Dimensions (a) of the dog bone template (b) used for tensile testing…..	29
13	Determination of contact angle for water droplets using ImageJ…….	32
14	One of each weight boat sample composition prepared for oxygen permeation testing…….	33
15	Cellulose (a) and GO (b) aggregations at 20x magnification……...	35
16	Low-concentration cellulose stock solution at 5x magnification towards the beginning (a) and end (b) of sonication……..	36
17	High-concentration graphene oxide stock solution at 5x magnification towards the beginning (a) and end (b) of sonication……	36
18	Unconditioned PVA (a), CNF (b), and 1% GO (c) samples at 5x magnification……	37

19	FTIR spectra for each composition's solution. From top to bottom: PVA, CNF, 1% GO, 5% GO, and 10% GO……	38
20	FTIR spectra of control PVA in liquid, unconditioned, and conditioned form, indicating a loss in water content……	39
21	Rheometry profiles for each liquid sample solution…….	40
22	Changes in viscosity at low and high shear rate for each sample composition……...	40
23	FTIR spectrum for unconditioned dry PVA…….	41
24	FTIR spectrum for unconditioned PVA with CNF……...	42
25	FTIR spectrum for unconditioned dry PVA with CNF and 10% GO…..	43
26	FTIR spectrum for conditioned dry PVA with CNF and 10% GO……..	44
27	UV-vis spectra for each unconditioned sample composition……...	45
28	UV-vis spectra for each conditioned sample composition……...	46
29	CIELAB L colorimeter data for unconditioned and conditioned samples……..	47
30	Gloss data at 85° (a) and 60° (b) for unconditioned and conditioned samples……..	48
31	Contact angle of droplets on conditioned samples versus time……	49
32	TGA mass loss versus temperature profile for control PVA……	50
33	Percent mass at 200°C indicating water content in the samples after conditioning……..	50
34	Onset temperature (a) and midpoint (b) of the first degradation step…...	51
35	Overlayed TGA results displaying the difference in step profiles between each sample composition……	52
36	Onset temperature (a) and midpoint (b) of the second degradation step..	52
37	Percent mass of each sample composition at 375°C (a) and at 600°C (b)……..	53
38	Glass transition temperatures for each sample composition…….	54
39	Melting temperatures (left) and heating enthalpy of fusion (right) for each sample composition……..	55

40	Crystallization temperatures (a) and cooling enthalpy of fusion (b) for each sample composition……..	56
41	Change in melting temperature (a) and degree of crystallinity (b) as samples thermally degrade……	56
42	Elastic modulus/stiffness for unconditioned (a) and conditioned (b) cast samples……..	57
43	Ultimate tensile strength for unconditioned (a) and conditioned (b) cast samples……..	57
44	Percent elongation for unconditioned (a) and conditioned (b) cast samples……..	58
45	Elastic modulus/stiffness for each conditioned sample composition on paper……..	59
46	Ultimate tensile strength for each conditioned sample composition on paper……..	60
47	Percent Elongation for each conditioned sample composition on paper..	60
48	Average water loss for each sample composition over a period of 30 days……...	61
49	Average permeability calculated from the water vapor transmission rates……...	63
50	Easel paper substrate images at 5x of two types of holes (a and b) and a thinner section (c)…….	63
51	Cobb values representing water absorption for unconditioned paper samples……..	64
52	Cobb values representing water absorption for conditioned paper samples……..	65
53	Cobb values representing oil absorption for conditioned paper samples.	66
54	Average water absorption as a function of time in the first three hours...	67
55	Average water absorption for each sample composition after 24 hours...	67
56	Average oil absorption as a function of time in the first three hours (a) and absorption at 24 hours (b)……..	68
57	Oxygen transmission results for conditioned paper samples……..	69

58 Oxygen transmission results without thickness calculations.……... 70
59 Steady-state averages for oxygen transmission rate from 65 to 85 hours…….. 71
60 Oxygen permeation rates for conditioned samples accounting for sample thickness……... 72
61 Sample temperatures using the microwave at full power for 15 seconds. 73
62 Thermal conductivity versus oxidation level of graphene oxide at various lengths…….. 74
63 Final *E. Coli* (a) and *S. aureus* (b) petri dishes……. 75

Abstract

Plastics are a class of materials known for their cost and property advantages, increasing significantly in their usage worldwide. Unfortunately, these benefits come with an increasingly concerning environmental impact. A combination of inadequate disposal options and combinations of materials have led to environmental disasters that will impact generations. One of the worst areas for plastic waste is food packaging. Plastic as a material generally excels at durability and longevity, but as food packaging, it outlives its intended purpose by several orders of magnitude. This leads to plastic food packaging materials sitting in landfill or leading to the environment for hundreds of years. Because of this, there is a strong motivation to develop food packaging materials that are biodegradable, yet still maintain the properties that make plastic better than other classes of materials. Food packaging has many forms, but in general, the most important aspects are cost, mechanical, and oxygen and water barrier properties. To achieve an end-product that excels in these aspects, combinations of materials called composites may be developed. Nanocomposites are a subcategory of composites composed of a matrix material and nanomaterials, separate phases that interact with one another in a number of ways. This research is focused on increasing the mechanical and barrier properties of polyvinyl alcohol, the most commercially-viable biodegradable polymer. The nanomaterials used were graphene oxide (GO) and cellulose nanofibers (CNF) for mechanical and barrier reinforcement. Five sample compositions were produced: a control PVA, CNF, 1 wt% GO, 5 wt% GO, and 10 wt% GO, which were drawn down on uncoated paper and cast by themselves. Testing of these nanocomposites included oxygen transmission, mechanical, and thermal property analysis, and various solvent-interaction

testing including absorption of water and oil, Cobb testing, and water vapor permeation. With the addition of CNF and GO to PVA, there was an observed increase in barrier properties through a reduction of hydrophilicity and water absorption, and oxygen permeability.

Keywords: Poly(vinyl alcohol), food packaging, cellulose nanofibers, graphene oxide, barrier properties

Acknowledgements

I would like to first thank Dr. Shanju Zhang, my advisor and graduate coordinator. Dr. Zhang has provided me with invaluable educational experiences in the Polymers and Coatings program through his facilitation of courses and thesis/research work. His guidance, enthusiasm, and level of expertise have encouraged me and allowed me to achieve personal growth that was not possible without him.

Next, I would like to thank Dr. Erik Sapper and Dr. Ajay Kathuria for being on my thesis committee. Dr. Sapper has been highly influential in my time in the Polymers and Coatings program, specifically through his courses for surface chemistry and in the polymers series. While I had no courses with Dr. Kathuria, I learned a lot about barrier properties and characterization that have made this project possible. Both of these professors have been extremely approachable and accommodating during my time working with them and I am extremely grateful to have them on my committee.

Huge thanks to the Bill Moore Fellowship for their generous scholarship and funding of lab resources. I would also like to thank Cal Poly and the Department of Chemistry and Biochemistry. Finally, thank you to the Polymers and Coatings program and the Kenneth N. Edwards Western Coatings Technology Center.

I would also like to thank the Zhang research group for their assistance, support, and community provided during my time working with them. Specifically, Michael Friend, an incoming Polymers and Coatings student and Sudeep Louis, a now graduated alumnus of the program. Michael assisted greatly in the preparation of lab work and collection of data, and without him this project would not have been the same. Sudeep

was a great lab partner who jointly synthesized graphene oxide with me and often helped in the preparation of samples.

Next, I would like to thank Dr. David Zigler for his help regarding UV-vis spectroscopy and tips on analysis. I'd also like to thank Dr. Marie Yeung and her research student Jasmine Wu for their cooperation in bacterial inhibition testing.

Lastly, I would also like to thank the friends and family that supported me throughout my time at Cal Poly.

1. Introduction

1.1. The Problem with Food Packaging

Since their conception, plastics have been a material with a wide range of applications due to their wide range of material properties and cost of production. These benefits have made plastics see exponential growth since their conception, doubling in usage since 2000 [1]. Unfortunately, as plastics have increased in usage, more research on environmental impact of materials has been done that indicates plastics as they are used currently are not sustainable in the long-run. This provides a drive to develop plastics from more renewable sources and a focus on the environmental impact of the entire lifecycle of materials. In the case of plastics, petroleum-based synthesis and century-long environmental degradations are typical and carry many issues on their scale of use [2]. The largest issue plastics have in the consumer world is the fact that most plastic packaging outlives its purpose. For example, a plastic bag from the grocery store is strong enough to hold groceries, prevents liquid from getting everywhere through condensation or spills, and is cheaply manufactured, but vastly outlives its lifetime usefulness. Once a plastic bag is done transporting groceries, it typically gets thrown away and sent to landfill to decompose over a period of hundreds of years.

In terms of materials outlasting their purpose, there are few better examples than the food packaging industry. In most cases, plastics designed to hold perishables do not need to last longer than a month at most while plastics can take hundreds of years to decompose [2]. This durability issue alongside the sheer scale of the food industry led to large amounts of single-use plastic waste, packaging materials accounting for 45 percent of landfill waste in the US in 2018 [3]. Food packaging in general takes many forms and

has a range of material requirements depending on the specific food item and needs for shelf-life, transportation, and presentation. In all cases food packaging needs to be food safe, not leaching harmful chemicals or causing illness. Properties such as strength, stiffness, chemical resistance, and water repellence can vary by a lot depending on the application. For example, some produce like cucumbers may be encased in a film while strawberries may be put into hard plastic baskets. The cucumber has enough structural integrity to not get bruised without assistance from the packaging but will degrade quickly if exposed to high moisture. Conversely, strawberries are much softer and will bruise easily, but can tolerate higher moisture. What this means for the development of food packaging is that depending on the needs of the application, many different materials and combinations of materials can be considered.

The two most important material properties in food packaging are mechanical and resistance to oxygen and water permeation. Mechanical properties include strength, toughness, stiffness, etc. and translate to how the material reacts to external forces. Oxygen and water permeability refers to the material's ability to block out air and water and is also referred to as barrier properties. These properties, alongside cost and ease of manufacturing are why plastic is the ideal modern material for most food packaging applications. Unfortunately, more sustainable plastics typically lack decent properties in one or both of these two main requirements in addition to higher cost [4].

A life cycle analysis of most plastic products includes environmental impact at all stages of its life – from "cradle to grave" and use production, shipping, use, and disposal to determine by-products, emissions, and waste. The chronological life of a plastic product can be categorized into synthesis, manufacturing, work life, disposal, and

optionally recycling. Synthesis refers to the polymerization process, which uses solvents, monomers, initiators, catalysts, etc. and can also be referred to as primary processing. As most plastics are synthetic, they typically start as a byproduct of the petrochemical industry [5]. For plastics that are not synthetically produced, they may be sourced naturally, for example starch from potatoes and corn to make thermoplastic starch [6]. After synthesis, manufacturing for polymers can be varied significantly as there are many ways to make different products. Examples of this include continuous processes such as extrusion and rolling, and non-continuous processes including molding and casting. Sometimes synthesis and manufacturing happen at the same time such as the case of UV-cure polymers and plastics with fast reaction times. After manufacturing, the product experiences its useful life as whatever role the product is supposed to take. This step is more relevant to larger and more complex systems such as cars, which have associated needs during their useful life such as gasoline, oil, replacement wheels, etc. For plastic products, this could include cleaning or protecting agents, but in most cases includes very little to nothing. Finally, disposal involves the processing and waste materials associated with the end of the product's life. If the product at the end of disposal can be reused or recycled, any environmental impact "saved" over using newly synthesized material can be subtracted from the overall environmental impact of the product [7].

Unfortunately, most plastics are not recycled for a few reasons. For the average consumer, recycling plastic materials is mostly limited to poly(ethylene terephthalate) (PET), high-density polyethylene (HDPE), and sometimes polypropylene (PP) [8]. PET is commonly used in water bottles, HDPE in milk jugs, and PP in solid food containers. These plastics can also only be recycled when they are in pure form, typically without too

many additives or combined into layered or composite forms. Other plastics or even composite materials including the plastics mentioned may require specific commercial processes that are not realistic to deploy in residential recycling facilities [9]. This general life cycle of course does not include every step a product might take, especially transportation, but for the purpose of material comparison, extra steps such as transportation most often matter significantly less than the ones listed above as they somewhat cancel each other out and their relative scale in terms of environmental impact per unit is magnitudes smaller than production and disposal [7].

Other issues with synthetic synthesis include the price of plastics being tied with the oil market. This is the case as oil is a finite resource and even byproducts of other processes have value. As oil becomes scarcer, the costs of plastics will increase until they are no longer commercially viable [10].

1.2. Biodegradable Polymers in Food Packaging

1.2.1. Polyesters

There are several classes of polymers being used and developed for degradable food packaging, each with their own benefits and associated issues. First, polyesters are a large class of polymers that may be produced using either natural or petroleum-based sources. Natural sources can include biomass and they may even be produced using microorganisms. Polyesters are good for environmental degradation as ester groups break down through a process of hydrolysis, a group of chemical reactions where water pulls apart larger molecules [11]. One such degradable polyester is the aliphatic poly(butylene succinate) (PBS), produced using succinic acid and 1, 4 butanediol, two renewable chemicals obtainable through biological routes [12], [13]. In general, aliphatic polyesters

display properties beneficial for liquid-containing bottles, being odorless and degrading within two months in the environment [14]. Some polyesters struggle with maintaining mechanical properties high enough to be useful.

Another type of degradable polyester is polyhydroxyalkanoates (PHAs). PHAs are typically produced through bacterial fermentation in nature and can have a wide range of properties depending on the specific monomers produced [14]. Several studies have been conducted using food waste as a bacterial feed to produce PHAs to form food packaging films, but difficulties in scaling and high cost prevent PHA from being widely used today [15].

Finally, poly(lactic acid) (PLA) is one of the most popular renewable polymers used today, mostly for its desirable low cost and mechanical properties [16]. PLA has seen a lot of success in 3D printing due to these benefits, but also due to the relatively low thermal transitions which make heated extrusion easier. Conversely, food packaging application of PLA is difficult due to the brittle nature and low thermal resistance of the polymer. Because of this, new copolymers incorporating aliphatic polyesters and other renewable polymers are being produced that improve ease of manufacture, mechanical, and thermal properties. The combination of the strong yet brittle PLA and weak yet ductile polymers can produce copolymers with superior toughness, an indication of high strength and ductility [17].

1.2.2. Polysaccharides

Another class of renewable polymers that are useful in food packaging is polysaccharides. This class of polymers excel in cost, biodegradability, and biocompatibility, while typically struggling with hydrophilicity and barrier properties.

Commonly used sources for polysaccharide-based polymers are starch, cellulose, chitin, chitosan, and pectin. Polysaccharide polymers use monosaccharide monomers, meaning it is extremely easy to synthesize products that degrade in the environment and importantly do not form other environmental hazards in the process of degradation.

Starch is highly hydrophilic due to the abundance of hydroxyl groups present in its chemical structure. This means binding to the also hydrophilic paper and cardstock is easy, especially with the assistance of water. Starch has seen a lot of success in food packaging and even single-use dinnerware in the form of thermoplastic starch [18]. Unfortunately starch polymers typically struggle with barrier properties without copolymerization or other additives [19].

Cellulose is derived from plant cells alongside hemicellulose and lignin (Figure 1). These three compounds are among the cheapest naturally produced polysaccharides, sourced from any plant material. There has been a lot of research specifically behind the surface functionalization and cross-linking of cellulose-based films to reduce hydrophilicity and improve barrier properties [20].

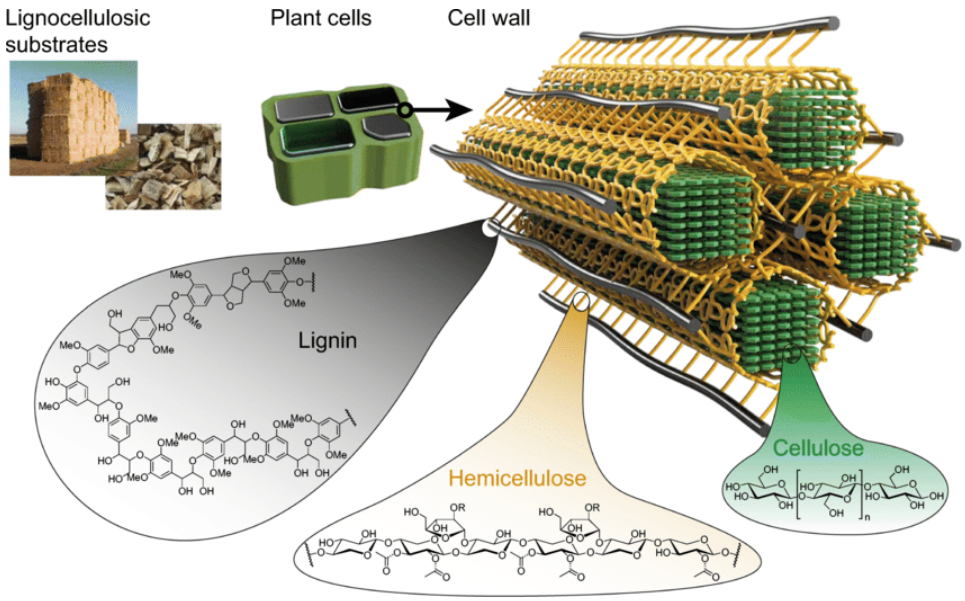

Figure 1. Configuration of cellulose, hemicellulose, and lignin as part of a plant cell [21].

Chitin and chitosan are also interesting polymer sources, being the second most common carbohydrate polymer after cellulose [22]. It can be sourced from crustaceans, insects, fungi, and spiders, and has many uses already in the food industry outside of packaging. Chitosan is simply chitin that has gone through a process called deacetylation, which removes most of the acetyl groups in an elimination reaction (Figure 2). Chitin and chitosan are already used as an additive to supplement fiber and maintain freshness of meaty flavors [23].

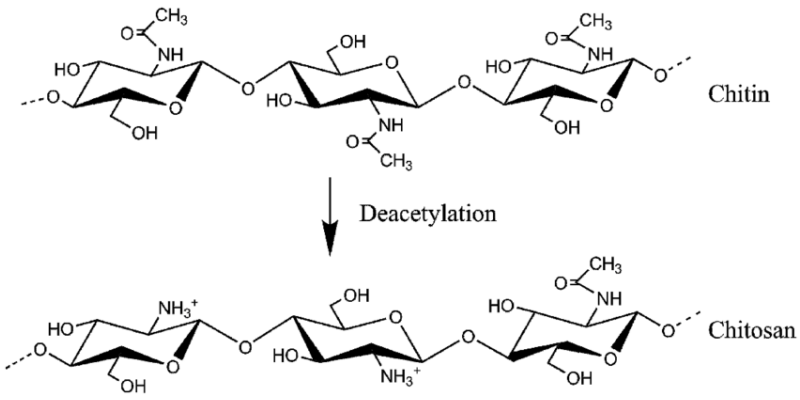

Figure 2. The deacetylation reaction removes acetyl groups from chitin to form chitosan [24].

1.2.3. Functional Lipids and Proteins

As lipids and proteins are naturally a part of the environment, their degradation is ensured and harmful degradation products are not present. General properties for lipid-based coatings are excellent hydrophobicity and barrier properties, but lackluster mechanical properties [25]. Popular lipid-based coatings are beeswax and carnauba wax, beeswax being sourced from beehives and carnauba wax being sourced from the leaves of the carnauba palm tree [26]. These two waxes contain a high percentage of esters from fatty acids, making them easily degraded in the environment.

Casein polymers are an interesting example of protein-based materials that degrade extremely well in the environment. This type of polymer is one of the oldest adhesives and is formed by the simple addition of acid to milk. The two main types of proteins in milk are casein and whey, casein being a class of many similar proteins that react to changes in acidification of the milk . Casein polymers can be produced through the use of a dilute form of formaldehyde called formalin, citric acid, acetic acid, or many other acids. They can also be produced by simply allowing milk products to go bad as bacteria convert the lactose into lactic acid. Generally, casein polymers struggle from poor mechanical properties and high cost [27].

1.2.4. Petroleum-derived

While not as ideal in terms of environmental impact, there are some petroleum-based polymers that perform well on an industrial scale that are also biodegradable. While these materials are a good step towards fully renewable food packaging. In general, oil-derived polymers exhibit better associated costs, and mechanical and barrier properties. Some petroleum-based biodegradable polymers include poly(butylene

adipate-co-terephthalate) (PBAT), polycaprolactone (PCL), and poly(vinyl alcohol) (PVA).

PBAT contains many ester groups, which facilitate the environmental degradation of the polymer. PBAT has the benefit of manufacture ease due to its synthetic origin and high flexibility. These factors along with cost lead to PBAT being one of the most promising future food packaging materials.

Another interesting degradable polyester is polycaprolactone. PCL is typically synthetically produced using petroleum products, but it makes up for this in its excellent biodegradability and chemical resistance. PCL is on the cheaper side of degradable polymers and has a very low melting point of around 60°C, which makes manufacturing PCL desirable, but applications in food packaging limited.

Finally, PVA is another biodegradable synthetic polymer. PVA has by far the most simplistic chemical formula of the polymers listed, being composed of a hydrocarbon chain and an alternating hydroxyl group (Figure 3). PVA does not contain an ester group like many of the other biodegradable polymers, but the degradation through hydrolysis still works as there are so many available hydroxyl groups.

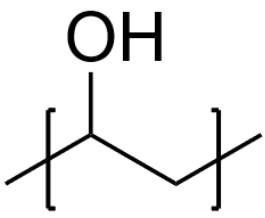

Figure 3. Chemical structure for the repeat unit of poly(vinyl alcohol).

PVA is one of the best biodegradable polymers for the application of food packaging due to its excellent film formation and relative cost but has several common issues for practical use. The main issue associated with PVA is its sensitivity to water in

both liquid and vapor forms. Due to the abundance of hydroxyl groups, the polymer itself is quite hydrophilic, which allows water into the bulk of the material. This has a large negative impact on mechanical and barrier properties, essentially restricting its use to low-moisture foods. With the issue of hydrophilicity taken out of consideration, PVA has comparable mechanical and barrier properties to conventionally used polymers such as polystyrene (PS) and poly(ethylene terephthalate) (PET) [28].

PVA is produced through a hydrolyzation procedure performed on poly(vinyl acetate), a structurally similar polymer with an alternating acetate group instead of a hydroxyl group (Figure 4). Through this procedure it is possible to obtain different purities of PVA, where the reaction did not happen for a percentage of the acetate groups. This can also impact the polymer's overall material properties through the interruption of crystalline regions.

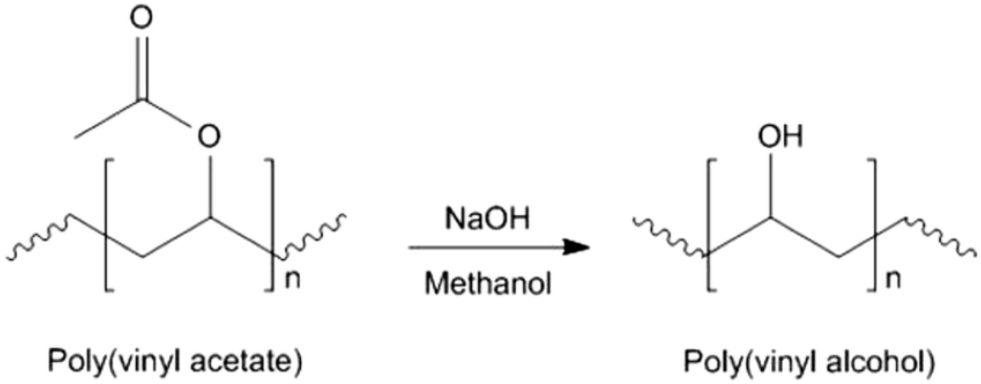

Figure 4. The hydrolyzation reaction is used to convert poly(vinyl acetate) to PVA [29].

Some food packaging developments with PVA are the incorporation of crosslinks to reduce the available hydroxyl groups and composites using PVA as a matrix material.

1.3. Composites

Composites describe a class of materials involving a combination of two or more significantly different materials, typically synthesized to improve properties or performance of the final product. One requirement of composites is that the materials combined form distinctly separate phases within the combined material. This means given a cross-section or other analysis it would be apparent there were different materials and/or structures that perform different roles. Composites have many uses in the modern world such as improving mechanical performance and decreasing costs. An example of this is carbon fiber reinforcement of epoxies, composites that with the combination of epoxy as a matrix material and carbon fibers, exhibit extraordinary mechanical properties exceeding steel while also maintaining low weight [30]. Without the combination of these two materials, neither would be able to replace steel as the sum is greater than the parts.

There are many types of composites depending on intended use. One subclass is nanocomposites, which combine a nanomaterial with a matrix material, typically a polymer. These can work in similar ways to regular composites, increasing mechanical, thermal, electrical, etc. properties without sacrificing cost and form-factor.

1.4. Nanomaterials

Nanomaterials refer to material with at least one dimension on the nanoscale (smaller than 100 nanometers). There are many types of nanomaterials that are generally divided into groups of chemical composition and dimensionality. Chemical compositions for nanomaterials include metals such as iron and copper nanoparticles, carbon in the form of fullerenes, carbon nanotubes, and graphene, and other materials such as silica and

clay. Dimensionality describes the specific shape of the nanomaterial as either 0D, 1D, or 2D. Figure 5 illustrates the difference of dimensionality on nanomaterial shape.

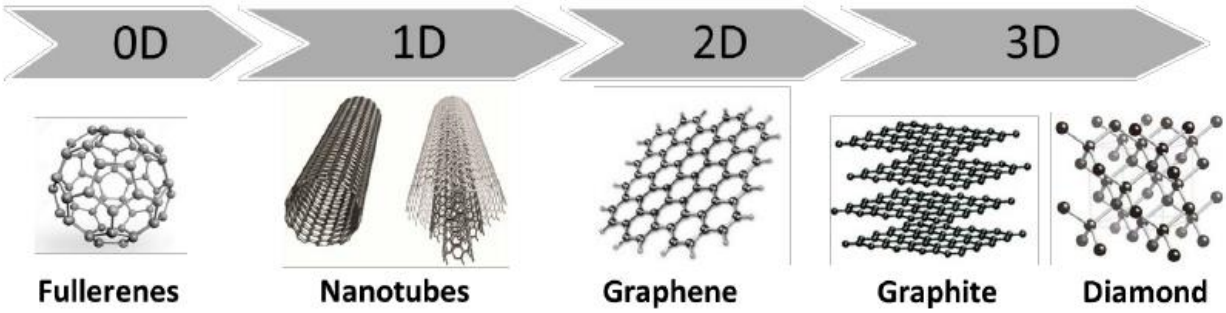

Figure 5. Some of the different dimensionalities of carbon, each having significantly different properties [31].

0D nanomaterials, also known as nanoparticles, are materials that have three dimensions on the nanoscale. They are typically used for their chemical reactivity and optical abilities but have many other uses depending on their chemical composition [32]. Commonly used nanoparticles include metals, metal oxides, ceramics, and fullerenes.

1D nanomaterials have two dimensions on the nanoscale and are typically used for the purposes of increasing electrical and mechanical properties. Nanocomposites with 1D nanomaterials can display much higher strength and stiffness than the bulk matrix material by itself. This is because within the composite, the nanofiller acts as fiber-reinforcement, similar to that seen with carbon fiber. In this case, the nanomaterial uses interfacial forces between itself and the matrix material to improve mechanical performance [33]. Important 1D nanomaterials include carbon nanotubes (CNTs) and cellulose nanofibers (CNF).

2D nanomaterials have only one dimension on the nanoscale and are most commonly used to increase barrier and mechanical properties, but also have uses in

electrical and thermal applications. Mechanical properties typically increase to a lesser degree with 2D nanomaterials as opposed to 1D nanomaterials, but the interfacial force mechanism is the same. Barrier properties in 2D nanocomposites can be increased through a mechanism known as tortuosity or tortuous path. Tortuosity essentially describes the difficulty of which permeants face as a result of physical travel distance [34]. Figure 6 displays three different tortuosities of varying levels based on filler particle shape. It is important to note that the physical thickness of films does not change the tortuous path, rather it is a function of how well additives increase travel length. Important 2D nanomaterials include graphene sheets, silicene (a two-dimensional silicon sheet), and nanoclays[35], [36].

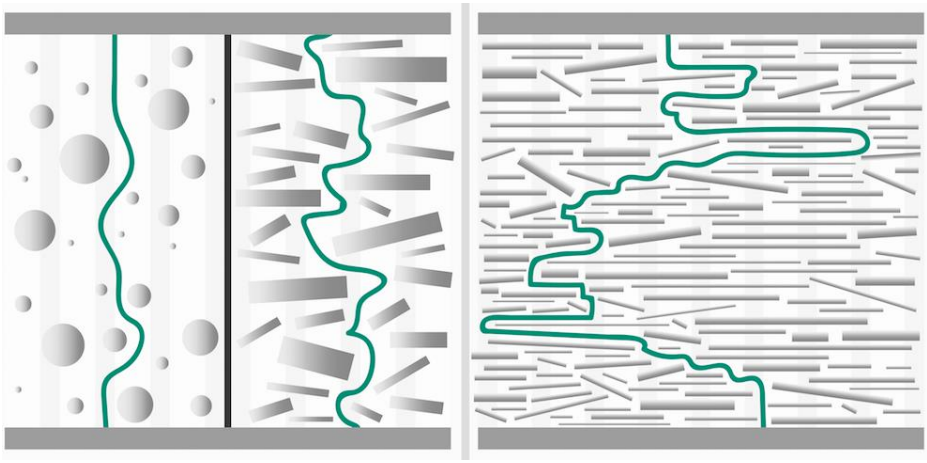

Figure 6. Illustration of how filler particle shape relates to the tortuous path [37].

Nanomaterials are of particular interest to the scientific community as with the scaling of material size, properties can change significantly. For example, iron in a large scale hardly flammable, but on the nanoscale can combust when sprinkled in the air and even inert metals such as platinum can catalyze reactions on the nanoscale [38].

1.5. Nanocomposites

As the name implies, nanocomposites are composites incorporating the use of nanomaterials. Many nanocomposites already have been used in all sorts of fields, but new discoveries are being made all of the time. Food packaging is an interesting application of nanocomposites as the health implications for many nanomaterials are still not fully understood. Considering the increase of interest in renewable materials and the concurrent rising interest in nanomaterials, the two come together to produce some interesting results.

Starting with 0D nanocomposites, the vast majority of nanomaterials currently in use are 0D for the purpose of catalyzing chemical reactions and enhancing coatings. For chemical reactions, the usefulness mostly lies in the higher surface area, allowing for higher levels of efficiency and reactivity. This, however, is not an example of a composite. For nanocomposites, paints and coatings use 0D nanoparticles for color and other optical effects. This can work through several different mechanisms including absorption and scattering of specific wavelengths of light, changing general transparency, and altering observed surface finish [39]. When used in this manner, nanomaterials are sometimes called nanopigments. Nanopigments can work through either reaching specific particle sizes, reaching the size of specific wavelengths of light or through other mechanisms such as photoluminescence [40]. For photoluminescence, specific emissions of light can be controlled through the absorption of photons. Using 0D carbon nanodots, paints can be developed that exhibit large photoluminescent reactions to UV and visible light in a way that doesn't harm the environment, while still being just as mass-producible as conventional photoluminescent dyes (Figure 7) [41].

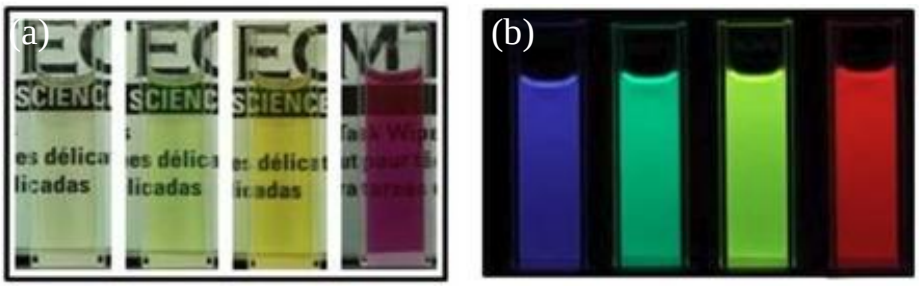

Figure 7. Multicolored photoluminescent solutions using carbon nanodots [42].

Although they currently are used less frequently than 0D nanomaterials, 1D nanomaterials have seen a lot of recent interest in the field of nanocomposites, mostly for their use in mechanical reinforcement. As a filler, 1D nanomaterials such as cellulose nanofibers (CNF) or carbon nanotubes (CNTs) may be added for this purpose. 1D nanofiller acts on the nanoscale similarly to how rebar works in concrete, increasing overall tensile strength through the transfer of force from the concrete to the steel. This idea of interfacial force transfer applies to 1D nanocomposites in the same way, just on a smaller scale. The addition of this nanofiller can increase strength and toughness of the nanocomposites to be able to compete with or outperform other materials. Depending on the application, lower amounts of material can be used as the performance to weight ratio changes, or materials can be changed to follow secondary manufacturing goals [43].

2D nanomaterials may also be used to increase mechanical properties in composites, but additional uses in enhancing barrier properties make their application different. 2D nanomaterials such as nanoclays and graphite have been used in the past to enhance mechanical and barrier properties. For mechanical properties, the same concept of force transfer between the matrix material and the nanomaterial applies. Considering the barrier properties, tortuosity can be massively increased when plate-like samples are introduced. As both of these composite changes impact properties that significantly

concern food packaging, the use of 2D nanomaterials has been explored previously. For example, nanoclays are food-safe and ecologically friendly nanoparticles that can be produced using relatively low-cost processes. Unfortunately, actual application of nanoclay into most polymeric materials is difficult as there are difficulties with dispersion and incorporation [44]. Other uses of 2D nanomaterials can include unmodified graphene for the purposes of improving electrical and thermal properties. Graphene sheets have extremely high electrical and thermal conductivity values, which transfer to nanocomposites including substantial loading. Several issues with graphene in general are the scaling of production and associated costs [45].

1.6. Active/Functional Nanocomposites

Active nanocomposites describe composites utilizing nanofiller as an antioxidant, antimicrobial, and/or antifungal agent. Typically, this is most useful for films or coatings as especially in the context of food packaging, a surface with no coverage doesn't protect food. Often additives such as clove essential oil can be added as a natural antimicrobial agent, but so can metal nanoparticles. This greatly reduces all forms of fouling a product may experience throughout its lifetime [46]. One application of metal nanoparticles is Au- TiO_2 in an algae-based film. It was concluded that the nanomaterials increased the antibacterial ability by 60% and 50% against *S. aureus* and *E. Coli*, respectively. Additionally, the hydrophilicity of the film changed by 34 degrees in a contact angle test, further increasing other properties of the film. This development for algae-based films transformed the extremely limited matrix material into something that could actually be used [47]. Another study focused on the addition of Ag-Cu nanoparticles to guar-gum films. In addition to stark differences in microbial activity, the barrier, thermo-

mechanical, and UV-resistance properties all improved. The results of this study indicated a proper active packaging material could be synthesized using these nanoparticles that would protect UV-sensitive foods [48].

1.7. PVA/CNF/GO Nanocomposites for Food Packaging

Considering the potential PVA films have if the problems with hydrophilicity and mechanical properties are addressed, PVA may be a good step towards a fully sustainable future for food packaging. To do this, cellulose nanofibers and graphene oxide could be used to make nanocomposites with PVA as the base. PVA is a synthetically produced polymer that biodegrades quickly and has appropriate base properties and associated cost that make it satisfactory for use in food-safe composites. PVA easily dissolves in water, so any additives would be best chosen to also disperse in water readily.

Cellulose nanofibers would be primarily added to increase strength as they are a 1D nanomaterial, but also to decrease hydrophilicity by occupying some of the hydroxyl groups of the PVA. Figure 8 displays that the structure of cellulose is composed of repeat units of D-glucose, condensed and connected in a chain. From the amount of oxygen present in the structure, hydrogen bonding between both PVA and water is achievable. This means both PVA and CNF can exist in liquid sample concurrently and the finished product sans water should include hydrogen bonding between the polymer and nanofiller. CNF is extremely biodegradable and bio-safe as cellulose itself is naturally produced by all living plants [49].

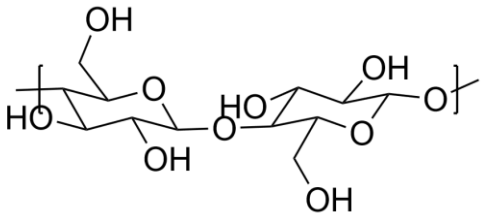

Figure 8. Chemical structure of the repeat units for cellulose.

Graphene oxide (GO) is another nanomaterial that would likely improve the properties of PVA through its 2D dimensionality and abundance of hydroxyl and carbonyl functional groups. As it is 2D, it should provide a lower level of mechanical enhancement when compared to the 1D CNF due to the difference in aspect ratio, the ratio of length to width. A representation of the chemical structure can be seen in Figure 9. The plate-like dimensionality of GO should assist in increasing tortuosity of the material, increasing the path length permeants have to travel through the material. The hydroxyl and carbonyl groups should decrease the hydrophilicity of PVA in the same way as CNF, by occupying the hydroxyl groups with hydrogen bonds. GO is produced through several methods, the most currently popular being the Hummer's method. Through this method, graphite can be converted into graphene oxide through a long series of steps. Due to the difficulty, dangerousness, and long reaction time, producing graphene oxide is expensive and not environmentally friendly. Fortunately, the production of graphene oxide can be scaled using different oxidizing agents and improving/modifying the Hummer's method to suit large-scale production [50]. Interestingly, different levels of oxidization can be used to obtain different properties, which can also change the requirements for the production method in a bulk setting. Curiously, this has also caused a lack of standardization in manufacturers for GO [51].

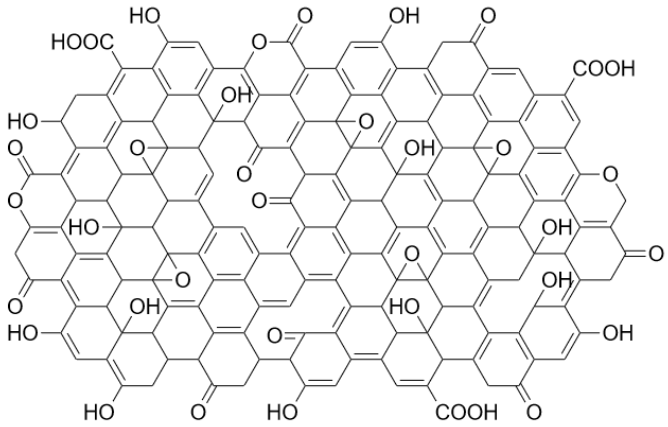

Figure 9. Representation of the chemical structure of graphene oxide.

The motivations for combining PVA with these two nanomaterials are produce a food-safe nanocomposite film or coating that maintains high mechanical and barrier properties, even when exposed to water, and to determine any interaction between 1D and 2D nanomaterials within the matrix. PVA was chosen as the base matrix material as aside from its decline in useful properties when exposed to water, it is the most commercially viable biodegradable polymer for the purpose of food packaging owing to its synthetic origins and associated low costs. In the scheme of things, any step towards biodegradability and true renewability is a step forward towards a greener future, even if the material is not renewably sourced. CNF was chosen as a 1D nanofiller material as cellulose is abundant in nature and degrades easily through environmental and biological means. GO was chosen as the 2D nanofiller due to its dimensionality and its recent interest in the scientific community. As the impact of CNF to polymers is relatively well-known, varying GO loading would provide a more novel focus to the food packaging research development. Even considering the swapping of materials for this type of nanocomposite, the observations and trends noted may be applied to other hybrid 1D and 2D nanocomposites.

2. Methods and Materials

2.1. Sample Preparation

2.1.1. Stock Solution Preparation

In order to prepare the five solutions with varying amounts of PVA, GO, and CNF, stock solutions of the three must be prepared to then distribute out for the finished liquid samples. In a typical process, graphene oxide was prepared using a modified Hummer's method, starting with graphite, then reacting to form expanded graphite, and finally graphene oxide. The Hummer's method involves first treating 5g of Acros Organics graphite flakes with a mixture of 150 mL 98% sulfuric and 50 mL 70% nitric acid in a stirred ice bath, then stirred for 24 hours. 1000 mL DI water was then added, and vacuum filtration was used to separate the acid-treated graphite flakes. DI water was added and filtered out until the pH of the rinse was around five. The graphite flakes were then dried in an oven at 60°C for 24 hours after being washed with acetone. To make expanded graphite, the acid treated graphite was then placed in a tube furnace set to 1000°C for 15 seconds. The five grams of expanded graphite was then added to 300 mL sulfuric acid, 4.2g potassium persulphate, and 6.2g phosphorous pentoxide. The mixture was then placed in an oil bath at 80°C for five hours. The mixture was then added to 1000 mL DI water and vacuum filtered. Again, the addition of water and filtration was repeated until the pH was around five. The expanded graphite was then set to dry in an oven for 72 hours at 100°C. Next, one gram of expanded graphite was added to 200 mL 97% sulfuric acid alongside 15g potassium permanganate in a large round-bottom flask, where the color changed from black to dark green. A mechanical stirrer was then set up and the round bottom was placed in another oil bath at 45°C. The reaction was then run

until the mixture changed from green to reddish-brown, taking approximately 24 hours. The mixture was then resuspended in 1000 mL DI water and 5 mL 30% hydrogen peroxide was added dropwise to change the color to a gold/orange color. At this point, the mixture contained oxidized expanded graphite. An Eppendorf 5810 centrifuge was then run with 35 mL of the mixture at 10,000 RPM for 90 minutes and the precipitate was collected. Once all of the mixture was processed, 500 mL DI water and 5 mL HCl was added to the precipitate and mixed until homogenous. Finally, the mixture was spun in the centrifuge at 7000 RPM until separation, where the supernatant liquid would be pulled out and DI water would replace the liquid volume taken out. Each vial was sonicated using the tip sonicator to redisperse the precipitate. This process was repeated until the pH was at or greater than five, with a final color change from yellow to black.

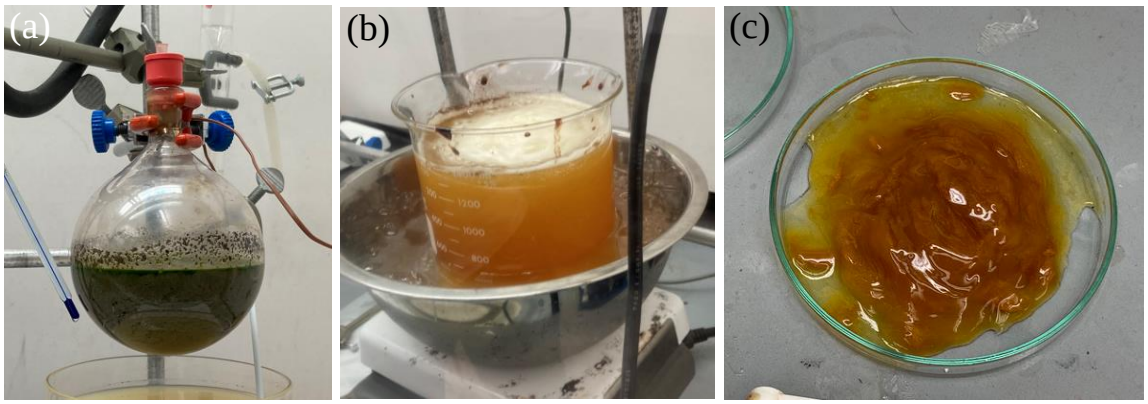

Figure 10. Graphene Oxide produced using the Hummer's method at three stages of the process, acid treating expanded graphite (a), oxidizing GO (b), and concentration through centrifuging (c).

The stock solution for PVA was prepared by dissolving 50 g 98-99% hydrolyzed high molecular weight PVA (Alfa Aesar CAS number 9002-89-5) in 500 mL DI water in a large beaker with stir bar. The PVA was first allowed to hydrate for 15 minutes, then the beaker was placed in a water bath at 80°C and ran for approximately two hours until much of the PVA had gone into solution. Occasionally a steel spatula was used to scrape

down the sides as the viscosity increased and to break up large chunks. Once the solution was having trouble stirring due to the viscosity increase, the solution was passed through a 100-micron mesh filter into two jars while still hot. The jars were then left to cool with their tops mostly closed, then placed in the refrigerator to avoid any mold issues. After cooling, a solid content test was performed to determine the water content in the stock solutions.

The stock solution for cellulose nanofibers was prepared by first grinding 1 g Acros Organics microcrystalline cellulose nanofibers with average particle size of 50 micron with a mortar and pestle for two minutes until fine. Next, the grinded CNF was added to 40 g DI water in a large vial. The vial was then sonicated in an ice bath with a tip sonicator for approximately an hour. At this stage, the cellulose was only metastable, sinking to the bottom if left overnight. The solution was then tested using a solid content test, then diluted with DI water to 0.055 wt% into several vials. Following that, the diluted solutions were then sonicated for four hours using a tip sonicator in an ice bath, monitoring the de-clumping of aggregations every 30 minutes.

Solid content tests were performed for each stock solution by weighing out an aluminum dish and adding between two and three grams of solution. The aluminum pans were then weighed and transferred to an oven at 110°C for an hour, then finally reweighed. To determine solid content of the solutions, the solid mass of the sample was divided by the liquid mass after subtraction of the pan. Solid content tests indicated the stock PVA sample was at 9.920 wt% PVA, the stock CNF sample was 0.055 wt%, and stock GO solutions were between 0.5 – 0.9 wt%.

2.1.2. Liquid Sample Synthesis

Five samples were synthesized for this project: control PVA, CNF, 1 wt% GO, 5 wt% GO, and 10 wt% GO. The PVA sample contained only PVA and DI water, the CNF sample contained PVA, CNF, and DI water, and the 1-10% GO samples contained PVA, CNF, DI water, and varying amounts of GO (Table 1). Final liquid samples were prepared using the solid content data from the stock solutions to determine the required amounts of each solution, accounting for different densities of each solution. DI water was used to maintain a common total solid weight percentage at 4.10 wt% (Table 2).

Table 1. Ratios of the solid content in each liquid sample.

	PVA	CNF	GO
PVA	100	0	0
CNF	99	1	0
1% GO	98	1	1
5% GO	94	1	5
10% GO	89	1	10

Table 2. Sample composition with each stock solution.

	Stock PVA (9.920 wt%)	Stock CNF (0.055 wt%)	Stock GO (0.686 wt%)	DI Water
PVA	16.74 g	0.00 g	0.00 g	21.60 g
CNF	16.74 g	0.75 g	0.00 g	20.86 g
1% GO	16.57 g	0.75 g	2.40 g	18.64 g
5% GO	15.90 g	0.75 g	11.50 g	10.28 g
10% GO	15.06 g	0.75 g	21.97 g	0.90 g

After combining the stock solutions, each sample was vigorously shaken for a few minutes, then tip sonicated for increasing amounts of time until few aggregates were seen with the polarized optical microscope. Following any period of inactivity, samples were placed in the vortex mixer to ensure even distribution.

2.1.3. Solid Sample Preparation

Solid samples were prepared using several methodologies, each with a different purpose. Samples intended for water vapor permeation, Cobb, microwave, and contact angle testing were drawn down on paper. The paper used was uncoated Creatology MSPCI easel paper intended for art purposes, so it was minimally processed and had no coating. Drawdowns are typically a simple preparation technique, but it was discovered that performing them on wet paper yielded more consistent thicknesses and textures throughout the sample. First, a good section of paper where there were no obvious defects was cut out and the alignment of the fibers was noted. Packaging tape was used to laminate the edges of the easel paper, then scissors were used to cut to the paper to account for some of the expanding as water was introduced. DI water was sprayed onto the surface and was spread lightly with gloved hands to fully saturate the paper. The water was left to soak into the paper for approximately a minute, then dabbed up until wet, but no longer shiny. From there, scotch tape was used to secure the edges of the now expanded paper and ensure the surface was sufficiently flat. After all of that preparation, a 15-mil drawdown bar was used to deposit the liquid sample in the same direction as the paper's fibers and it was left to dry overnight at 25°C. The finished product was then marked for areas of high uniformity (Figure 11a) and samples were cut.

Samples intended for FTIR, water and oil absorption, thermal, and mechanical testing were prepared by simply casting four grams of liquid solution into a weigh boat and storing in a covered room temperature environment. Figure 11b displays the cast samples organized by composition from CNF at the top to 1, 5, and 10% GO samples going down. Samples for color and gloss data were made using the standard 6-mil drawdown bar on BYK black and white color paper and left to dry overnight at 25°C.

Figure 11. Paper drawdown (a) and cast (b) nanocomposite samples.

Some samples were conditioned in an oven at 110°C for three hours. The paper samples were secured using glass plates and microscope slides to prevent them from folding in on themselves and being hard to work with. Conditioning was necessary to ensure all samples had equal amounts of water content, which can influence barrier and mechanical properties in PVA significantly [52]. After conditioning, plastic bags and desiccant were used to keep the water content from increasing.

2.2. Basic Material Characterization

2.2.1. Thickness and Mass Testing

Thickness of samples was determined using a digital Starett 734 micrometer for both paper and cast samples. Mass testing was performed by simply cutting out large sections of the uncoated paper and determining a mass per square area. Through these tests, it was concluded that the paper was on average 0.099 mm with a standard deviation of 0.006 mm. The average mass per square meter was also determined as 60.997 g. Coated samples were then cut to appropriate areas and weighed out. The increased mass per area was then quantified and an estimated film thickness was determined. For the coated samples, this was a better estimate than simply measuring with a micrometer as liquid sample penetrates the paper, undershooting the actual coating thickness. Weigh boat samples were also measured for thickness, but mostly to determine usefulness as oxygen permeation samples. Those samples had an average thickness of 1.346 mm with a standard deviation of 0.052 mm.

2.2.2. Polarized Optical Microscopy

A Leica DM 2500P polarized optical microscope was used to observe both the liquid samples during preparation and solid samples. Liquid samples were monitored to ensure aggregation was minimized throughout the lifetime of the samples. Solid samples were observed to monitor any potential aggregation and monitor the condition of the semicrystalline nature of the PVA. The paper substrate used for some samples was also observed, specifically areas of thinness and holes.

2.2.3. Fourier-Transform Infrared Spectroscopy

Fourier-Transform Infrared Spectroscopy (FTIR) testing was performed using a Thermo Scientific Nicolet iS10 using the 16-scan mode. Data was analyzed using Essential FTIR, locating peaks and calculating the height and integral of the OH peak from 3030-3700 cm^{-1}. Samples were scanned in liquid, unconditioned, and conditioned form.

2.2.4. Rheometry

Rheometry profiles were determined using a Discovery hybrid HR-2 rotational rheometer with a two-degree cone top plate. One milliliter of liquid sample was placed on the bottom stage of the rheometer and tested with a shear rate sweep from 0.01-1000 1/s. This data could be important to collect if graphene oxide or cellulose nanofibers impact the coating's ability to be applied through high shear applications such as spray coating or spreads/sags more in low-shear applications.

2.2.5. Absorbance

Absorbance of the film samples was determined using an Agilent Cary 60 UV-vis spectrometer. Samples for this test were drawn down with a 6-mil drawdown bar on glass. The samples were removed from the glass in order to have the fewest transitions between materials. Adding glass to the spectra introduces extra error in the final data that needs to be accounted for. To obtain data, a background spectrum was first taken, then samples were simply placed between the aperture and the detector. The wavelength range was from 200 to 1100 nm. Data was then output from the instrument and converted to absorbance. From there, the absorbance data from the background was subtracted from each sample's data.

2.2.6. Color and Gloss Testing

Color and gloss testing was performed on 6-mil drawdowns on BYK black and white color paper. Color data was determined using a BYK Gardner Spectro-Guide 45/0 colorimeter set to D65/10° and gloss was determined using a BYK Gardner Micro-TRI-Gloss glossmeter set to 60 and 85°. Data was taken from the white portion of the paper in triplicate and any extremely low gloss values were thrown out.

2.3. Thermal Analysis

2.3.1. Thermal Gravimetric Analysis

Thermal gravimetric analysis was performed in triplicate on conditioned and unconditioned samples using a TA Q500 TGA instrument from 25-600°C at a ramp rate of 5°C/min. Average sample mass was 5 mg, prepared using offcuts from weigh boat samples and conditioned for three hours at 110°C. This test was run in atmospheric conditions, not under nitrogen.

2.3.2. Differential Scanning Calorimetry

Differential scanning calorimetry was performed using conditioned samples using a TA Q1000 DSC instrument in atmospheric conditions. Each test was performed in triplicate using a heat/cool/heat cycle from -50-275°C with a heating and cooling rate of 10°C/min. The results from TGA helped to determine an upper bound for this test so that too much degradation would not interfere with the second heating cycle's data. The average sample mass was 8 mg, also collected using offcuts from the weigh boat samples.

2.4. Mechanical Testing

Mechanical testing was conducted using a TA Q800 DMA on a triplicate of unconditioned and conditioned samples. The film-tensile mount was used, and samples

were cut from even areas of weigh boat samples in a “dog bone” shape in order to ensure a failure point between the grips instead of at the grips. The dog bone dimensions were scaled down from ASTM D638 Type IV. Figure 12 shows the template cut and the dimensions used to make it. A line was marked on samples to indicate where the clamps would line up to ensure even holding points between tests. To run the test, a strain ramp of 5% per minute was used with a final strain at 500%. For paper samples, simple 3x30 mm rectangles were cut from areas of high uniformity in from the bulk paper.

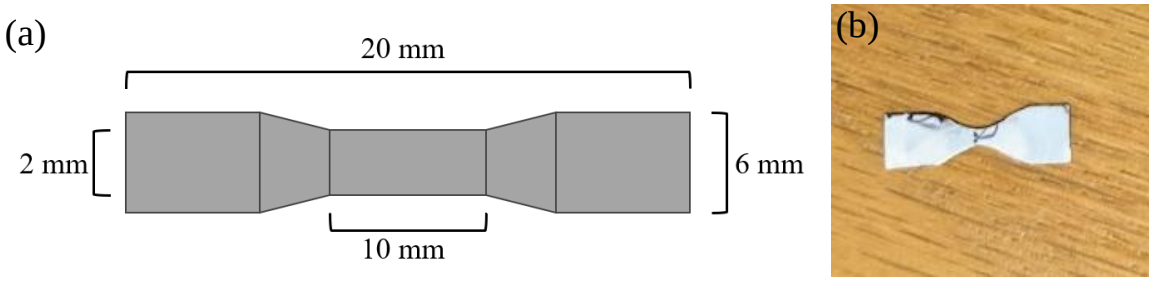

Figure 12. Dimensions (a) of the dog bone template (b) used for tensile testing.

2.5. Solvent Permeation

2.5.1. Water Vapor Transmission

Water vapor transmission testing was performed using regular-mouthed 400 mL Ball jars. Standardized vapometers were considered, but the jars were tested for water and air-tightness and were deemed a suitable alternative. To set up the test, paper samples were cut into circles using the jar lids as a template. The cut samples were then weighed and labelled. The flat, metal component of the lid was then replaced by the sample, coated side down. Next, each jar was marked with the sample name and filled with DI water to approximately 200 mL and the lids were secured onto each jar. From there, each jar was weighed, then placed into a PH09-DA Darwin environmental chamber at 50%

humidity and at 23°C. The mass loss over time was determined by simply weighing out each jar on day two and four, then once a week for four weeks.

Water vapor transmission rate was determined using water loss divided by area and time and reported in units of g/(hour*m^2) (Equation 1).

$$WVTR = \frac{water\ loss\ mass}{transfer\ area\ \times\ time\ period}$$

Equation 1. Water vapor transmission rate using average water loss, area, and time.

Next, two vapor pressures were calculated using the 50% humidity and 25°C of the chamber and 100% humidity to represent the inside of the jars. To calculate permeability of each sample, first the Tetens equation was used to determine the saturation water vapor pressure (Equation 2).

$$Ps = 0.61078 \exp\left(\frac{17.27(temperature)}{(temperature) + 237.3}\right)$$

Equation 2. Saturation water vapor pressure (Ps) using temperature in Celsius.

From there, the saturation water vapor pressure was used to calculate the water vapor pressures at 100% and 50% humidity. For 100% humidity, the water vapor pressure was simply equal to the saturation pressure, and the water vapor pressure for 50% was half. From there, permeability could be calculated using the rate acquired previously, an estimated film thickness, and the difference between the two calculated water vapor pressures (Equation 3).

$$Permeability = \frac{Mass \times Thickness}{Time \times Area \times \Delta Pressure} = \frac{WVTR \times Thickness}{\Delta Pressure}$$

Equation 3. Permeability caluclation incorportaing the water vapor tranmssion rate, sample thickness, and change in pressure.

2.5.2. Cobb Testing

Cobb testing was performed three times, using water for unconditioned and conditioned samples, and using oil for conditioned samples. A modified TAPPI T411 Cobb testing procedure was used, making substitutions where practical. To start, 200 mL of DI water or 1-2-3 vegetable oil was poured into each of the jars used for water vapor transmission testing. The paper samples were weighed, then placed coated-side down on the lid and the lid was secured on the jar, carefully so as to not form creases in the samples. One at a time, jars were inverted for 120 seconds, then inverted again. The samples were quickly pulled out and dabbed with paper towels as consistently as possible to remove any surface moisture. The samples were then weighed again to determine the added mass from the absorbed water. To conserve graphene oxide (the yield from the Hummer's method in a lab setting is small), the samples used were the same ones used for water vapor transmission testing. Additionally, each sample was used for unconditioned, conditioned, and oil conditioned testing, in that order. To calculate the Cobb value, the mass of the water absorbed was divided by the exposed area of the samples.

2.5.3. Contact Angle Testing

Contact angle testing was performed using a RX-Trans imaging system and ImageJ. Pictures were generated by carefully taping a coated paper sample to the stage so that the camera view displayed a singular flat surface. The instrument was set to take pictures every second for five minutes to ensure enough data could be collected. A needle was then run across the focal point to ensure the camera was focused and the area of interest was sufficiently flat. Next, a singular drop of DI water was placed on the surface

of the sample and left to sit for a period of 240 seconds. Finally, the angle tool in ImageJ was used to analyze the exported images and determine contact angle. Figure 13 displays the zoomed-out image of the entire droplet after zooming in to determine the precise angle at the edge of the droplet.

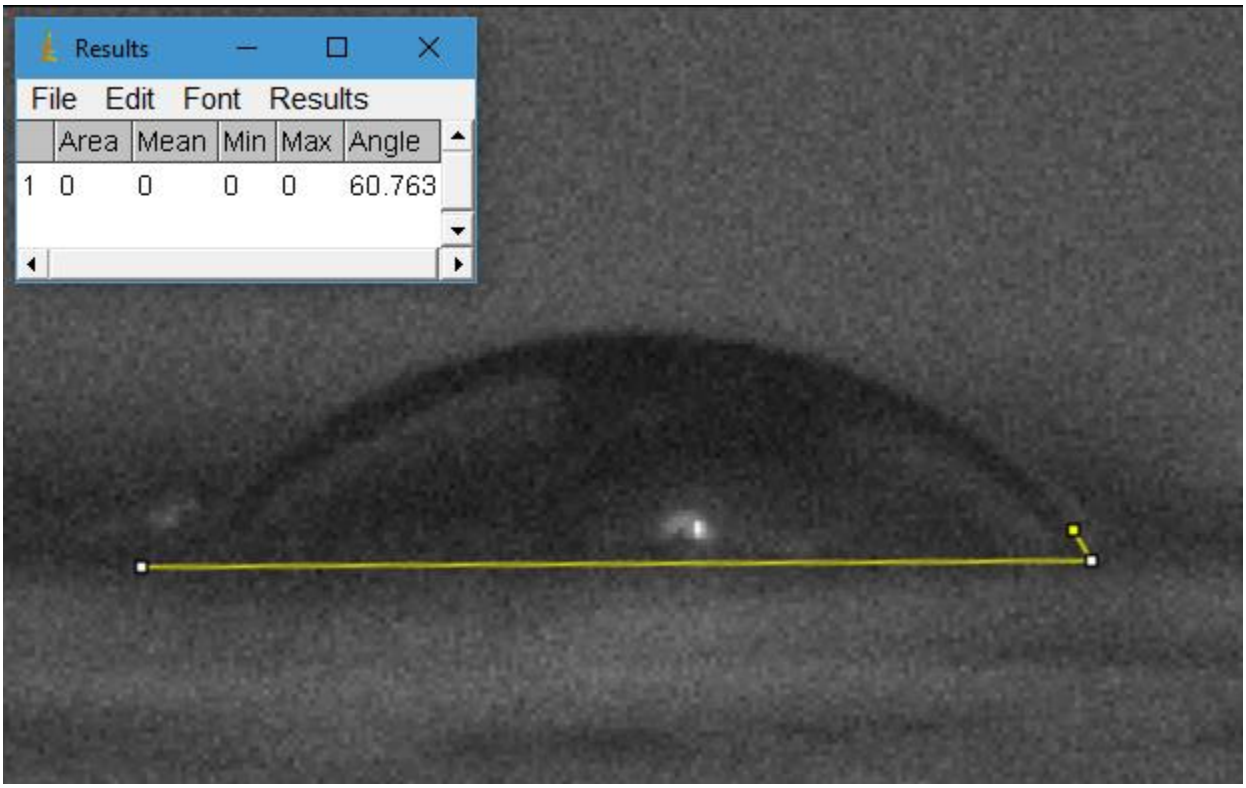

Figure 13. Determination of contact angle for water droplets using ImageJ.

2.5.4. Water and Oil Absorption

Absorption of water and oil was determined by cutting samples approximately two and a half centimeters by three millimeters out of the cast samples, weighing, and placing them in one-dram vials with DI water and oil. Samples were taken out, lightly patted dry, and weighed at intervals of 1, 5, and 30 minutes, then 1, 3, 5, and 24 hours. A final mass was determined at 7 days. Conditioned samples were the only ones tested as their water content would be comparable to one another.

2.6. Oxygen Permeability

Oxygen permeability was determined for each sample using an OX-Tran model 2/22 oxygen permeability tester. Samples were prepared by first locating the most uniform sections of the casted weigh boat samples and determining their thicknesses in a one-centimeter grid on the samples. A 20 mm circle was traced on the surface of the sample in the best section and folded or otherwise non-flat sections were trimmed. To adapt the samples to the instrument, aluminum tape was used to seal in the samples. First, the shape of the chamber midsection was cut out of a folded piece and a 20 mm punch was used to make a hole in the middle. Next, the wax paper protecting the adhesive was peeled off and the circle marked on the samples was carefully lined up with the hole. The samples were then pressed into the aluminum tape and the tape was folded over to encase the sample. Finally, a rubber mallet was used to secure the sample and to flatten out the perimeter of the aluminum tape (Figure 14). To prepare the chamber for the test, specialized oxygen barrier vacuum grease was spread across one side of the chamber and the samples were placed in the chamber. Finally, the chambers were loaded into the instrument and data was collected.

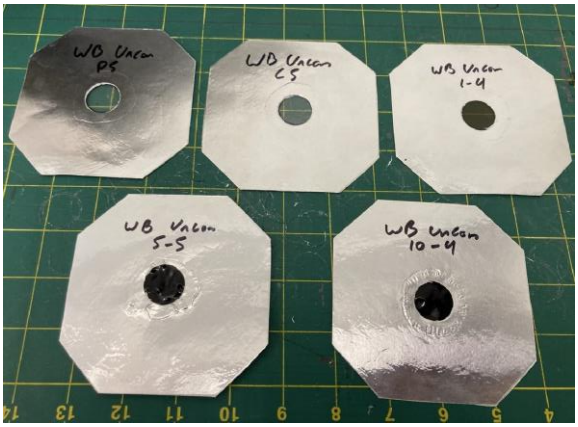

Figure 14. One of each weight boat sample composition prepared for oxygen permeation testing.

2.7. Microwave Testing

Microwave testing was performed by first cutting a strip of paper drawdowns into 2 x 5.5 cm rectangles. Next, samples were weighed, then rolled and placed in a 15-dram vial approximately two centimeters in diameter. One at a time, 6 milliliters of DI water was then added to the vials to cover the paper samples, then the vial was placed into the middle of the spinning platter of a MT5111XDQ-0 1000-watt Whirlpool microwave. The microwave was then turned on for 30 seconds at a time up to 120 seconds and an Etekcity Lasergrip 1080 infrared thermometer was used to quickly determine temperature at each interval. Another test was performed with the microwave, this time putting all samples in a ring around the middle of the platter, again with 6 mL of DI water. The microwave was set to half power for ten minutes, and jars were reweighed to determine the mass loss from boiling and evaporation.

2.8. Bacterial Inhibition Testing

Bacterial inhibition testing was performed with cultures of *E. Coli* and *S. aureus* to represent gram-negative and positive bacteria. First, a solution of the bacteria was obtained by pulling bacteria from an inoculator loop and vortex mixing with DI water. Next, prepared agar plates were evenly spread with bacteria solutions. Small 5 mm squares were carefully cut from the cast samples and disinfected by dipping in 70% ethanol for 30 seconds. Samples were then placed apart on petri dishes and the dishes were then allowed to culture for 24 hours at 37°C and observed for zones of inhibition surrounding the samples. If an inhibition zone was observed, a ruler was used to measure it at its narrowest and thickest dimensions.

3. Results and Discussion

3.1. Sample Preparation and Solution Properties

3.1.1. Polarized Optical Microscopy

Polarized microscopy was used to ensure aggregations of GO and CNF were not present in both the stock solutions and final mixed sample solutions. Aggregates can be noticed separately from dust and dirt through visualization of crystalline formations. Figure 15 shows typical optical micrographs of cellulose and graphene oxide aggregates that indicated further sonication was required. This works for CNF and GO because the cellulose used was initially in microcrystalline form and GO aggregates appear in crystalline form.

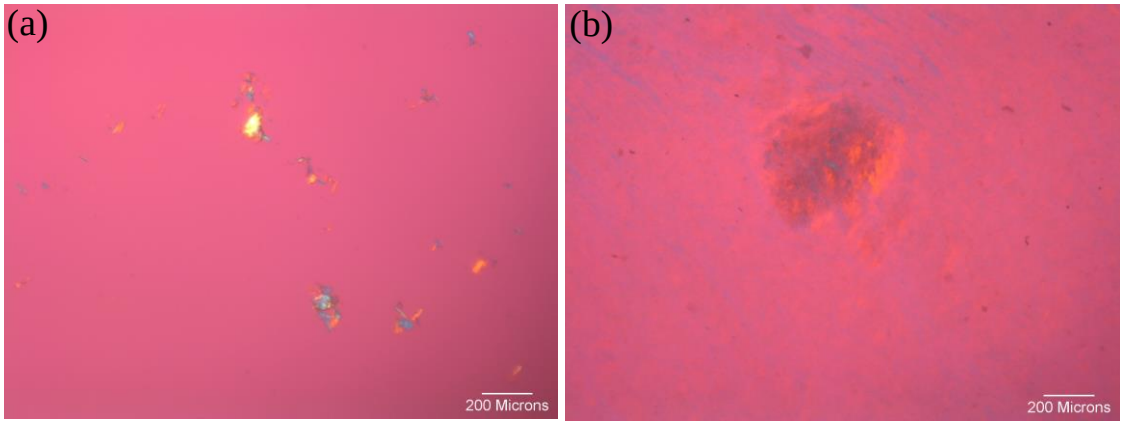

Figure 15. Cellulose (a) and GO (b) aggregations at 20x magnification.

For the cellulose stock solution, careful observation of aggregates was performed as applying aggregated CNF to finished solutions would only increase the amount of time for which the samples needed sonication. Figure 16 illustrates optical micrographs of CNF solutions at the beginning and end of sonication. It can be seen that there are many aggregates before sonication which become invisible after sonication. This observation indicates that sonication is effective to exfoliate and disperse CNFs in water.

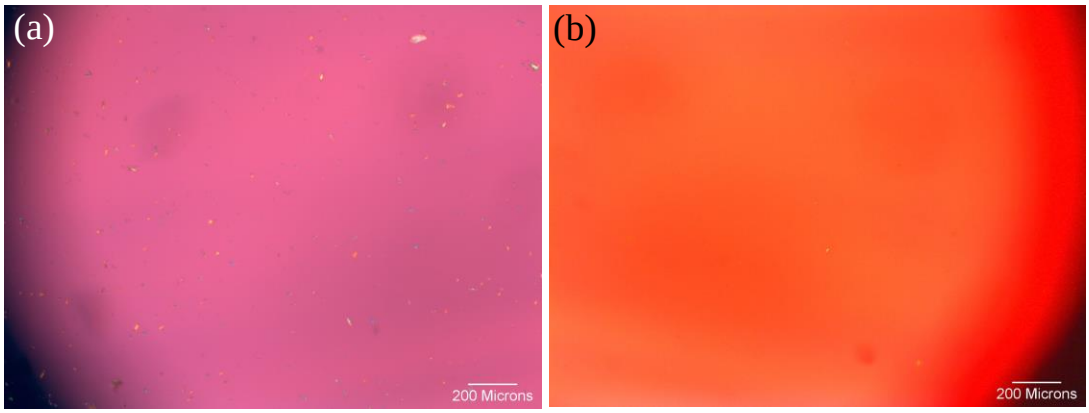

Figure 16. Low-concentration cellulose stock solution at 5x magnification towards the beginning (a) and end (b) of sonication.

Concerning the GO stock solutions, aggregates can be eliminated much faster than the CNF solutions. Within 30 minutes of tip sonication, high concentration GO transforms from a multi-phase liquid to a singular phase as shown in Figure 17. These two phases are present due to the removal of the acidic supernatant and addition of fresh DI water. Removing aggregates takes longer but is still fairly fast. A typical liquid crystal texture was observed in the concentrated singular phase (Figure 17b).

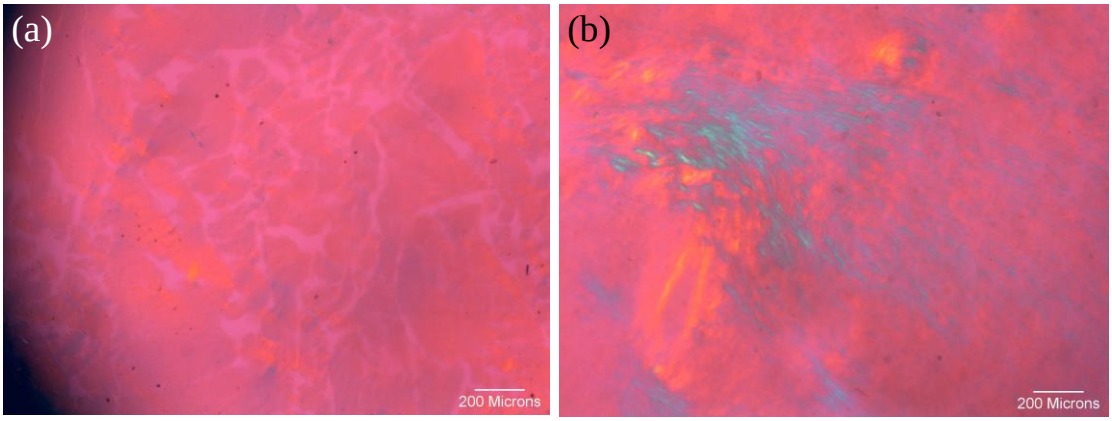

Figure 17. High-concentration graphene oxide stock solution at 5x magnification towards the beginning (a) and end (b) of sonication.

Dry samples were also observed, specifically for aggregates and to monitor the semicrystalline nature of PVA as nanomaterials were added. All samples displayed semicrystalline features through small crystalline spherulites and were free of visible

aggregates (Figure 18). As more nanomaterials were added to the PVA, the crystalline spherulites get visibly smaller and more dispersed. This is due to the increased loading of GO, which helps to provide more nucleation sites, which in turn decreases the size [53].

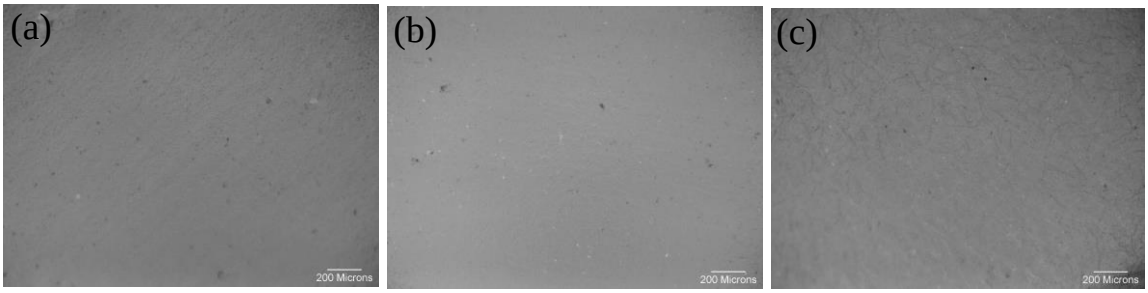

Figure 18. Unconditioned PVA (a), CNF (b), and 1% GO (c) samples at 5x magnification.

3.1.2. Fourier-Transform Infrared Spectroscopy

FTIR for each sample showed mostly expected behavior. To start, liquid samples were analyzed using Essential FTIR v3.50.218. Unfortunately, the large presence of water in the samples made observing specific peaks difficult. The high water content in the samples is indicated by the large broad peak at 3380 cm^{-1}, which represents O-H stretching. This is observed in all solution samples, and it was decided that solid samples would be a better indication of chemical composition (Figure 19).

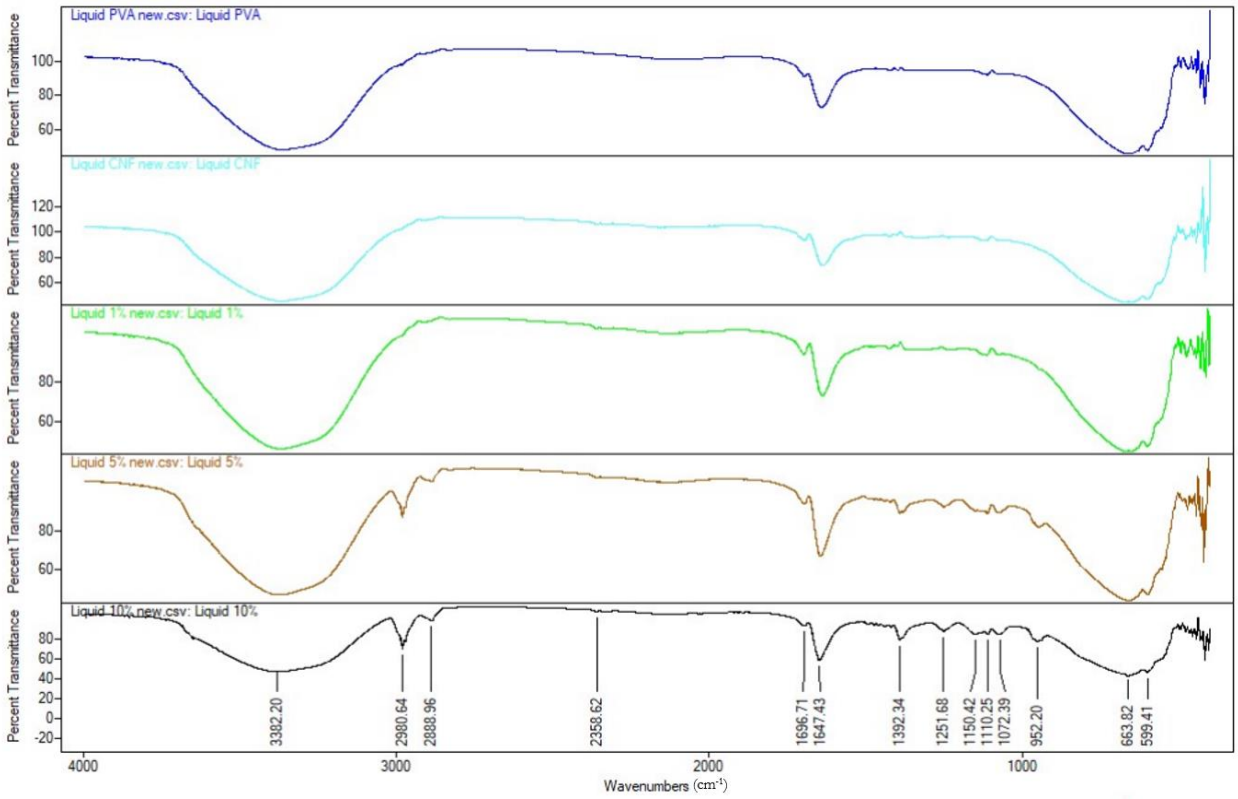

Figure 19. FTIR spectra for each composition's solution. From top to bottom: PVA, CNF, 1% GO, 5% GO, and 10% GO.

The loss of water in the samples as they are left to dry and conditioned was monitored using FTIR. The large peak almost completely disappeared for all conditioned samples, indicating the water content significantly decreased during the conditioning process (Figure 20). This was important as it ensured other tests would have an even starting point.

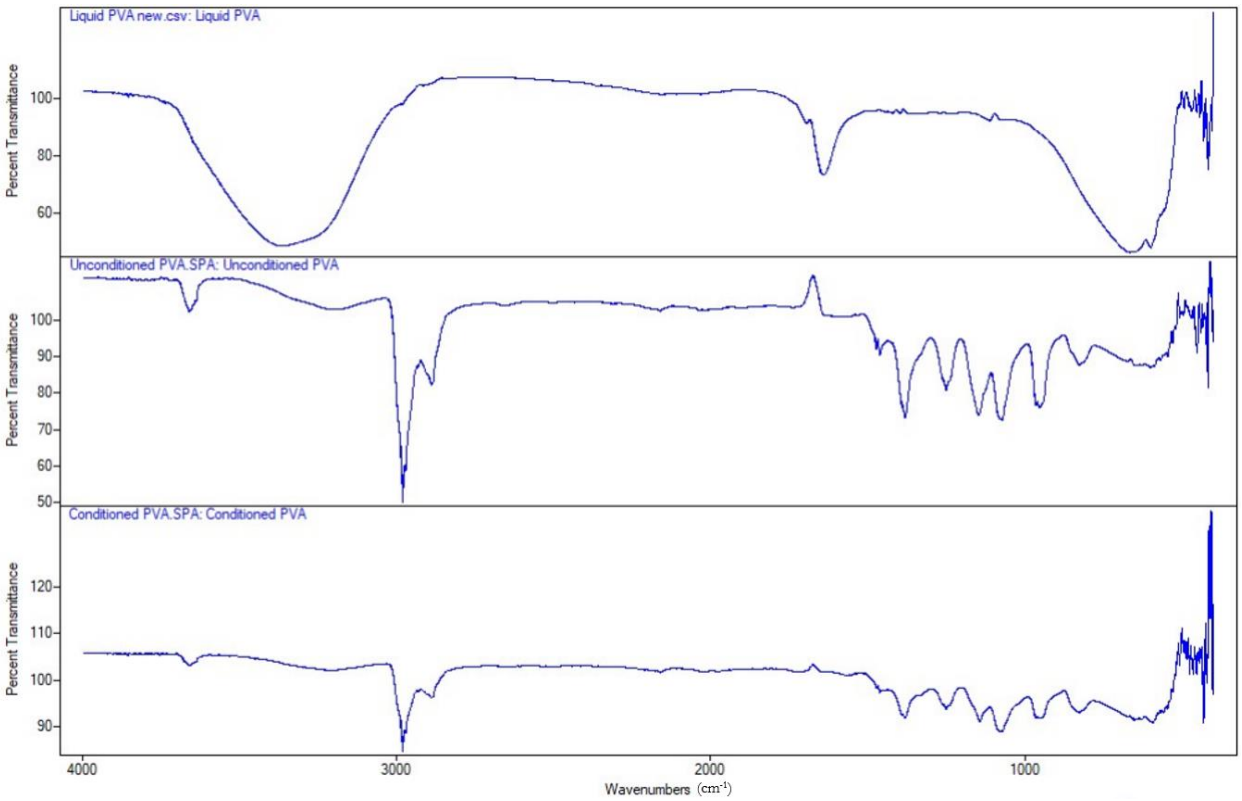

Figure 20. FTIR spectra of control PVA in liquid, unconditioned, and conditioned form, indicating a loss in water content.

3.1.3. Rheometry

The rheometry profiles of each sample were quite similar to one another. For everything except 10% GO, mostly Newtonian behavior was observed. For 10% GO, a slight shear thinning was observed (Figure 21). Overall viscosities decreased with the addition of low amounts of nanomaterials, but as the amount of GO increased, viscosity increased as well. Looking a little deeper, it can be observed that each sample is slightly shear thinning, as can be seen by the difference between the low and high shear rate viscosities (Figure 22). This was expected as polymers typically display a shear thinning behavior and the samples are only 4.1 wt% solid content, the rest being water [54]. Additionally, the difference between low and high shear seems to increase with the

composition of graphene oxide. This was expected as aqueous dispersions of GO are shear thinning [55].

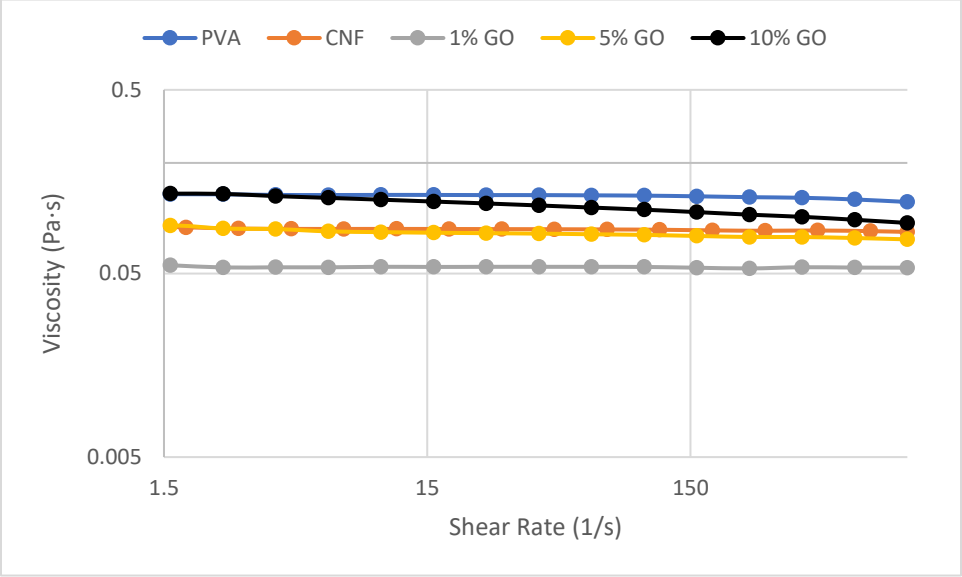

Figure 21. Rheometry profiles for each liquid sample solution.

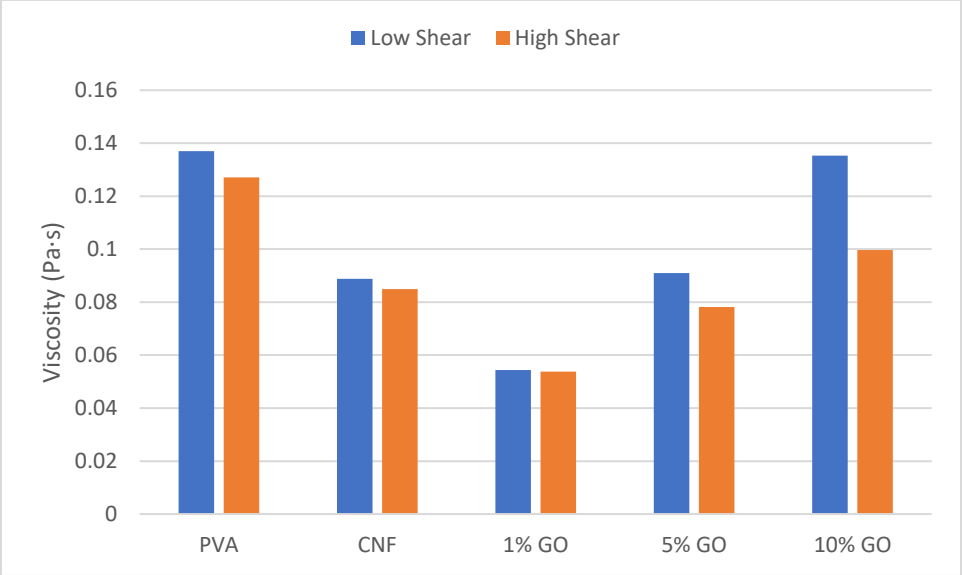

Figure 22. Changes in viscosity at low and high shear rate for each sample composition.

3.2. Structural Characterization

3.2.1. Fourier-Transform Infrared Spectroscopy

Following the solution samples, characteristic peaks for PVA were confirmed with the unconditioned and conditioned samples as lower water content obscured many of the smaller peaks. Important vibration bands to note are OH stretching from 3100 to 3400 cm^{-1}, CH_2 stretching at 2980 cm^{-1}, and C-H bending at 1381 and 1461 cm^{-1}. All of these peaks were observed in the unconditioned control PVA sample (Figure 23).

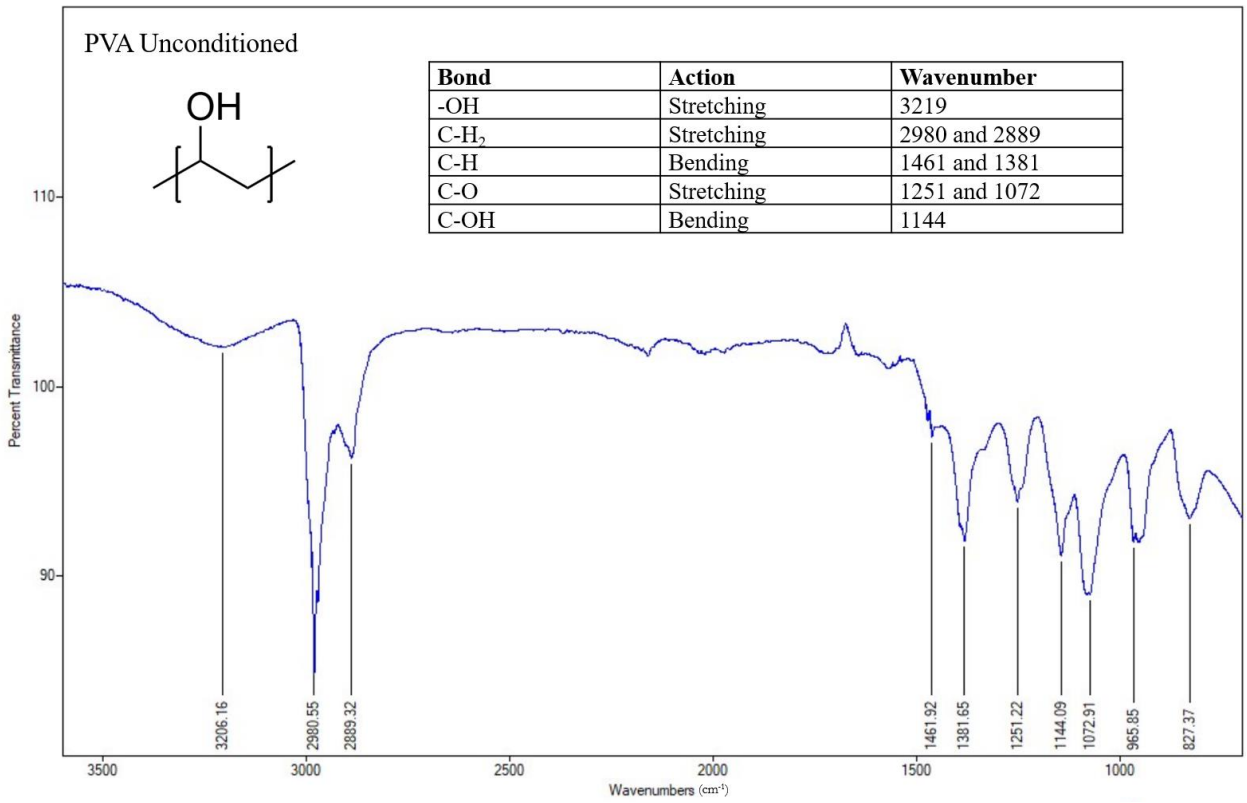

Figure 23. FTIR spectrum for unconditioned dry PVA.

Using FTIR, it can be difficult to isolate peaks for the CNF samples as the concentration of cellulose in the samples is not high in comparison to PVA. Additionally, many peaks overlap with those observed in PVA and GO. Especially between CNF and GO, most bonds are repeated, making analysis difficult. For CNF, the best indication of

its presence is an increase in the peak at 1334 cm^{-1} as it represents an alcohol group O-H bond, which does not change with water content. Additionally, the singular peak for C-O at 1072 cm^{-1} splits into two, one at 1074 cm^{-1}, representing a primary alcohol and the other at 1124 cm^{-1}, representing a secondary alcohol and an ether functional group. These two peaks are observable in the unconditioned CNF sample, indicating the proper addition of CNF to the sample (Figure 24).

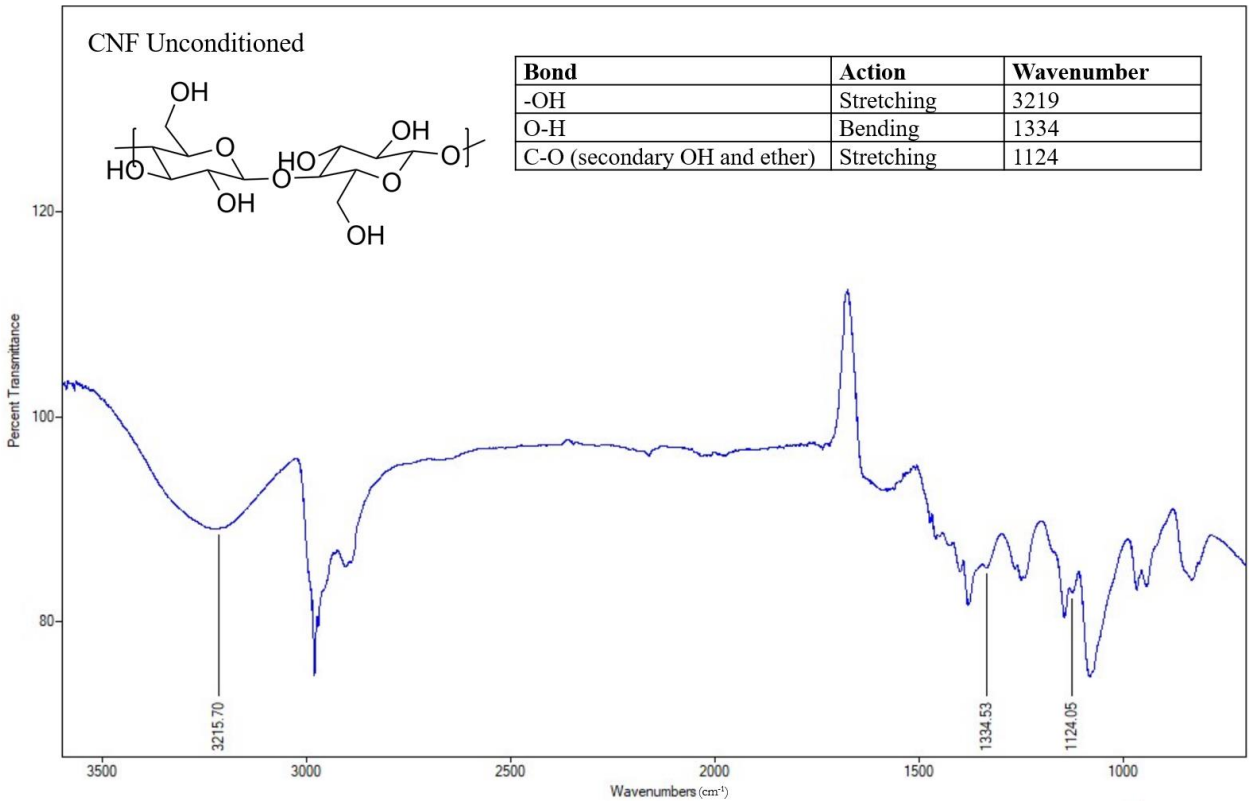

Figure 24. FTIR spectrum for unconditioned PVA with CNF.

To observe the addition of GO to the polymer samples, the best peaks to look at are C=O at 1763 cm^{-1} and C=C at 1630 and 995 cm^{-1}. Additionally, the C-O peak at 1085 cm^{-1}, which represents secondary alcohol and ether groups is increased due to the higher concentration of those functional groups. All of these peaks are observed in the spectrum of the 10% GO unconditioned sample, with the exception of C=O at 1630 cm^{-1} (Figure

25). Instead, there is a wide peak at 1599 cm^{-1} that extends over 1630 cm^{-1}, where if there were a peak, it may be obscured.

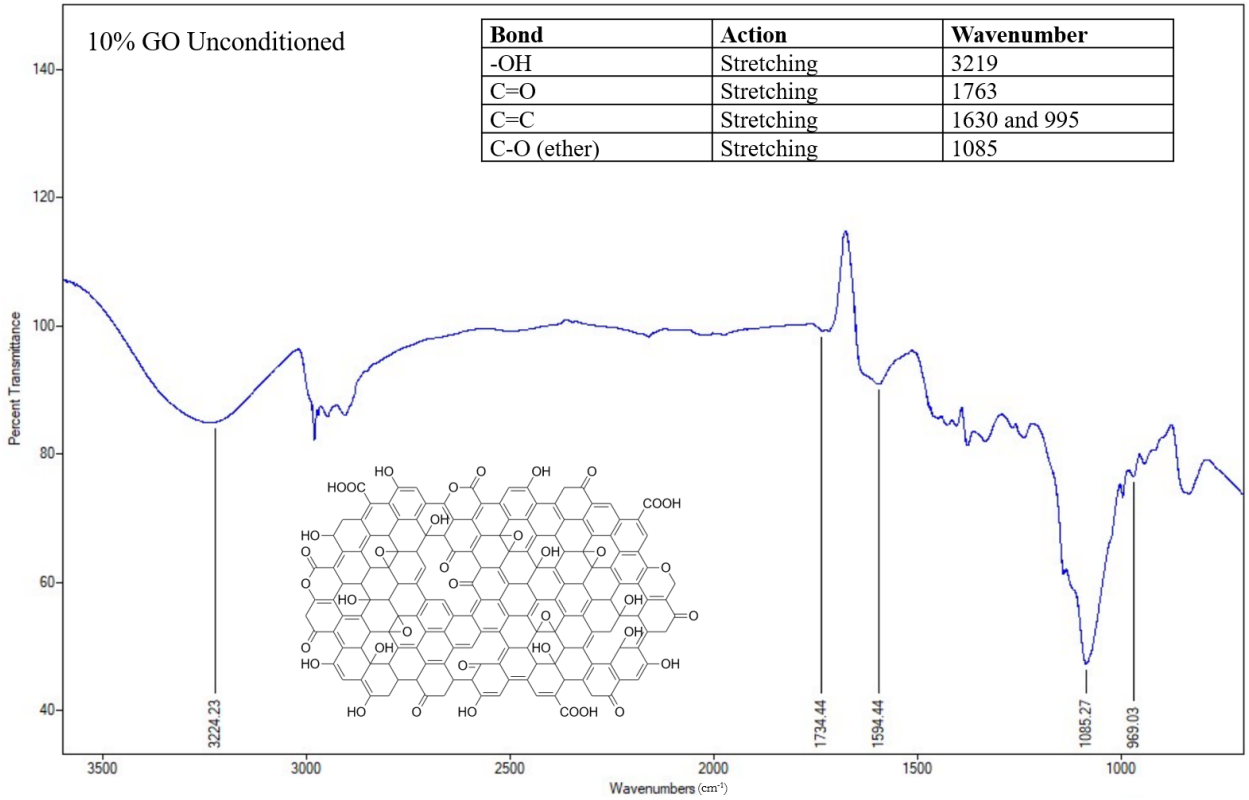

Figure 25. FTIR spectrum for unconditioned dry PVA with CNF and 10% GO.

To observe the chemical difference between unconditioned and conditioned GO samples, FTIR was used on both. The only changes observed between the conditioned and unconditioned 10% GO samples are a decrease in the OH peak at 3200 cm^{-1}, a decrease in C=O peak at 1763 cm^{-1}, and a decrease in the C-O peak at 1085 cm^{-1}. If graphene oxide was reduced significantly, the peaks indicating alcohol and ether groups would decrease, and double-bonded carbon-carbon bond peaks would remain. This is because through the reduction of graphene oxide, the nanoparticles lose some of their hydroxyl and carbonyl groups, forming a mostly uninterrupted graphite structure. This change is observed in the conditioned sample and indicates the conditioning step may

cause partial reduction of graphene oxide (Figure 26). It has been reported that graphene oxide can be reduced when heated above 100°C [56].

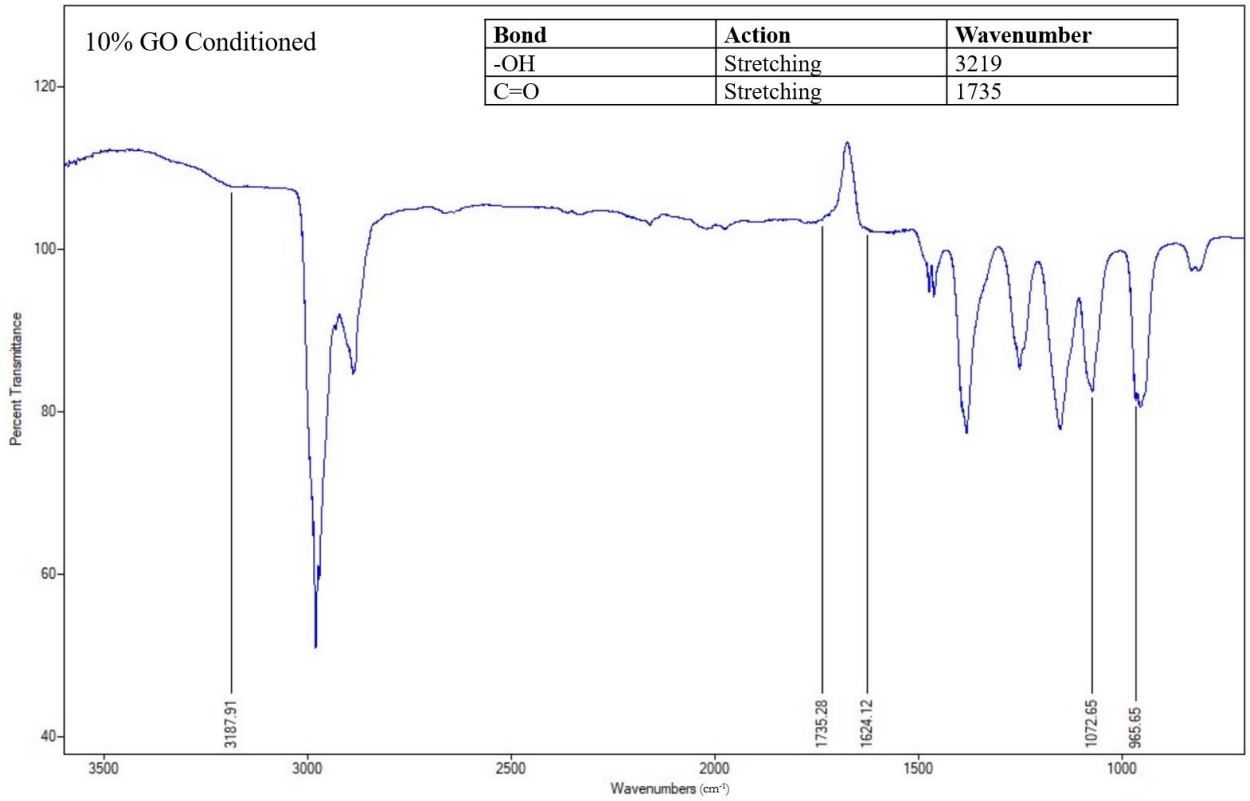

Figure 26. FTIR spectrum for conditioned dry PVA with CNF and 10% GO.

3.2.2. Absorbance

Figure 27 shows the high absorbance of visible light for both unconditioned and conditioned high loading GO samples. Unconditioned samples displayed large difference in absorbance for all samples between around 250-900 nm, with the largest peaks being at approximately 350 nm. The control PVA and cellulose nanofiber samples performed almost identically, absorbing almost nothing over the entire range of visible light. For graphene oxide samples, their absorbance increased as their composition increased. These trends follow with how the samples appear visually, with PVA and CNF samples being

completely transparent and the 1, 5, and 10% GO samples progressively getting harder to see through.

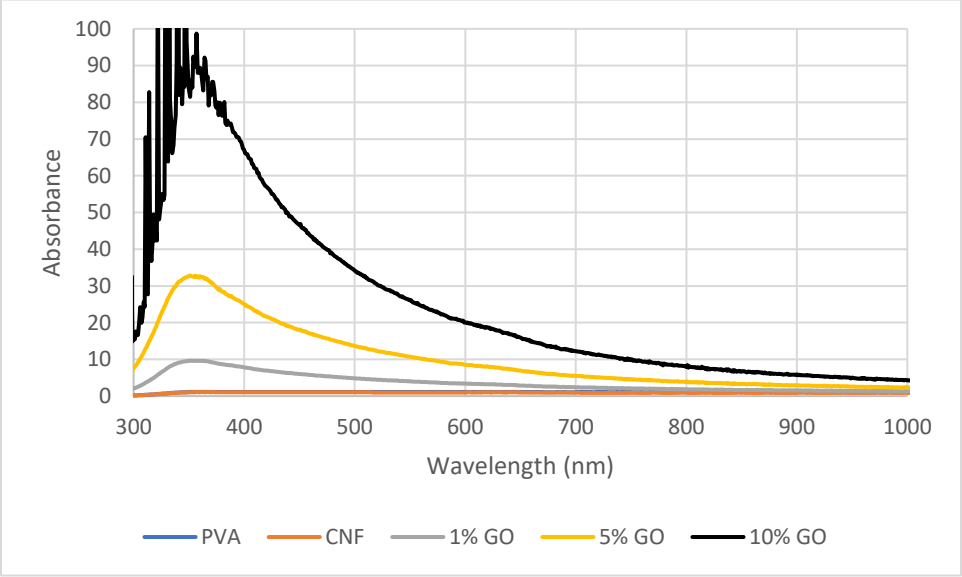

Figure 27. UV-vis spectra for each unconditioned sample composition.

For the conditioned samples, there was again a large difference in absorption of samples across the entire range of visible light as shown in Figure 28. Similar to the unconditioned samples, the control PVA and CNF samples displayed little to no absorbance throughout the entire wavelength range. The graphene oxide samples did increase absorbance over the entire range of light, with higher GO loading further increasing the absorbance. This is not particularly observable in the samples themselves as both conditioned 5 and 10% GO samples appear the same level of black visually. The broadening of the absorption peak to cover the entire spectrum is indicative that graphene oxide has partially been converted into reduced graphene oxide during the conditioning treatment.

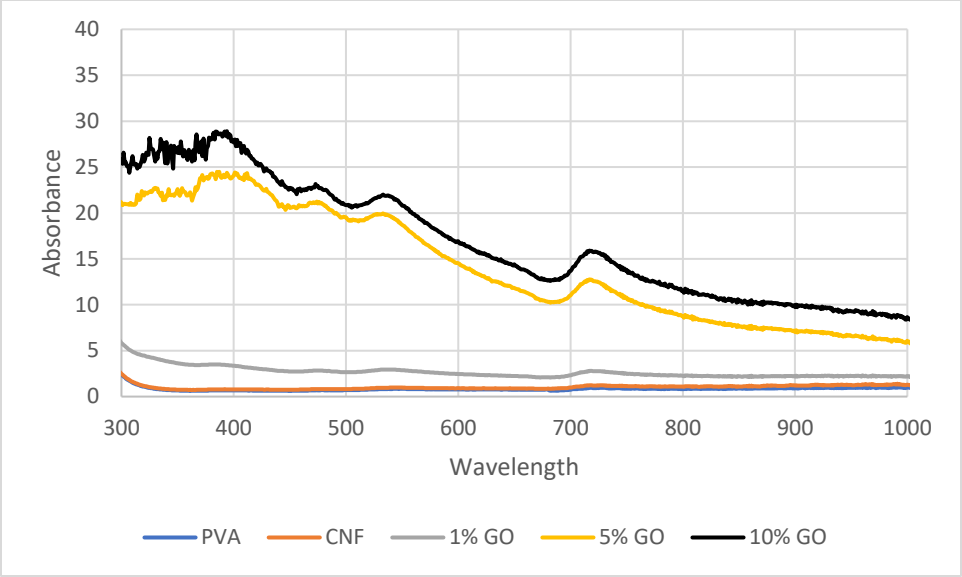

Figure 28. UV-vis spectra for each conditioned sample composition.

As there is no real difference between the absorbance from the cellulose and control PVA, it can be concluded that PVA and CNF will not absorb light within this range of wavelengths. As a calibration curve was not performed with the stock solutions, the magnitude of absorbance cannot be accurately used to confirm percent loadings of additives, but the unconditioned samples certainly seem to display the 1, 5, and 10% GO loadings with the absorbances of 10, 32, and 88 at their peak at 350 nm.

3.2.3. Color and Gloss Testing

The color data determined using the colorimeter followed expected trends from visual inspection and absorbance. As samples increased in loading of graphene oxide, they became darker. This is observable in Figure 29, where a CIELAB L value of 100 corresponds to white and 0 is black. This follows the observed darkening of samples after going through the conditioning process and the trends observed in FTIR and UV-vis, where graphene oxide seems to be partially reduced.

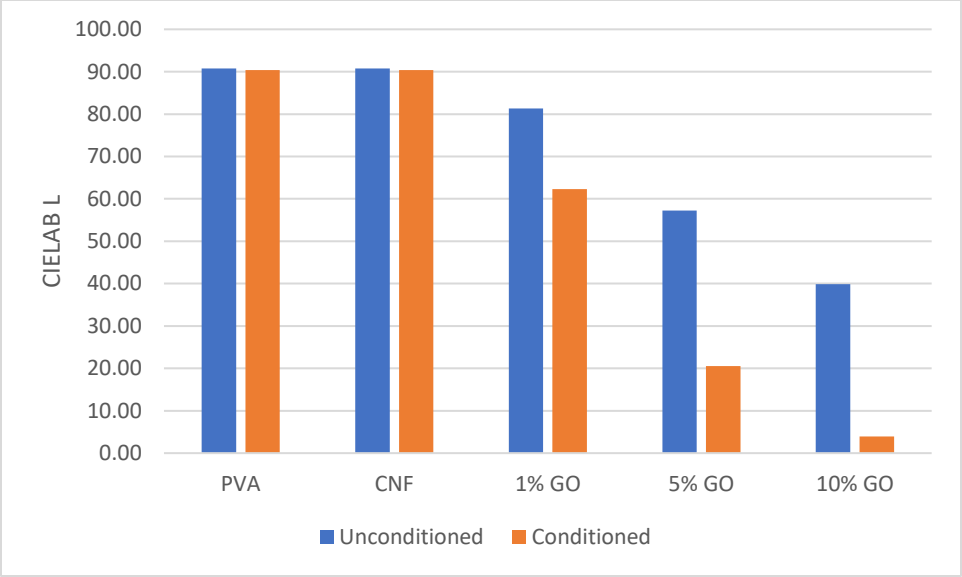

Figure 29. CIELAB L colorimeter data for unconditioned and conditioned samples.

For gloss, there were some interesting trends, but also potentially a high degree of error. As more filler was added to the samples, in general gloss decreased. For the 85° gloss, the unconditioned samples follow the best trend, decreasing in gloss only when GO is added and drastically decreasing as the loading reaches 5 and 10 wt%. This could be explained by an increase in surface roughness caused by GO appearing at the surface. The conditioned data for 85° gloss displays PVA and CNF samples decreasing in gloss, while the GO samples all increased (Figure 30a). This could be attributed to the partial reduction of graphene oxide, leading to a shinier surface after conditioning. For the 60° gloss, a trend is harder to pick out, but in general GO decreases gloss in its 5 and 10% loadings and there is little difference between gloss for PVA, CNF, and 1% GO. As for the difference between unconditioned and conditioned samples, there is a slight increase for the PVA and CNF samples, and a larger increase for 5 and 10% GO (Figure 30b). This data is likely not ideal as any section that was not perfectly flat would have produced significant error. This is because the glossmeter relies on the flatness of the sample to reflect the light beam into its detector [57].

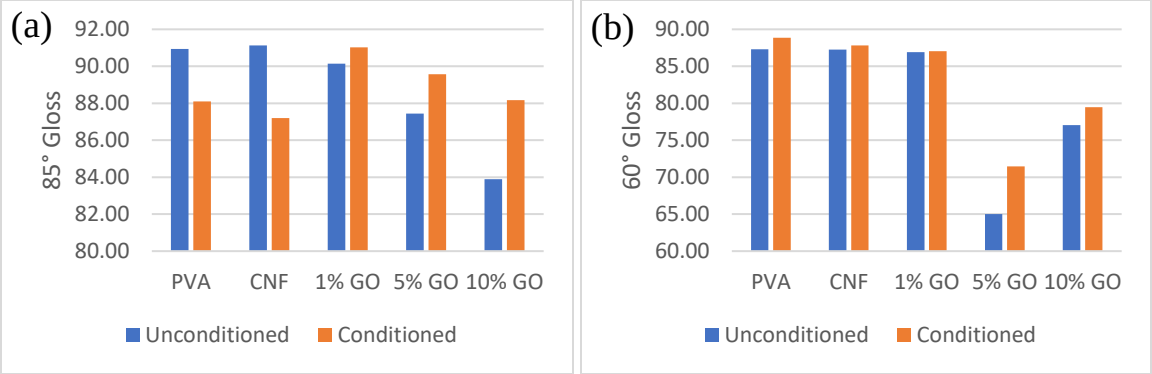

Figure 30. Gloss data at 85° (a) and 60° (b) for unconditioned and conditioned samples.

3.2.4. Contact Angle Testing

Contact angle testing helped a lot to understand the water Cobb test results for the uncoated paper samples. When the droplets were first added, it had the highest contact angle, indicating its initial hydrophobic nature, likely due to its roughness compared to the coated samples (Figure 31). As the test continues, the paper sample quickly starts taking in the water droplet, and by 120 seconds all of the water droplets had been completely absorbed into the paper. For the coated samples, CNF performed slightly better than the control PVA for the first two minutes, but over time performed about equally. Interestingly, 1% GO performed better than both 5 and 10% GO initially, until a crossover at approximately 45 seconds. After that, it consistently displayed worse performance than the higher loading samples. Finally, 5 and 10% GO had practically identical performances throughout the entire test, indicating a maximum hydrophobic threshold for GO loading, at least for this test.

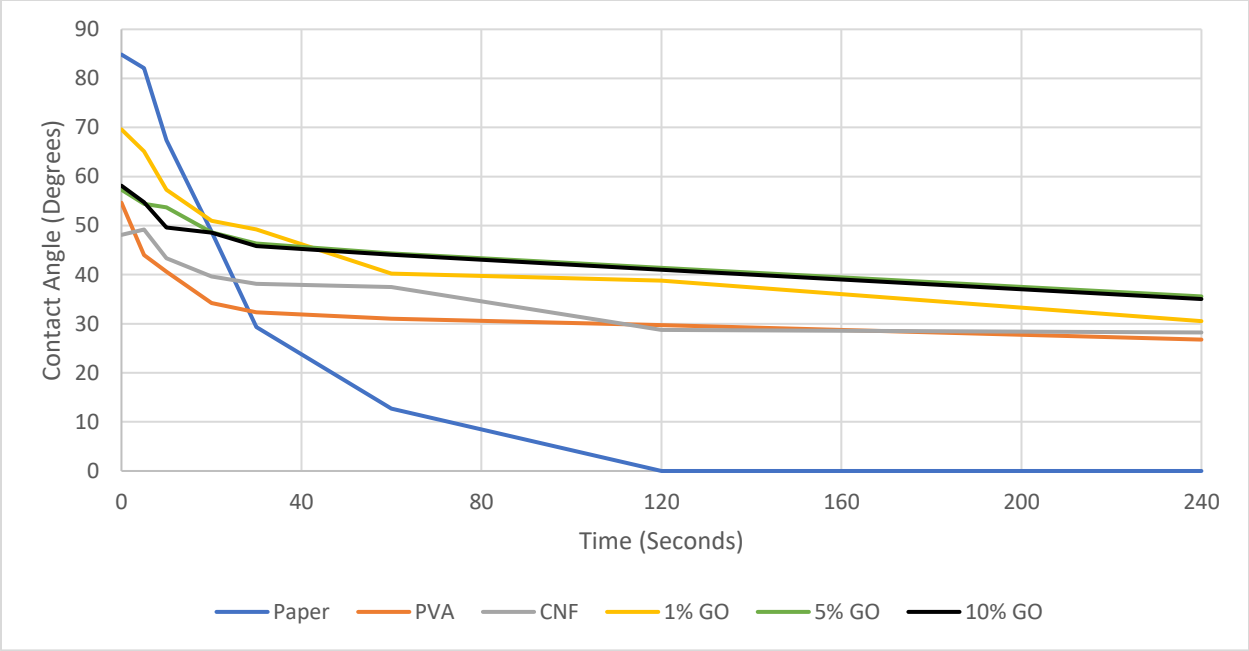

Figure 31. Contact angle of droplets on conditioned samples versus time.

3.3. Thermal Analysis

3.3.1. Thermal Gravimetric Analysis

Figure 32 indicates two distinct steps of degradation in the control PVA, one from around 225 - 325°C, and another around 425 - 500°C. In typical polymeric materials, only one degradation step is observed, but with PVA there are two distinct steps. The first step between 200 - 350°C represents the degradation of side chain groups, in this case hydroxyl groups. The second step between 400 - 500°C represents the polymer backbone degrading. This two-step behavior was observed in all samples tested.

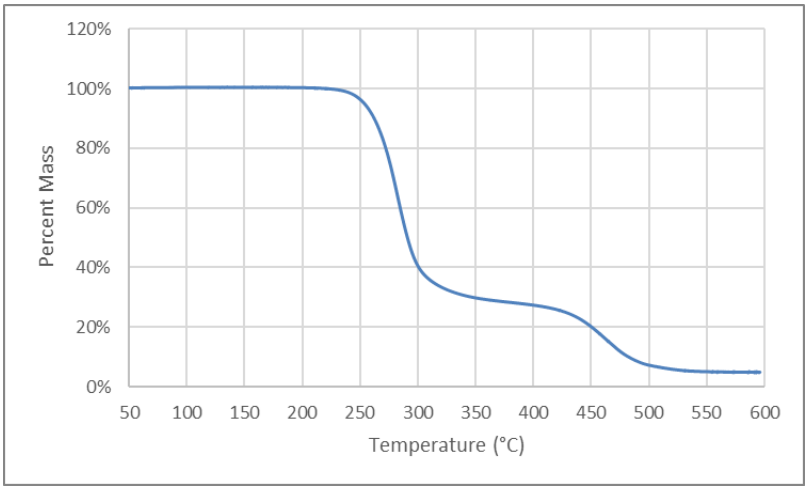

Figure 32. TGA mass loss versus temperature profile for control PVA.

The first observation with the TGA results was what percent mass remained at 200°C. This should be well before any degradation and would only indicate the water loss in the samples. Figure 33 shows a slight increase in water loss from PVA to CNF, but a much larger increase as GO was added. This follows the observations noted during the conditioning steps, that the GO samples hold on to water much more than PVA.

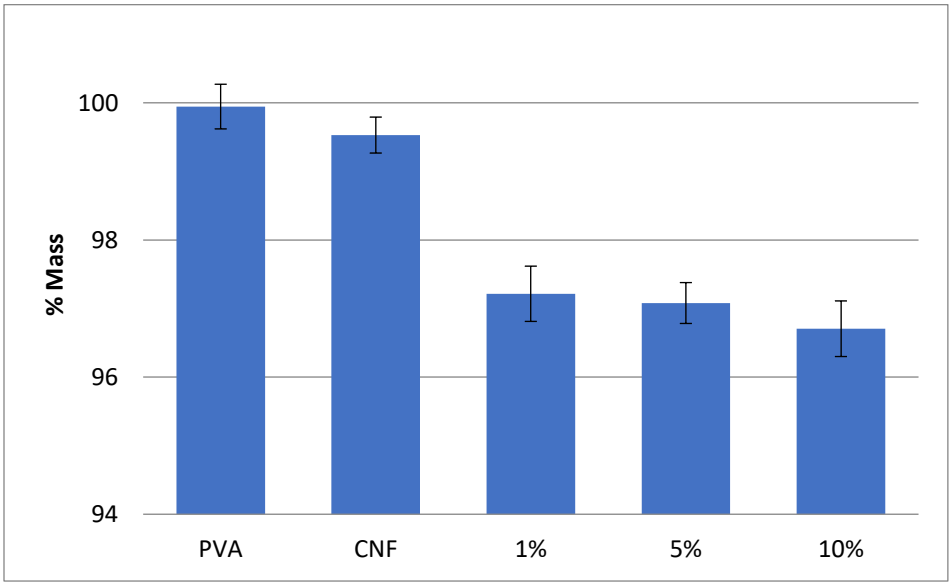

Figure 33. Percent mass at 200°C indicating water content in the samples after conditioning.

The next points of interest are the first step onset and midpoint. It was observed that with the addition of both CNF and GO, the midpoint increased, but the onset decreased significantly with the addition of GO but increased with the loading (Figure 34). This is consistent with literature as side groups bound by CNF and GO would take more thermal energy to degrade and eliminate [58].

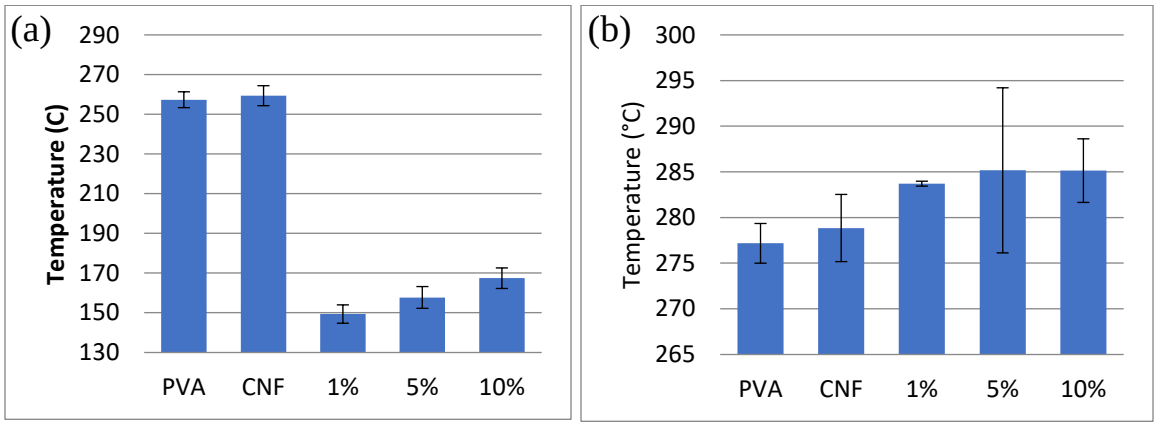

Figure 34. Onset temperature (a) and midpoint (b) of the first degradation step.

Interestingly, the first degradation step had different profiles between each sample, significantly changing for the GO samples as seen in Figure 35. This may be explained by an increase in thermal conductivity of partially reduced GO, which would facilitate the transfer of heat to the PVA matrix, accelerating the first-step degradation [59]. On the other hand, ordered PVA structures can be induced through the addition of GO, which would increase the thermal resistance of the material, thus the degradation temperatures.

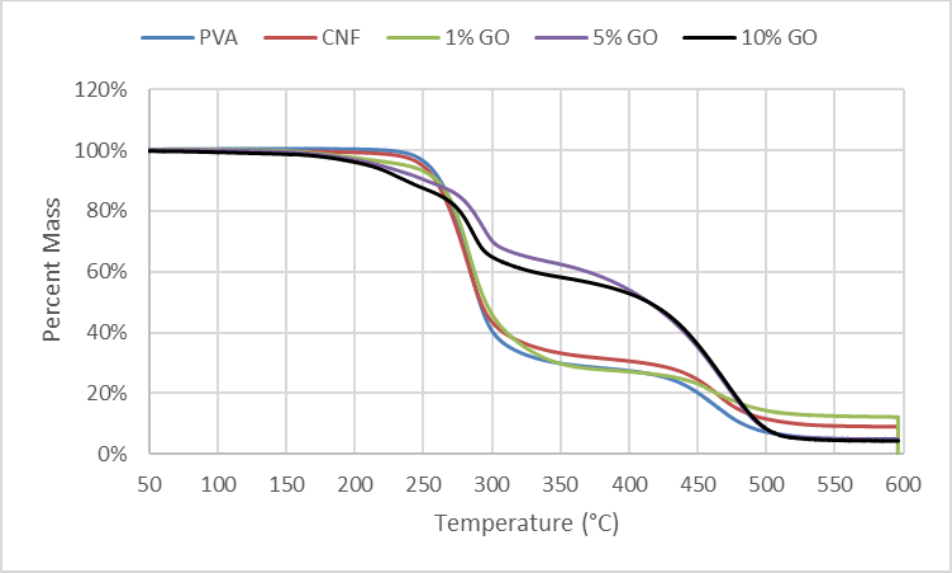

Figure 35. Overlayed TGA results displaying the difference in step profiles between each sample composition.

Next, the second onset and midpoint were observed for main-chain degradation (Figure 36). The overall trend appears to be that as more nanomaterials are added, the second degradation temperature increases. The exception to this is the results for 5 and 10% GO with the onset, but considering the different TGA profiles of those samples, the onset could be still including side chains.

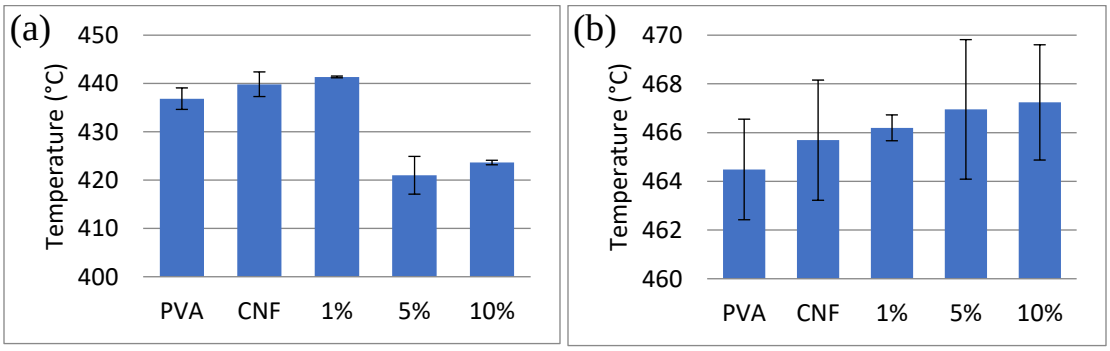

Figure 36. Onset temperature (a) and midpoint (b) of the second degradation step.

The percentage mass for each sample composition was recorded at 375 and 600°C to produce Figure 37. This displays the mass present after the first and second steps, where the 5 and 10% GO samples displayed that all of the extra mass present after the

first step was eliminated. Curiously there was a lower percent mass for the 5% GO sample at the end of the test, but that may be due to taring issues as values at the end would be the most susceptible to those sorts of issues.

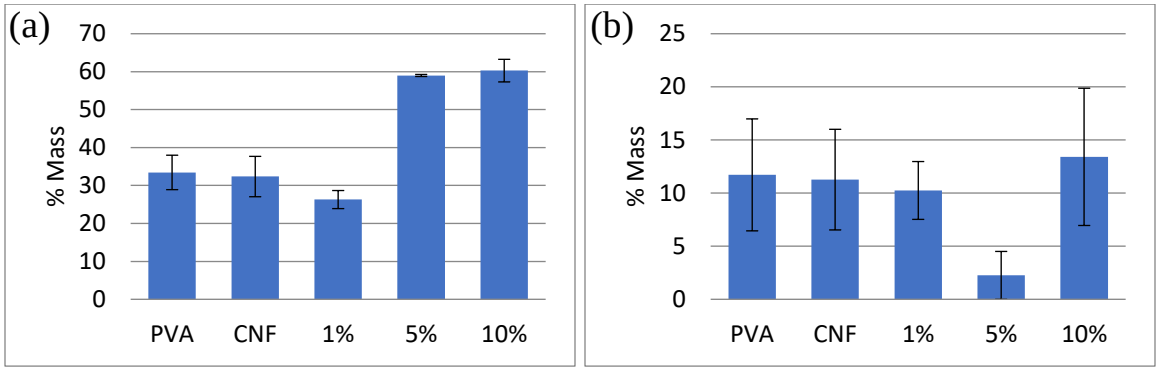

Figure 37. Percent mass of each sample composition at 375°C (a) and at 600°C (b).

3.3.2. Differential Scanning Calorimetry

Figure 38 shows the glass transition temperature was about equal for the control PVA and the CNF and 1% GO samples. This was within the literature range of 76 - 80°C for PVA, which is so large as it depends on the percentage of hydrolyzation [60]. As the loading of GO increased, so did the glass transition temperature, which was due to hydrogen bonding restricting the movement of polymer chains [61]. As glass transition is the point at which a polymeric material shifts from a glassy to rubbery state, the mechanism behind it requires polymer chains to slide past each other as mechanical force is applied [62]. With the hydrogen bonds present, the polymer chains require more energy to obtain the freedom necessary to slide past one another.

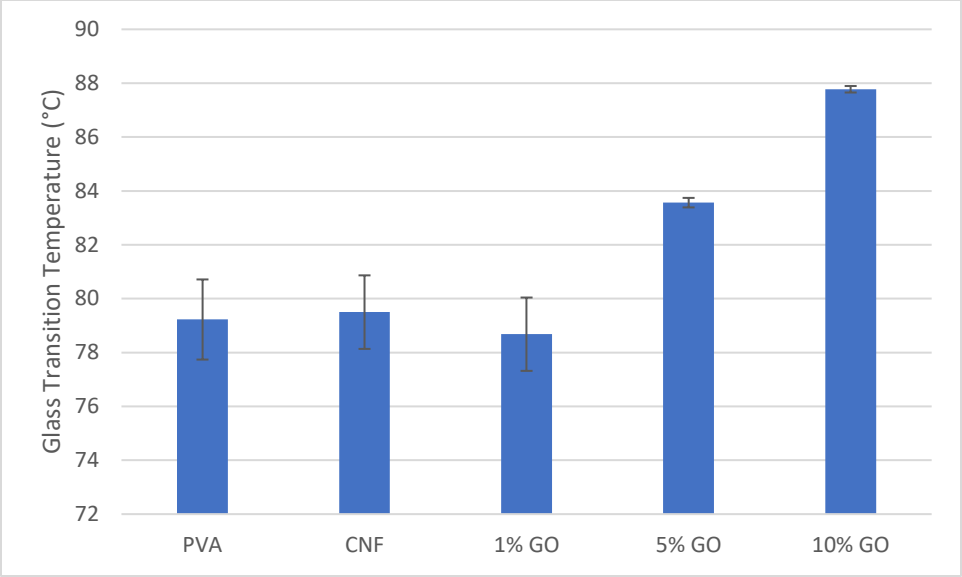

Figure 38. Glass transition temperatures for each sample composition.

Considering the melting points of each composition, there was a lot of observed variation within the same samples (Figure 39a). This could have been due to different individual moisture content between samples as higher water content, which can change the melting temperature up to 10°C [63]. As for the trend, the melting temperature slightly decreased with the addition of CNF, and continually decreased with the increased loading of GO. This follows literature as the melting temperature should decrease with the addition of both CNF and GO due to decreased crystal sizes as loading increases. For the enthalpy of fusion (ΔH), the values correspond to the degree of crystallinity of the polymer samples. The trend observed in Figure 39b suggests that with more added nanomaterials, the degree of crystallinity decreases, which is exactly what was expected. One note is that for the 10% GO sample, degradation occurred within the upper bound of the first cycle, so only the first heating cycle was compared.

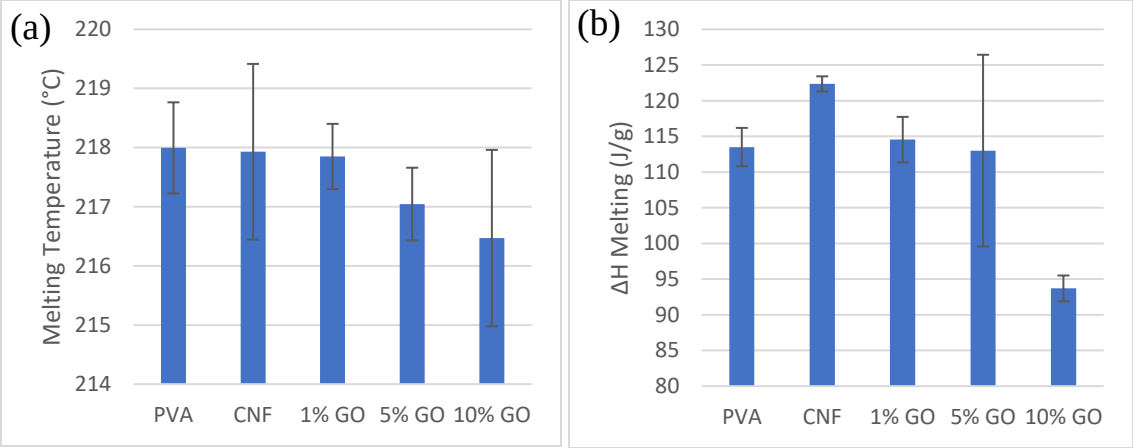

Figure 39. Melting temperatures (left) and heating enthalpy of fusion (right) for each sample composition.

Finally, crystallization occurred on the cooling cycles for each sample composition aside from 10% GO (Figure 40). The trend for crystallization temperature was an increase with the addition of nanomaterials, which may be explained by the nanomaterials acting as nucleation sites earlier on in the cooling cycle [53]. This would allow for crystalline regions to develop quickly, but higher loadings of the CNF and GO would make large crystalline regions difficult to finish developing. The cooling enthalpy of fusion results produced this trend mirroring expectations exactly. As more additives are added, it gets harder for large crystalline regions to fully develop, which decreases the crystallinity of the material as a whole.

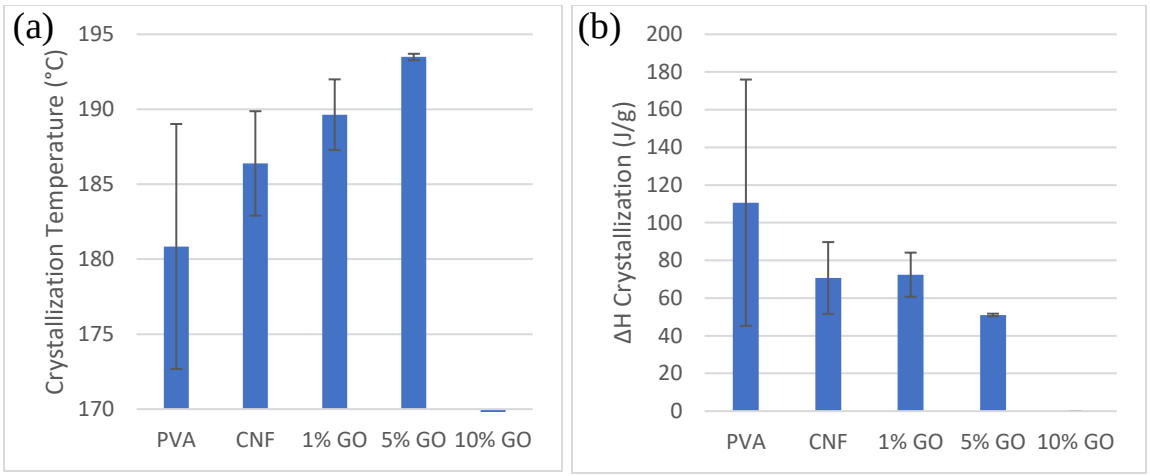

Figure 40. Crystallization temperatures (a) and cooling enthalpy of fusion (b) for each sample composition.

Because the test went to an upper limit of 275°C, each sample experienced slight side-chain degradation, a permanent change to the polymer structure. As properties such as melting point and degree of crystallinity change with the reduction of side chains, this degradation can also be observed using DSC [63]. Figure 41 displays an observable change in melting point and crystallinity as the samples are retested.

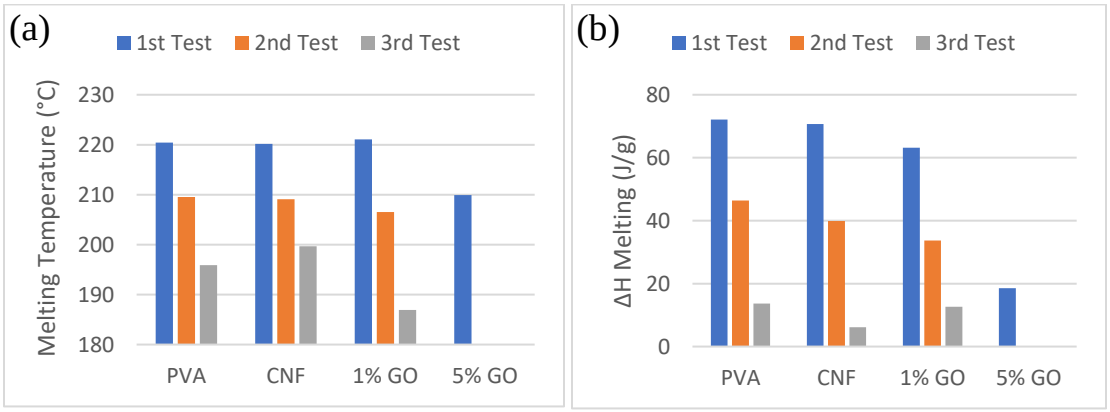

Figure 41. Change in melting temperature (a) and degree of crystallinity (b) as samples thermally degrade.

3.4. Mechanical Testing

For the mechanical properties of the cast samples, overall the addition of CNF seemed to do little to impact the stiffness of the PVA and the GO decreased the stiffness for both the unconditioned and conditioned samples (Figure 42).

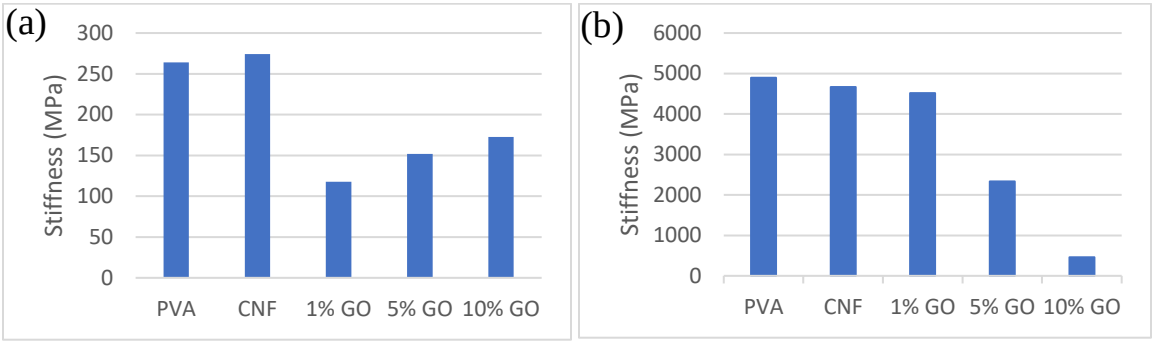

Figure 42. Elastic modulus/stiffness for unconditioned (a) and conditioned (b) cast samples.

For the ultimate tensile strength, the CNF and 1% GO samples saw a massive increase for the unconditioned samples, but with higher loading of GO, strength decreased. For the conditioned samples, ultimate tensile strength decreased with the increase in CNF and GO loading (Figure 43).

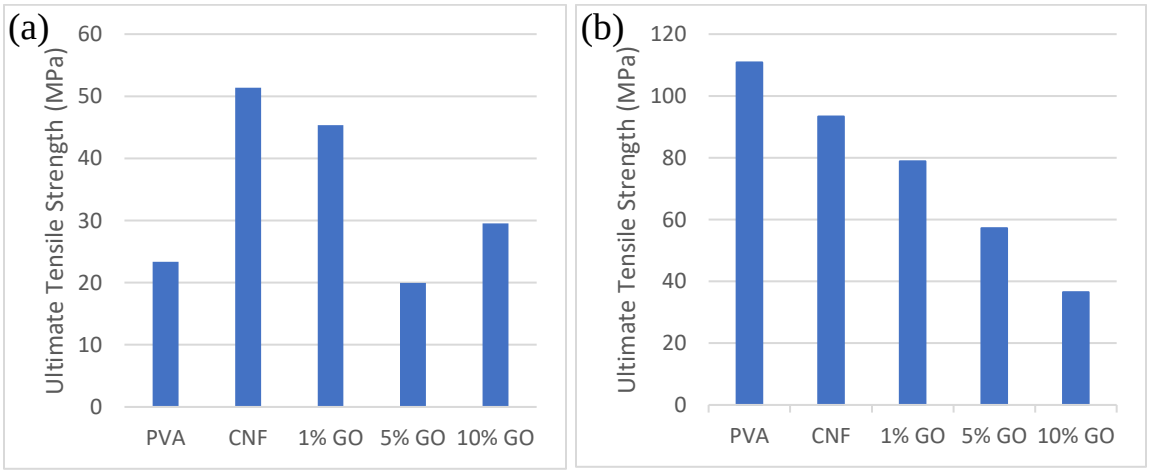

Figure 43. Ultimate tensile strengths for unconditioned (a) and conditioned (b) cast samples.

Considering the elongation of samples, the trend observed seems to be that as the CNF and GO are added, elongation increases (Figure 44). For the unconditioned samples, the largest percent elongation was 1% GO at approximately 490% strain, followed by CNF and 10% GO, which extended approximately 210%. PVA displayed the lowest elongation between all samples for both unconditioned and conditioned samples but decreased almost four times after conditioning. Finally, the conditioned samples increased their elongation with loading of CNF and GO.

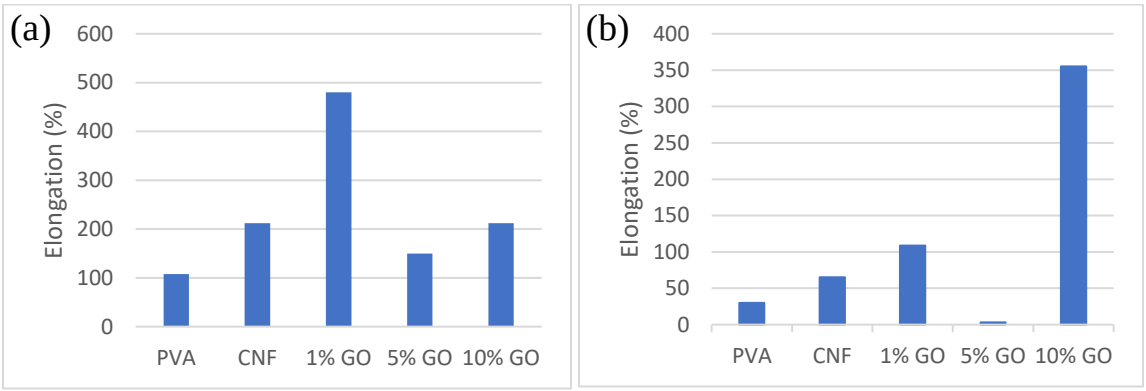

Figure 44. Percent elongation for unconditioned (a) and conditioned (b) cast samples.

The only take away from the cast samples that was expected was the decrease in elongation and increase elastic modulus and ultimate tensile strength for most samples. This meant the PVA samples lost water through the conditioning step as mechanical properties are influenced significantly due to water content. The data observed in the unconditioned samples was expected to show an increase in strength and stiffness with the addition of CNF, but GO loading was unknown. On one hand, the interfacial force transfer between the GO and PVA matrix would increase these two mechanical properties, but higher loading of GO also meant they held onto their water for much longer, as observed in the synthesis of samples, and FTIR and TGA testing. The

decreasing in stiffness and tensile strength for conditioned samples is also likely due to higher water content in the higher loading of CNF and GO.

The paper samples displayed an opposite trend to that of the conditioned cast samples, instead increasing in stiffness with the higher loading of nanofiller (Figure 45). This indicates that paper samples may have had a better conditioning process as the samples themselves are much thinner.

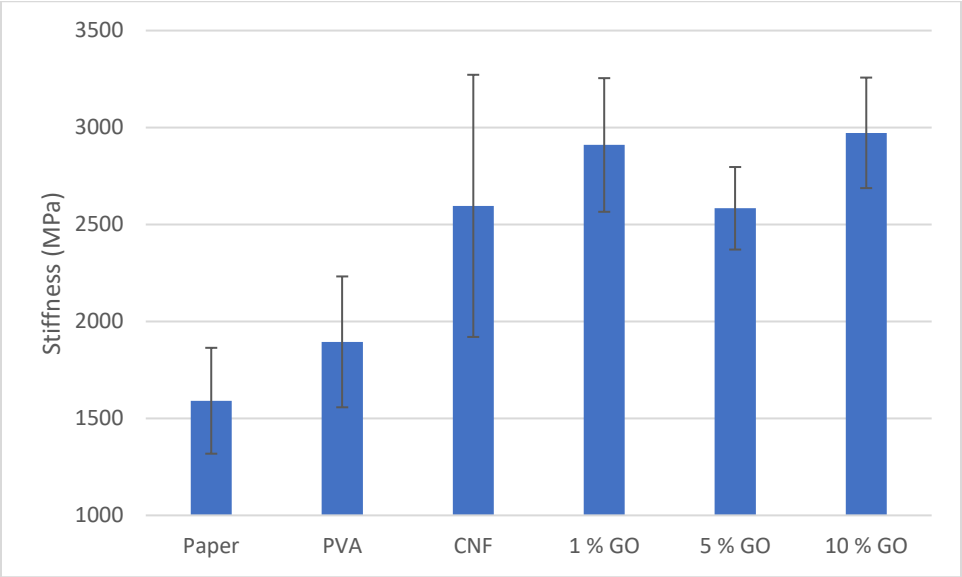

Figure 45. Elastic modulus/stiffness for each conditioned sample composition on paper.

The ultimate tensile data collected seems to follow a similar trend to the stiffness, generally increasing with the loading of CNF and GO. Interestingly, the 1 and 10% GO samples displayed lower strength than the CNF and 5% GO samples (Figure 46). This could be explained by either inconsistencies in the paper substrate or sample film as any imperfections could lead to inconsistent results.

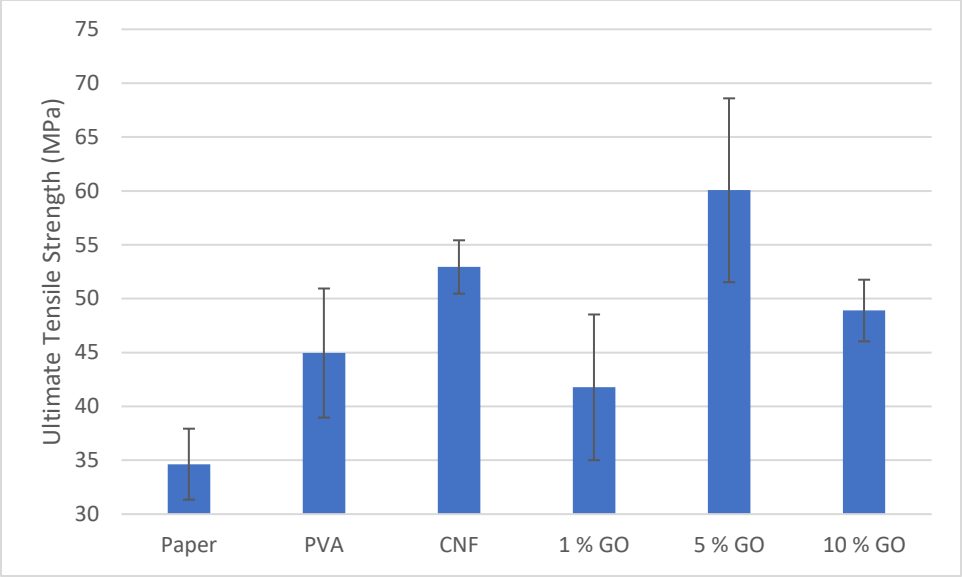

Figure 46. Ultimate tensile strength for each conditioned sample composition on paper.

Next, the elongation of the paper samples did not seem to change significantly, despite the stiffness and strength increases (Figure 47). This is likely due to the paper yielding and the low elongation of PVA at low water content.

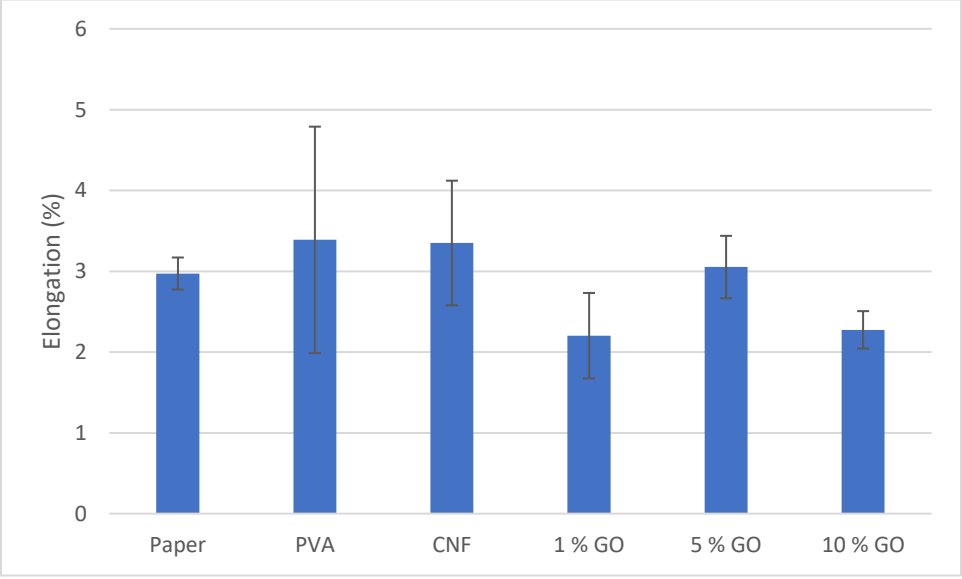

Figure 47. Percent elongation for each sample conditioned composition on paper.

Concerning mechanical property analysis, further work should be investigated, ensuring the water content of each sample is the same.

3.5. Solvent Permeation

3.5.1. Water Vapor Transmission

Figure 48 displays the loss of water for each sample composition as a function of time. The trend observed is that the paper sample took several days to produce steady-state water loss, while the coated paper samples essentially produced steady state results after the second day. From this data, it can be observed that each coated paper sample shows higher resistance than the paper control samples. The uncoated paper samples displayed high permeability, which was expected as paper by itself is not a good barrier to water vapor. The coated paper samples performed similarly to one another, but the CNF and 1% GO samples displayed higher water loss than the control PVA, and the 5 and 10% GO samples displayed lowest water loss. This data is not useable in this form, however, as it does not account for the thickness of the coating applied on the paper.

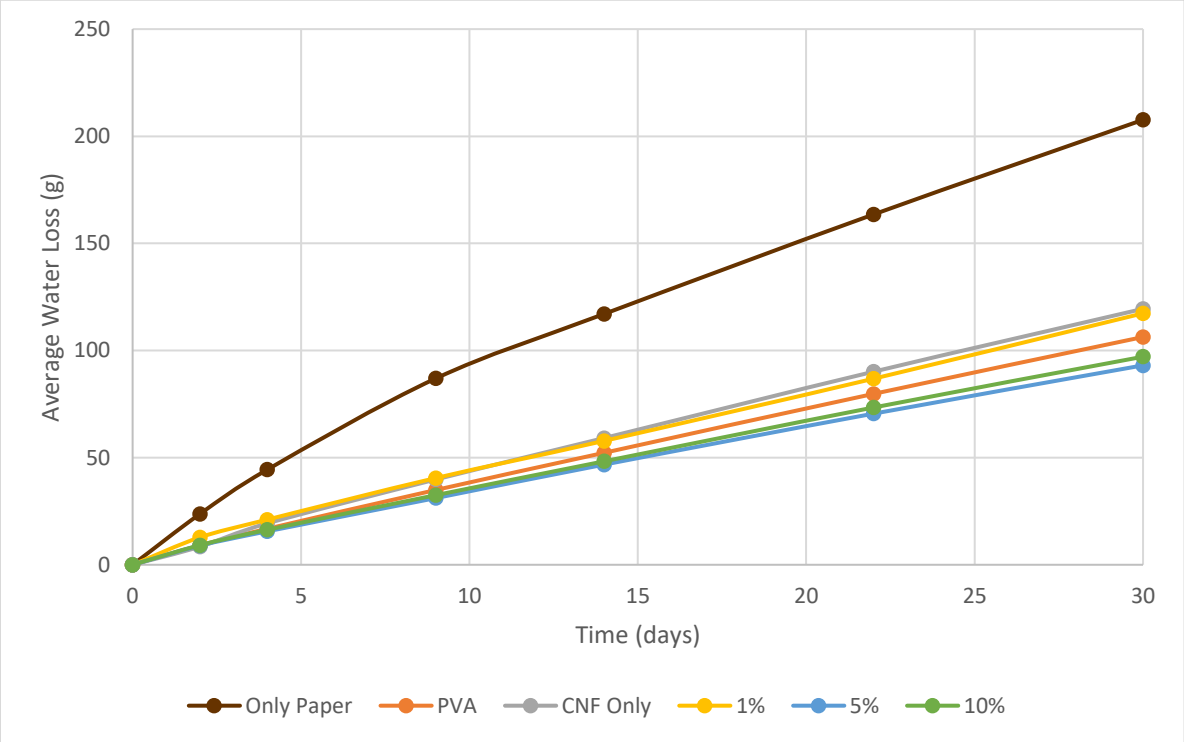

Figure 48. Average water loss for each sample composition over a period of 30 days.

Using the slopes of each sample composition, transmission rates were determined and applied to the equation for permeability. This effectively applied a normalization for the thickness of the sample films as everything used in the calculations for permeability is related to the sample area, relative humidities, and temperature of the environment. The uncovered samples were omitted for the purposes of clarity for the data of interest as the rate of water loss in the chamber was approximately 20 g/day. First, each sample maintained an average permeability between $2.5x10^{-11}$ - $3x10^{-11}$ g/(m·s·Pa), between expected literature values from $1.8x10^{-11}$ - $4.2x10^{-11}$ g/(m·s·Pa) [64]. The trend for permeability suggests the addition of CNF did not help decrease the transmission of water vapor through the samples. Additionally, 1% GO actually increased transmission through the sample, which was unexpected. Finally, as the loading of GO increased from one to five and ten percent, permeability decreased (Figure 49). This follows expected behavior as with a higher loading of graphene oxide, the tortuous path would be increased, furthering the distance water vapor needs to travel within the samples to reach the other side.

Unfortunately, there was a lot of error in the data collected as is visible in the magnitude of the error bars (Figure 49). This may be explained by issues regarding sample preparation such as barely visible holes in the paper, bleed through, and/or variations in coating thickness. Additionally, there could be error related to the jar method with which this experiment was performed.

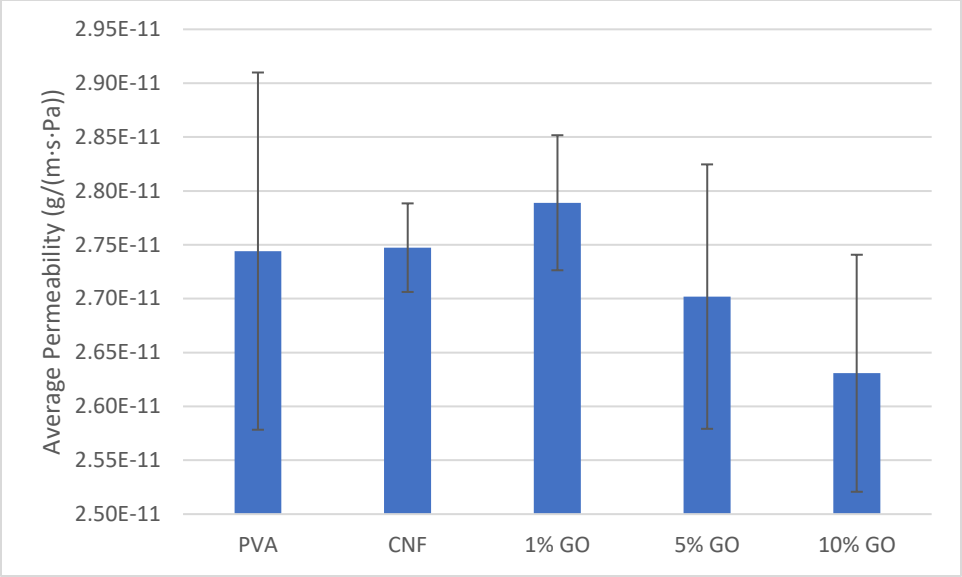

Figure 49. Average permeability calculated from the water vapor transmission rates.

Following this test, the paper substrate and coated paper samples were observed using optical microscopy to determine the surface features of the paper itself and ensure proper application of the drawdown. Specific areas of interest for the paper samples were holes and areas of reduced thickness (Figure 50). The holes were mostly visible when holding the paper up to light, but were easily missed, and areas of reduced thickness were difficult to observe with the naked eye. For the coated samples, no holes were observed, but areas of reduced thickness were common.

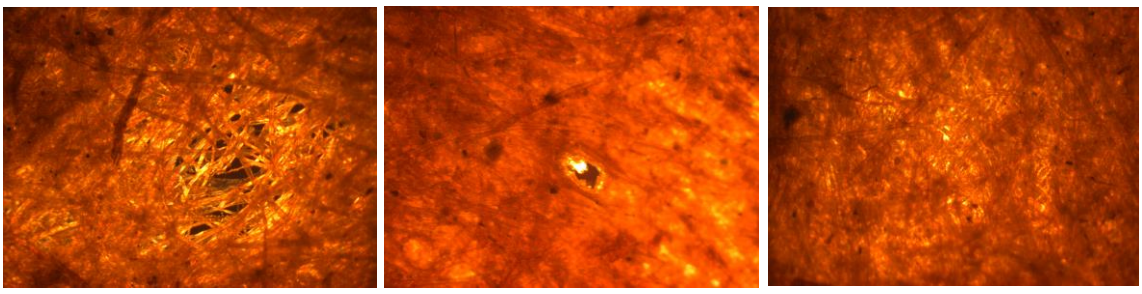

Figure 50. Easel paper substrate at 5x of two types of holes (a and b) and a thinner section (c).

3.5.2. Cobb Testing

For the unconditioned samples, the Cobb data suggests that the control PVA absorbed water most and the addition of CNF and GO helped to decrease the water absorbed (Figure 51). This was the expected behavior as PVA by itself has many hydroxyl groups that are open to hydrogen bond with water. As CNF is added, some of the hydroxyl groups are occupied, lowering the hydrophilicity of the PVA. Next, as GO is introduced, the higher GO-loading further occupies those hydroxyl groups, again lowering the hydrophilicity of the PVA.

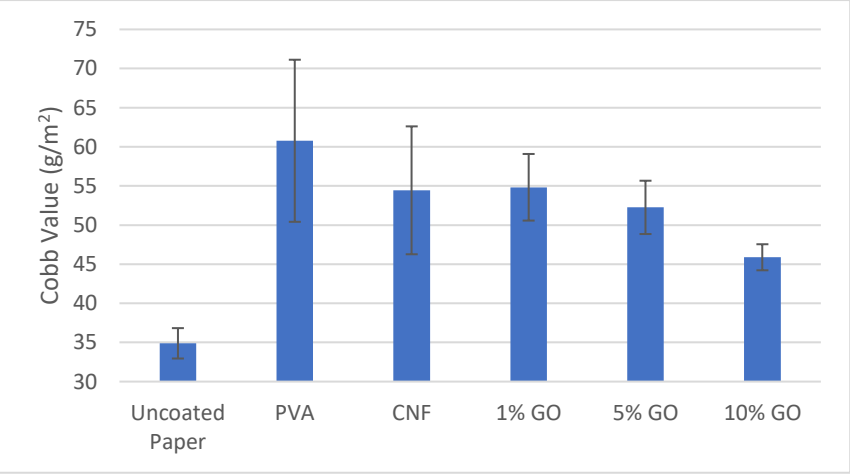

Figure 51. Cobb values representing water absorption for unconditioned paper samples.

For the conditioned samples, a different trend was observed. In this test, the control PVA absorbed water the least out of all coated samples, followed by an increase in hydrophilicity with both CNF and GO. As the loading of GO was increased, hydrophilicity decreased (Figure 52). The results may be explainable through the interruption of the hydrogen bonding and reduction of graphene oxide.

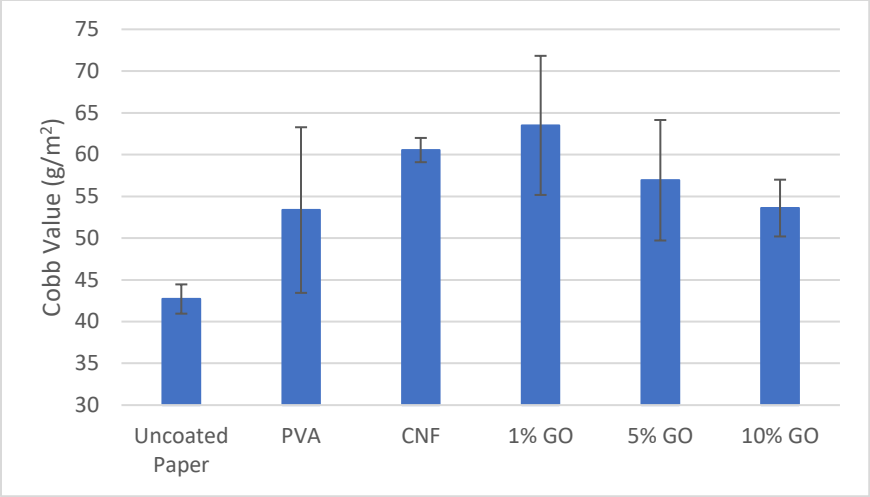

Figure 52. Cobb values representing water absorption for conditioned paper samples.

For both unconditioned and conditioned samples, uncoated paper seemed to perform exceedingly well despite paper typically being fairly hydrophilic [65]. This might be explainable by the difference in surface roughness between the paper itself and the smoothness of the coated samples. A high surface roughness would allow the water to avoid touching the entire surface of the paper, thus preventing the paper from getting fully saturated in a short period of time [66]. This same effect would not stop the transmission of water vapor or inhibit long-term saturation. Future Cobb testing data should be produced at a longer interval to ensure the paper displays this behavior.

The scale of error is again fairly large but may be accounted for in the methodology and/or sample imperfections. There were concerns that by reusing them, the conditioned samples would provide less reliable data, but one new sample of each composition was made, and the resulting trend was the same.

Finally, considering the oil testing, the uncoated paper absorbed the most, which was expected as oil permeates uncoated paper well despite typically being hydrophilic (Figure 53). Paper is good at absorbing low-viscosity fats such as cooking oils through

capillary action [67]. For the coated samples, there is an increase in absorbed oil with the CNF, but as GO is added, the oil absorbance of the samples decreases significantly. PVA by itself should be [68], so it is interesting that the Cobb values for the control PVA in the oil test are similar to that observed in the water tests. The increase in absorption from PVA to CNF was unexpected but is likely due to experimental error. The decrease in absorption as GO loading increases is likely due to path length for the oil increasing following the tortuosity model. This model applies even considering the partial reduction in graphene oxide as the graphene sheets still modify the path solvents need to travel.

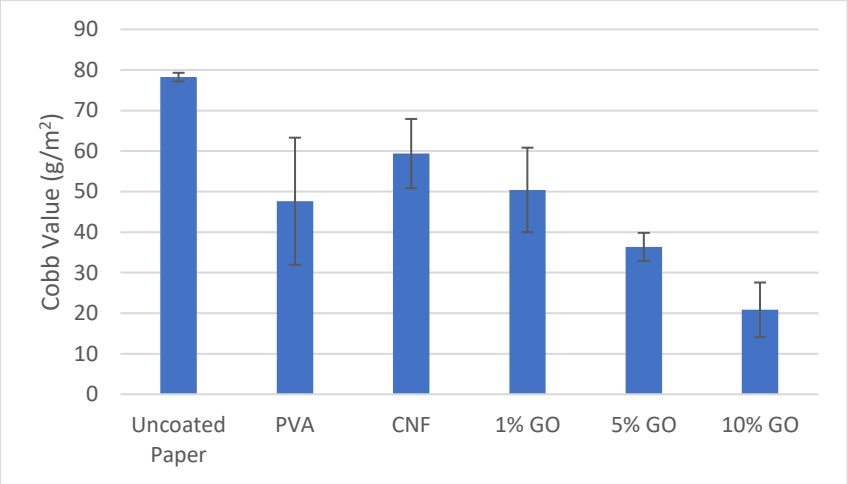

Figure 53. Cobb values representing oil absorption for conditioned paper samples.

3.5.3. Water and Oil Absorption

Water absorption testing revealed trends that aligned fairly well with Cobb and water vapor transmission. Figure 54 illustrates an initial high slope of mass increase, then a low slope and a plateau.

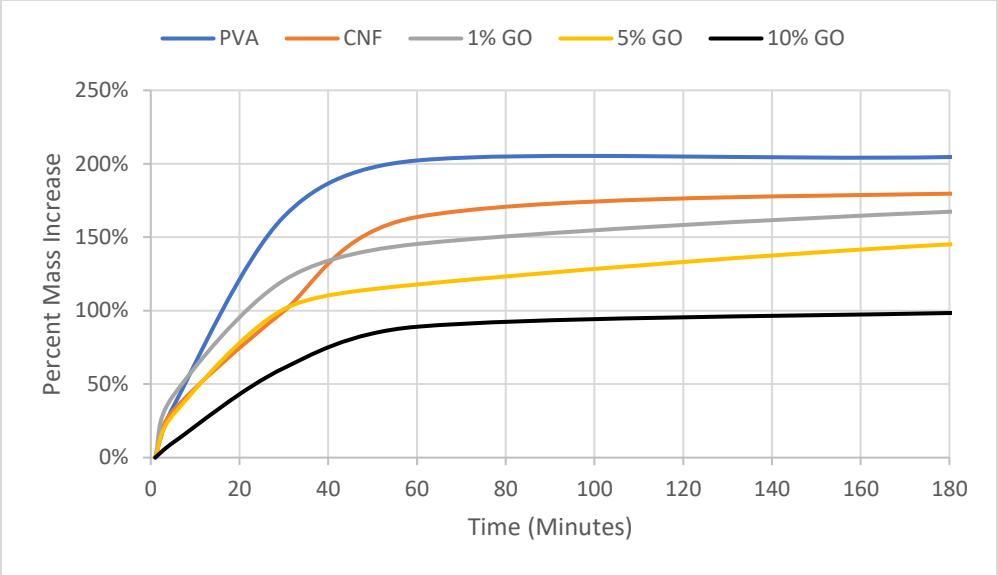

Figure 54. Average water absorption as a function of time in the first three hours.

From Figure 55, it was observed that the amount of water absorbed by each sample decreased as GO and higher loadings of GO were added. This trend was present because as more CNF and GO are added, the nanomaterials occupy spots in the PVA matrix that could take in water due to their hydrogen bonding.

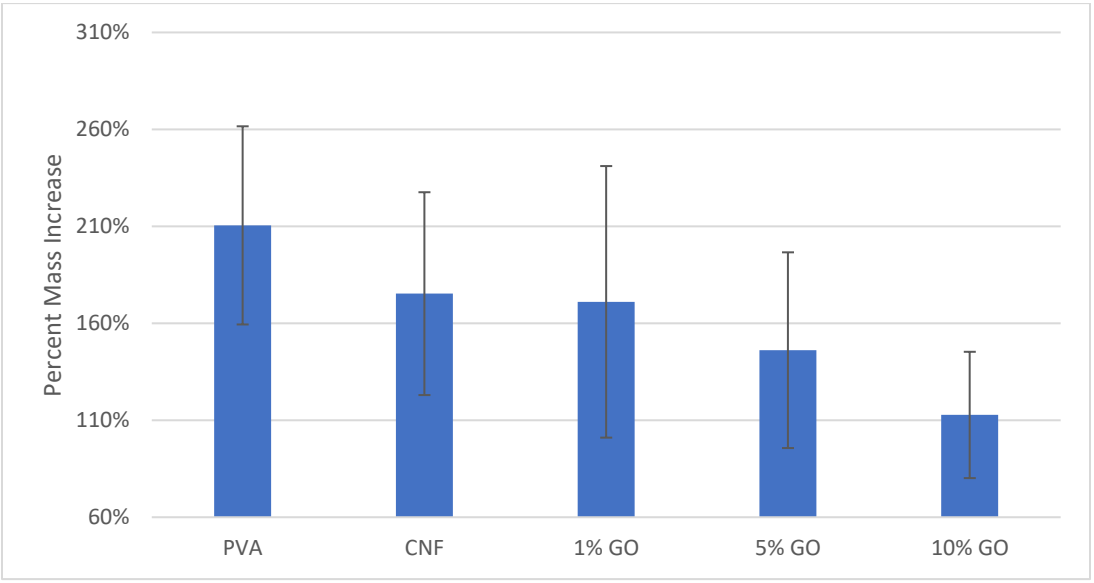

Figure 55. Average water absorption for each sample composition after 24 hours.

For the oil absorption test, the only real trend observable is that the control PVA took in much more vegetable oil than the other samples (Figure 56). This was unexpected as PVA has many hydroxyl groups, typically making it hydrophilic, but the trend observed is the opposite. It is possible PVA appears to absorb more oil when in fact the samples had curling issues that made patting off excess oil difficult.

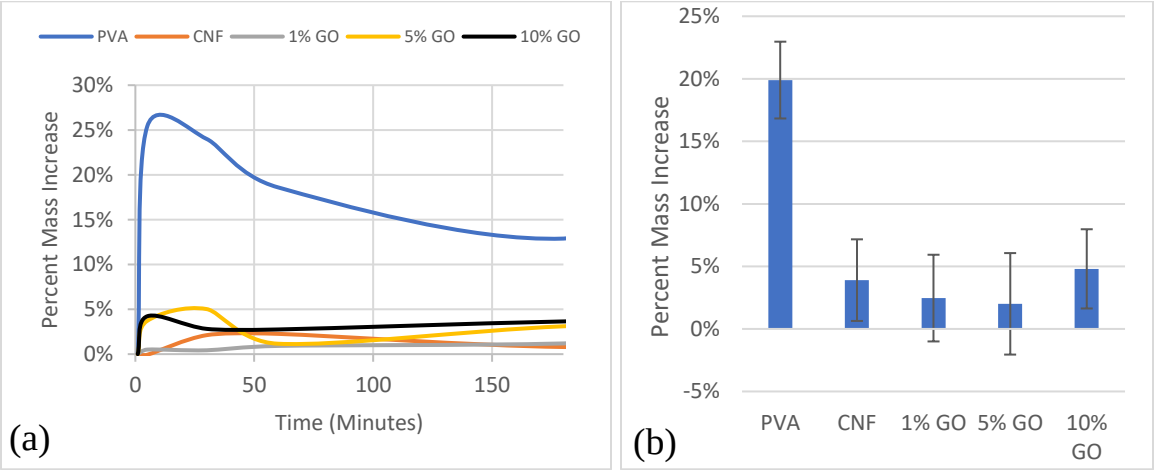

Figure 56. Average oil absorption as a function of time in the first three hours (a) and absorption at 24 hours (b).

3.6. Oxygen Permeability

Unfortunately, the data collected for oxygen permeability was not fully completed in triplicate as there were complications with samples and high failure rates. Initially, coated paper samples were used with the idea that glass drawdowns would introduce small holes as it was scraped from the glass due to the high adhesion to the substrate. Paper samples were used as the paper used could essentially be ignored in the calculations for oxygen permeability as oxygen could easily pass through it. It was also expected that the paper would not introduce any points of failure in the form film continuity, but the data suggests otherwise.

For the paper sample tests, out of 35 tests, 25 resulted in a test failure and only four gave results that were below 8 cc/(m^2*day). One data point was generated for each sample aside from 1% GO, which had nine tests and failed all of them. These results can be seen in Figure 57, and display little to no visible trend outside of possibly the addition of CNF and GO decreasing permeation. There is no particular trend to the samples and their failure rates. These results illustrate an issue with methodology, specifically the paper substrate used and sample preparation (Table 3). This unfortunately tracks with the previously observed continuity issues with the paper substrate.

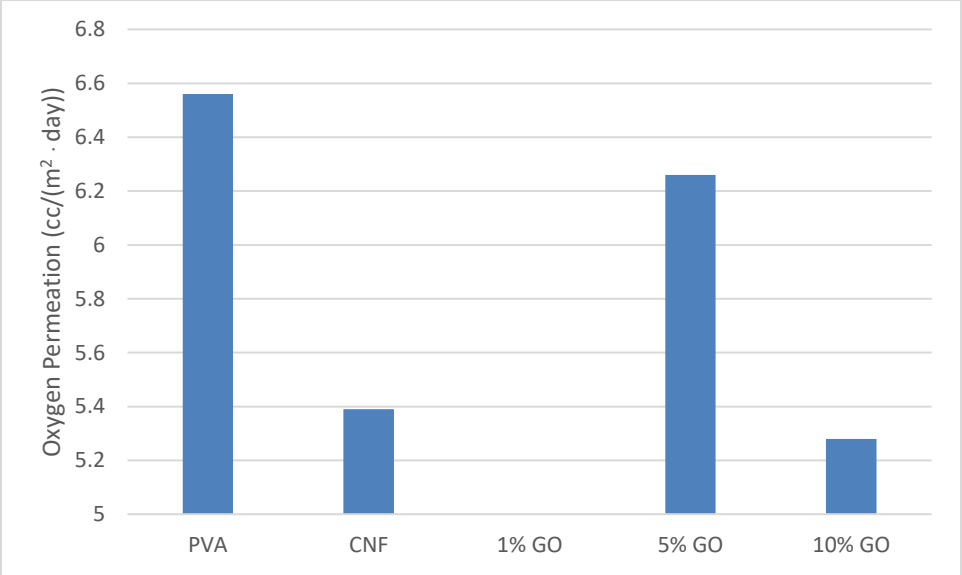

Figure 57. Oxygen transmission results for conditioned paper samples.

Table 3. Oxygen permeation testing failure rate of each sample composition.

Sample Composition	Number of Failed Tests	Number of Unusable Tests	Failure Rate
Control PVA	5	3	88.9%
CNF	3	2	83.3%
1% GO	9	0	100%
5% GO	7	2	90%
10% GO	1	3	80%

The weigh boat samples performed much better, with an overall failure rate of 0% for PVA, CNF, and 1% GO, and the only issues with 5 and 10% GO being errors in setup. Without the thickness calculations, it can be observed that oxygen transmission towards the beginning of the test is much higher than as the test continues (Figure 58). That is because with these samples there is a level of oxygen in the chamber and inside of the samples that needs time to be completely removed from the system. That means the important data is at what transmission the data plateaus at (Figure 59), which can then be multiplied by thickness to determine a comparable rate.

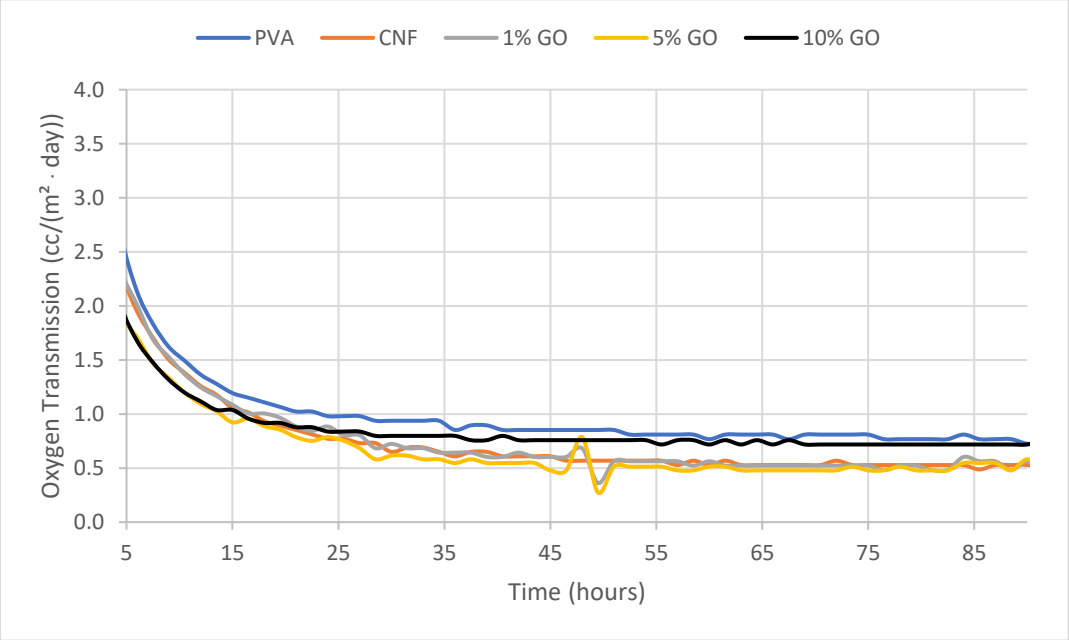

Figure 58. Oxygen transmission results without thickness calculations.

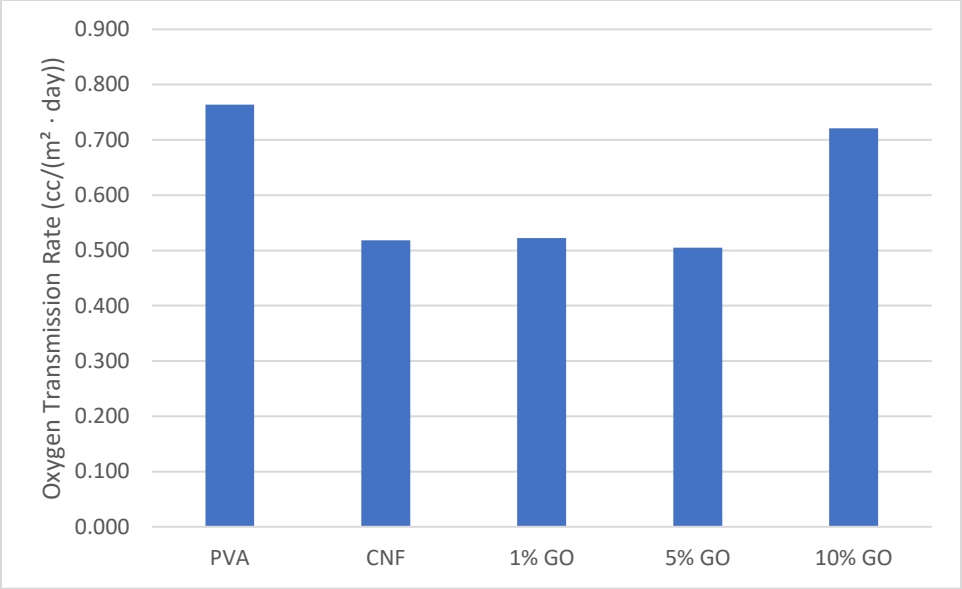

Figure 59. Steady-state averages for oxygen transmission rate from 65 to 85 hours.

After accounting for sample thickness, the trend appears to be that CNF decreased the oxygen permeation rate and GO increased permeation (Figure 60). This was unexpected as the behavior expected was that CNF and GO would both decrease permeation through the binding of hydroxyl groups, reducing the water content, and increasing the tortuous path. These results could be explained by a lack of control in conditioning as samples were tested in the order of PVA, CNF, 1% GO, 5% GO, then 10% GO. The desiccant used was fairly old and may not have worked properly. If that is the case, it would make sense that the oxygen permeation would increase the way the results indicate. Another way this test could have given bad results is if the conditioning step itself was not long enough or the humidity within the furnace was particularly high. From the water mass loss test, it was observed that the samples with higher loadings of GO held onto water for longer than the control. Unfortunately, triplicate results were not obtainable for these tests due to a lack of time, which could also be a source of error. Future work will need to be done in this area to ensure the quality of the data obtained.

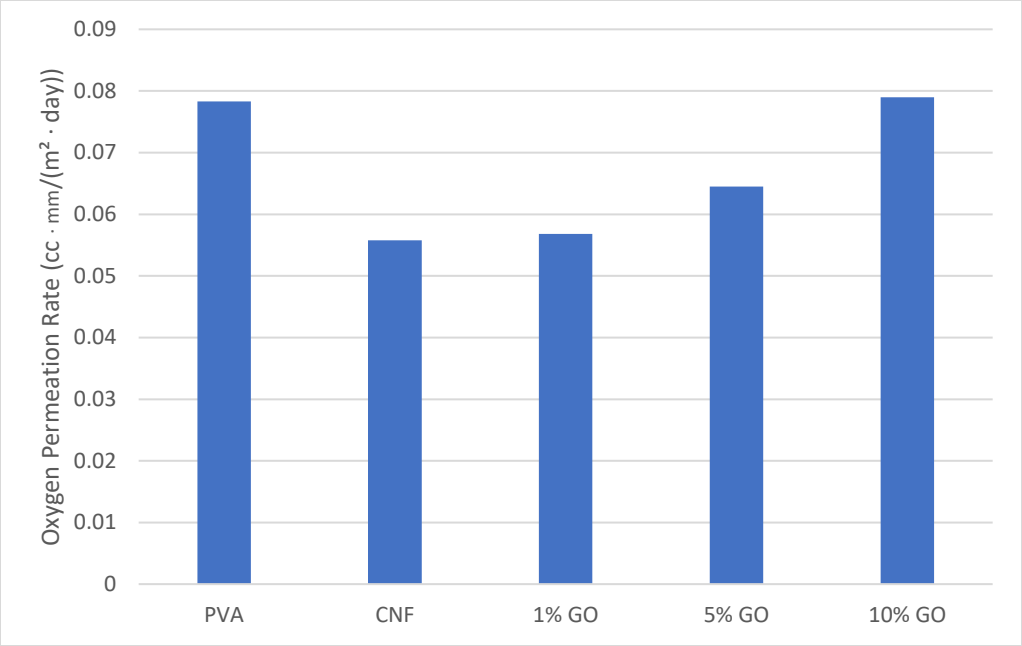

Figure 60. Oxygen permeation rates for conditioned samples accounting for sample thickness.

3.7. Microwave Testing

Figure 61 displays the increase in water temperature throughout the 15-second test in the microwave. By 15 seconds, 10% GO boiled over, while the control PVA, CNF, and 1% GO were only at 80°C. 5% GO also showed a significant increase in temperature over the other samples, finishing at 90°C. These results clearly indicate the microwave absorption in higher loading GO samples through higher water temperatures. While graphene is a good absorber of microwaves, typically graphene oxide is not due to functional groups. Following the observations of the other tests, it is indicated here that the graphene oxide has been partially reduced, increasing microwave absorption. Additional non-conditioned samples should be analyzed in future work to ensure this is the cause of these results.

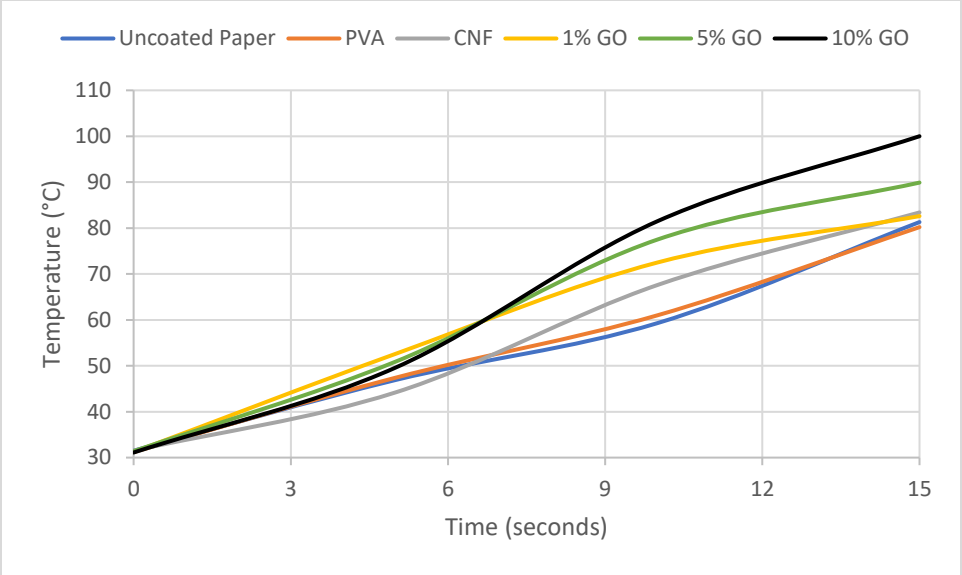

Figure 61. Sample temperatures using the microwave at full power for 15 seconds.

For the lower power test, Table 4 demonstrates that the only samples that boiled over and lost water were 5 and 10% GO over the entire 10-minute period. The 1% GO sample appeared to start boiling around a minute after 5% GO, but not violent enough to go over the sides of the vial or lose mass substantial enough to measure. The uncoated paper, PVA, and CNF samples were not observed as boiling throughout the entire test. These results again indicated the microwave absorption of rGO, this time with more extreme results.

Table 4. Water loss from boiling over 10 minutes at 10% microwave power.

Sample Composition	Water Loss (g)
PVA	0.0
CNF	0.0
1% GO	0.0
5% GO	3.2
10% GO	5.5

These observations were expected as graphene oxide is a modified version of graphene, which is highly thermally conductive, has high surface area, and dissipates electromagnetic energy extremely well [69]. Graphene oxide would be expected to

perform worse in terms of conductivity and energy dissipation. This is because oxidation level is inversely proportional to thermal conductivity due to the negative impact of hydroxyl and carbonyl groups on phonon-defect scattering (Figure 62) [59]. Because of this, graphene can have over thirty times the thermal conductivity of graphene oxide. Through the partial reduction of graphene oxide, the thermal conductivity should have increased as the fewer oxygen containing functional groups have less of a negative impact on thermal conductivity.

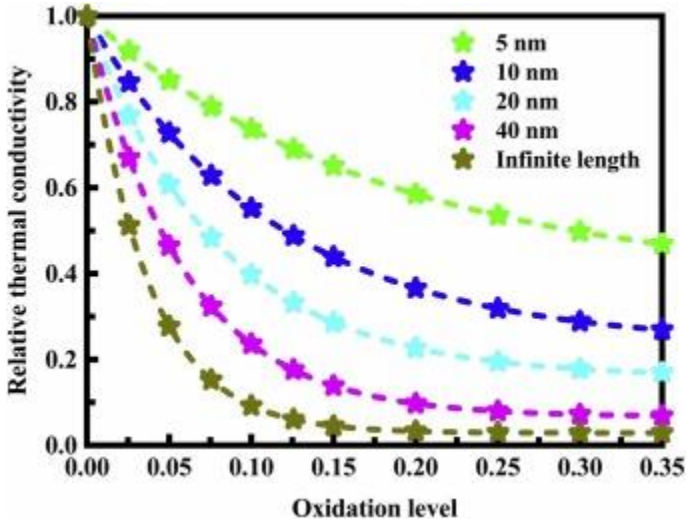

Figure 62. Thermal conductivity versus oxidation level of graphene oxide at various lengths [59].

3.8. Bacterial Inhibition

For the bacterial testing, no observable areas of inhibition were found for any of the samples tested (Figure 63). This is likely the case as despite GO and rGO having antibacterial properties, this test relies on diffusion of antibacterial agents out from the solid samples and onto the plate [70], [71]. It's likely that there simply was not enough moisture between the samples and the agar to facilitate enough diffusion to provide visible antibacterial zones. Further work should be performed to investigate the true antibacterial properties of the produced films.

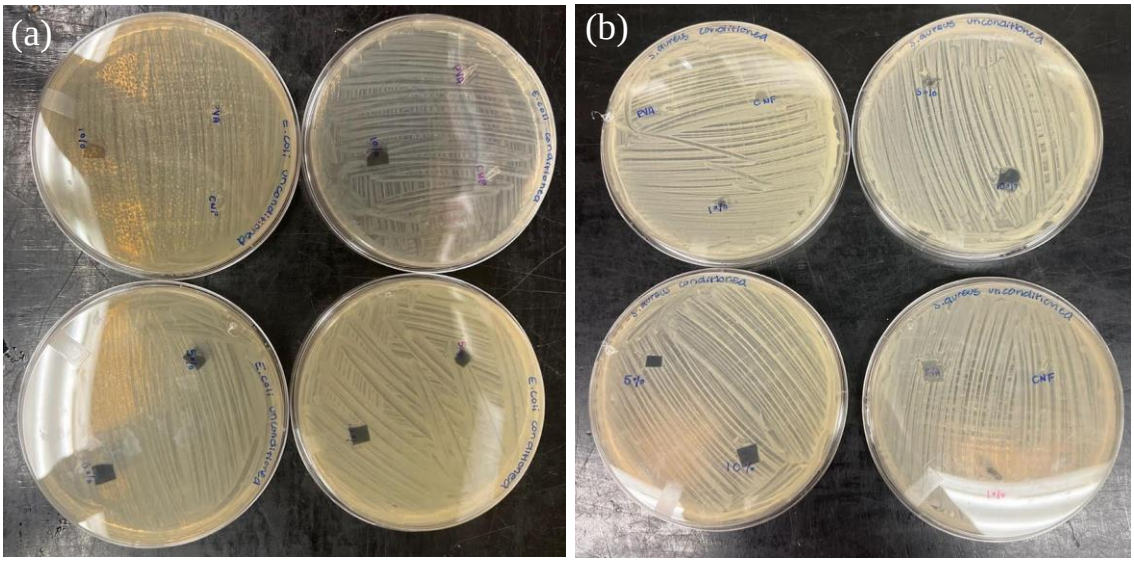

Figure 63. Final *E. Coli* (a) and *S. aureus* (b) petri dishes.

4. Conclusion

Food packaging has an industry-wide waste problem relating to packaging materials outliving their intended purpose by hundreds of years. With that being the case, plastic is by far the most commercially viable material in most cases due to its ease of manufacture, cost, and associated mechanical and barrier properties. This project focused on the synthesis of PVA/CNF/GO nanocomposites and the associated changes in color, barrier, mechanical, thermal, microwave, and antibacterial properties. The main observations present were an overall increase in barrier properties through the increase in hydrophobicity, reduction in water absorption, and decrease in oxygen permeability. Additionally, the reduction of graphene oxide was observed in both the conditioning and evaluation stages through visual confirmation, color, gloss, FTIR, and microwave analysis. Results for rheometry suggested that the shear thinning behavior expected with polymers was only slightly present due to the high water content of the liquid samples, and a significant shear-thinning behavior was observed with the 10% GO loading.

Absorbance testing using visible light indicated the reduction of graphene oxide due to conditioning through the widening of absorption bands. Color and gloss results indicated this change in reduction of graphene oxide through darkening of samples and increase in gloss. Contact angle testing displayed a reduction in hydrophilicity of PVA. Thermal gravimetric analysis observed an overall increase in degradation temperatures for both side-chain and backbone degradation. For differential scanning calorimetry testing, it was observed that glass transition and recrystallization temperatures increased while melting temperature and crystallinity decreased with the addition of higher loadings of GO. Mechanical properties were not observed as increasing with the addition of nanomaterials for cast samples, which may be a result of experimental conditions, however coated paper samples saw an approximate 50% increase in stiffness and 30% increase in ultimate tensile strength with high loading of GO when compared to the control PVA. Water vapor permeability was observed as decreasing with increasing loading of GO. For Cobb testing, water absorption displayed an increase with the introduction of CNF and GO for unconditioned samples, but the conditioned samples saw an increase. Oil Cobb results also displayed an overall decrease in absorption with the increased loading of GO. Water absorption testing displayed a clear decrease in absorption with higher loading of GO, almost up to a twofold reduction. Oxygen permeation results saw a large amount of error but displayed a reduction in permeability with the addition of CNF and GO. For microwave testing, it was observed that the GO had partially reduced from the conditioning process due to the microwave absorption properties of reduced GO. Finally, bacterial testing results were inconclusive as diffusion of GO was not possible with the methodology employed. Future work in mechanical, antibacterial, and electrical

properties of these compositions of nanocomposite would benefit the future of food packaging as a whole.

5. Future Work

The most important work that should be continued is degradation testing. Knowing how and when a specific composition of nanocomposite will degrade would be extremely useful in any deployment of PVA as a food packaging material. As PVA typically degrades through hydrolysis and bacterial means, environmental and biological degradation testing would be the most relevant. Some examples of this include accelerated weathering, dirt degradation, marine degradation, and bacterial and mycelial testing.

Another concept for future experimentation is exploring other forms of conditioning for the same sample compositions. Examples could include longer conditioning times at a lower temperature or using desiccation. This would allow for direct comparisons between samples containing graphene oxide and reduced graphene oxide or even comparisons between different levels of oxidation in the GO.

Next, an interesting idea for future work would be the incorporation of antibacterial and antifungal agents into the compositions of the nanocomposites. The liquid samples needed to be kept in a refrigerator as there was a threat of mold and microbial growth if samples were kept for too long at room temperature. To keep with the concept of degradable and renewable components, renewable additives such as citric acid or phytochemicals such as garlic juice (chemicals of plant origin) could be directly compared to common industry additives currently employed [72]–[74].

Next, food-safe nanomaterials such as chitin, chitosan, nanoclays, fullerenes, carbon nanodots, etc. and different matrix materials such as polylactic acid (PLA) could be observed in conjunction with cellulose nanofibers and graphene oxide for different interactions and property modifications. It may also be a good idea to switch from the somewhat irregular easel paper to a more uniform uncoated paper substrate. Additionally, FTIR or another chemical characterization method should be used to determine any additives in the paper.

To improve and support some of the conclusions made in this project, additional work following may include UV-vis testing with quartz slides and drawdown bars as that would ensure an even thickness between samples. Additionally, a control test performed with official water vapor vapometers would be good to ensure the results using the Ball jars are repeatable. In this vein, a longer Cobb test would be excellent for the uncoated paper samples specifically to ensure that the initial hydrophobic behavior is not long-lasting.

Finally, additional tests regarding electrical properties such as using a four-point probe would be good for the characterization of the nanocomposites. This could be useful for these types of nanocomposites to determine oxidization level of the graphene oxide or for application of CNF and GO in other fields aside from food packaging.

6. Bibliography

[1] *Global Plastics Outlook*. OECD, 2022. doi: 10.1787/de747aef-en.

[2] I. H. Siahaan and O. Soegihardjo, "Sustainability design of press machine for waste plastic bottle with electric motor," *IOP Conf Ser Mater Sci Eng*, vol. 1034, no. 1, p. 012007, Feb. 2021, doi: 10.1088/1757-899X/1034/1/012007.

[3] United States Environmental Protection Agency, "National Overview: Facts and Figures on Materials, Wastes and Recycling ," *epa.gov*, Jul. 31, 2022.

[4] A. Pellis, E. Herrero Acero, L. Gardossi, V. Ferrario, and G. M. Guebitz, "Renewable building blocks for sustainable polyesters: new biotechnological routes for greener plastics," *Polym Int*, vol. 65, no. 8, pp. 861–871, Aug. 2016, doi: 10.1002/PI.5087.

[5] S. Lanzalaco and B. G. Molina, "Polymers and Plastics Modified Electrodes for Biosensors: A Review," *Molecules 2020, Vol. 25, Page 2446*, vol. 25, no. 10, p. 2446, May 2020, doi: 10.3390/MOLECULES25102446.

[6] G. J. He, Q. Liu, and M. R. Thompson, "Characterization of structure and properties of thermoplastic potato starch film surface cross-linked by UV irradiation," *Starch - Stärke*, vol. 65, no. 3–4, pp. 304–311, Mar. 2013, doi: 10.1002/STAR.201200097.

[7] M. Hauschild, R. Rosenbaum, and S. I. Olsen, *Life Cycle Assessment: Theory and Practice*. Cham: Springer International Publishing, 2018. doi: 10.1007/978-3-319-56475-3.

[8] T. T. Wei, K. J. Wu, S. L. Lee, and Y. H. Lin, "Chemical recycling of post-consumer polymer waste over fluidizing cracking catalysts for producing chemicals and hydrocarbon fuels," *Resour Conserv Recycl*, vol. 54, no. 11, pp. 952–961, Sep. 2010, doi: 10.1016/J.RESCONREC.2010.02.002.

[9] S. Utekar, S. V K, N. More, and A. Rao, "Comprehensive study of recycling of thermosetting polymer composites – Driving force, challenges and methods," *Compos B Eng*, vol. 207, p. 108596, Feb. 2021, doi: 10.1016/J.COMPOSITESB.2020.108596.

[10] J. Jiang, T. L. Marsh, and P. R. Tozer, "Policy induced price volatility transmission: Linking the U.S. crude oil, corn and plastics markets," *Energy Econ*, vol. 52, pp. 217–227, Dec. 2015, doi: 10.1016/j.eneco.2015.10.008.

[11] N. Hiraishi *et al.*, "Susceptibility of a polycaprolactone-based root canal-filling material to degradation. III. Turbidimetric evaluation of enzymatic hydrolysis," *J Endod*, vol. 33, no. 8, pp. 952–6, Aug. 2007, doi: 10.1016/j.joen.2007.05.004.

[12] M. K. Patel *et al.*, "Second-generation bio-based plastics are becoming a reality – Non-renewable energy and greenhouse gas (GHG) balance of succinic acid-based plastic end products made from lignocellulosic

biomass," *Biofuels, Bioproducts and Biorefining*, vol. 12, no. 3, pp. 426–441, May 2018, doi: 10.1002/BBB.1849.

[13] R. G. C. Silva, T. F. Ferreira, and É. R. Borges, "Identification of potential technologies for 1,4-Butanediol production using prospecting methodology," *Journal of Chemical Technology & Biotechnology*, vol. 95, no. 12, pp. 3057–3070, Dec. 2020, doi: 10.1002/JCTB.6518.

[14] V. Siracusa, P. Rocculi, S. Romani, and M. D. Rosa, "Biodegradable polymers for food packaging: a review," *Trends Food Sci Technol*, vol. 19, no. 12, pp. 634–643, Dec. 2008, doi: 10.1016/J.TIFS.2008.07.003.

[15] S. V. G. Kumari, K. Pakshirajan, and G. Pugazhenthi, "Recent advances and future prospects of cellulose, starch, chitosan, polylactic acid and polyhydroxyalkanoates for sustainable food packaging applications," *Int J Biol Macromol*, vol. 221, pp. 163–182, Nov. 2022, doi: 10.1016/J.IJBIOMAC.2022.08.203.

[16] A. Kathuria, M. G. Abiad, and R. Auras, "Toughening of poly(l-lactic acid) with Cu3BTC2 metal organic framework crystals," *Polymer (Guildf)*, vol. 54, no. 26, pp. 6979–6986, Dec. 2013, doi: 10.1016/J.POLYMER.2013.11.005.

[17] Y. Bin, B. Yang, and H. Wang, "The effect of a small amount of modified microfibrillated cellulose and ethylene–glycidyl methacrylate copolymer on the crystallization behaviors and mechanical properties of polylactic acid,"

Polymer Bulletin, vol. 75, no. 8, pp. 3377–3394, Aug. 2018, doi: 10.1007/S00289-017-2215-8/FIGURES/14.

[18] A. Kathuria and S. Zhang, "Sustainable and Repulpable Barrier Coatings for Fiber-Based Materials for Food Packaging: A Review," *Front Mater*, vol. 9, p. 929501, Jul. 2022, doi: 10.3389/FMATS.2022.929501/BIBTEX.

[19] S. P. Bangar, W. S. Whiteside, A. O. Ashogbon, and M. Kumar, "Recent advances in thermoplastic starches for food packaging: A review," *Food Packag Shelf Life*, vol. 30, p. 100743, Dec. 2021, doi: 10.1016/J.FPSL.2021.100743.

[20] N. Asim, M. Badiei, and M. Mohammad, "Recent advances in cellulose-based hydrophobic food packaging," *Emergent Materials 2021 5:3*, vol. 5, no. 3, pp. 703–718, Nov. 2021, doi: 10.1007/S42247-021-00314-2.

[21] "Components and structure of lignocellulosic plant cell walls.... | Download Scientific Diagram." https://www.researchgate.net/figure/Components-and-structure-of-lignocellulosic-plant-cell-walls-Lignocellulosic-plant-cell_fig1_340936827 (accessed Aug. 18, 2023).

[22] F. Shahidi, J. K. V. Arachchi, and Y. J. Jeon, "Food applications of chitin and chitosans," *Trends Food Sci Technol*, vol. 10, no. 2, pp. 37–51, Feb. 1999, doi: 10.1016/S0924-2244(99)00017-5.

[23] P. Darmadji and M. Izumimoto, "Effect of chitosan in meat preservation," *Meat Sci*, vol. 38, no. 2, pp. 243–254, 1994, doi: 10.1016/0309-1740(94)90114-7.

[24] J. Nilsen-Nygaard, S. P. Strand, K. M. Vårum, K. I. Draget, and C. T. Nordgård, “Chitosan: Gels and interfacial properties,” *Polymers (Basel)*, vol. 7, no. 3, pp. 552–579, 2015, doi: 10.3390/POLYM7030552.

[25] S. A. A. Mohamed, M. El-Sakhawy, and M. A. M. El-Sakhawy, “Polysaccharides, Protein and Lipid -Based Natural Edible Films in Food Packaging: A Review,” *Carbohydr Polym*, vol. 238, p. 116178, Jun. 2020, doi: 10.1016/J.CARBPOL.2020.116178.

[26] J. V. Steinle, “Carnauba wax: An Expedition to Its Source,” *Ind Eng Chem*, vol. 28, no. 9, pp. 1004–1008, Sep. 1936, doi: 10.1021/IE50321A003/ASSET/IE50321A003.FP.PNG_V03.

[27] M. Y. Bhat, T. A. Dar, and L. R. Singh, “Casein Proteins: Structural and Functional Aspects,” in *Milk Proteins - From Structure to Biological Properties and Health Aspects*, InTech, 2016. doi: 10.5772/64187.

[28] L. K. Massey, “Permeability Properties of Plastics and Elastomers : a Guide to Packaging and Barrier Materials.,” p. 616, 2002.

[29] C. F. Mok, Y. C. Ching, F. Muhamad, N. A. Abu Osman, N. D. Hai, and C. R. Che Hassan, “Adsorption of Dyes Using Poly(vinyl alcohol) (PVA) and PVA-Based Polymer Composite Adsorbents: A Review,” *J Polym Environ*, vol. 28, no. 3, pp. 775–793, Mar. 2020, doi: 10.1007/S10924-020-01656-4.

[30] L. Quagliato, C. Jang, and N. Kim, “Manufacturing process and mechanical properties characterization for steel skin – Carbon fiber reinforced polymer

core laminate structures," *Compos Struct*, vol. 209, pp. 1–12, Feb. 2019, doi: 10.1016/J.COMPSTRUCT.2018.10.078.

[31] O. Kanoun, A. Benchirouf, A. Sanli, and A. Bouhamed, "Potential of Flexible Carbon Nanotube Films for High Performance Strain and Pressure Sensors 'CENTAUR' Ceramics with sensing capabilities for high temperature applications View project Synthesis and Characterization of Electrospun Flexible Piezoresistive Force Sensors for the Applications of Human Body Motion Monitoring View project." [Online]. Available: https://www.researchgate.net/publication/281438116

[32] R. J. Peláez *et al.*, "Enhanced reactivity and related optical changes of Ag nanoparticles on amorphous Al2O3 supports," *Nanotechnology*, vol. 24, no. 36, p. 365702, Aug. 2013, doi: 10.1088/0957-4484/24/36/365702.

[33] X. Yin *et al.*, "Recent Progress in 1D Nanostructures Reinforced Carbon/Carbon Composites," *Adv Funct Mater*, vol. 32, no. 35, p. 2204965, Aug. 2022, doi: 10.1002/ADFM.202204965.

[34] C. Wang, J. Wu, P. Cheng, L. Xu, and S. Zhang, "Nanocomposite polymer blend membrane molecularly re-engineered with 2D metal-organic framework nanosheets for efficient membrane CO2 capture," *J Memb Sci*, vol. 685, Nov. 2023, doi: 10.1016/J.MEMSCI.2023.121950.

[35] S. C. Tjong, *Nanocrystalline materials : their synthesis-structure-property relationships and applications*, Second edition. in Elsevier insights. London: Elsevier, 2014.

[36] S. Talebian, T. Rodrigues, J. das Neves, B. Sarmento, R. Langer, and J. Conde, “Facts and Figures on Materials Science and Nanotechnology Progress and Investment,” *ACS Nano*, vol. 15, no. 10, pp. 15940–15952, Oct. 2021, doi: 10.1021/acsnano.1c03992.

[37] “Vapour Permeation Barrier,” *Glass Flake Limited*, 2022.

[38] J. Cowen and A. F. Hepp, *Synthesis and characterization of cobalt-containing nanoparticles on alumina: a potential catalyst for gas-to-liquid fuels production*. in NASA/TM ; 2016-219138. Cleveland, Ohio: National Aeronautics and Space Administration, Glenn Research Center, 2016.

[39] D. Yu *et al.*, “*In situ* hydrosilane reduction and preparation of gold nanoparticle–gel glass composites with nonlinear optical properties,” *J Mater Chem C Mater*, vol. 6, no. 21, pp. 5624–5629, 2018, doi: 10.1039/C8TC00913A.

[40] M. Baneshi, H. Gonome, A. Komiya, and S. Maruyama, “The effect of particles size distribution on aesthetic and thermal performances of polydisperse TiO2 pigmented coatings: Comparison between numerical and experimental results,” *J Quant Spectrosc Radiat Transf*, vol. 113, no. 8, pp. 594–606, May 2012, doi: 10.1016/j.jqsrt.2012.02.006.

[41] S. Young Park *et al.*, “Eco-friendly carbon-nanodot-based fluorescent paints for advanced photocatalytic systems,” *Sci Rep*, vol. 5, no. 1, p. 12420, Dec. 2015, doi: 10.1038/srep12420.

[42] K. Jiang *et al.*, “Preparation of Multicolor Photoluminescent Carbon Dots by Tuning Surface States,” *Nanomaterials 2019, Vol. 9, Page 529*, vol. 9, no. 4, p. 529, Apr. 2019, doi: 10.3390/NANO9040529.

[43] S. M. Noorbakhsh-Soltani, M. M. Zerafat, and S. Sabbaghi, “A comparative study of gelatin and starch-based nano-composite films modified by nano-cellulose and chitosan for food packaging applications,” *Carbohydr Polym*, vol. 189, pp. 48–55, Jun. 2018, doi: 10.1016/j.carbpol.2018.02.012.

[44] Z. M. Wang, H. Nakajima, E. Manias, and T. C. Chung, “Exfoliated PP/Clay Nanocomposites Using Ammonium-Terminated PP as the Organic Modification for Montmorillonite,” *Macromolecules*, vol. 36, no. 24, pp. 8919–8922, Dec. 2003, doi: 10.1021/ma035291l.

[45] G. Y. Toh, H. L. Ong, K. Bindumadhavan, and R. Doong, “Physicochemical properties of reduced graphite oxide conglomerated polyethylene nanocomposites,” *Polym Int*, vol. 67, no. 12, pp. 1638–1647, Dec. 2018, doi: 10.1002/pi.5687.

[46] I. Echeverría, M. E. López-Caballero, M. C. Gómez-Guillén, A. N. Mauri, and M. P. Montero, “Active nanocomposite films based on soy proteins-montmorillonite- clove essential oil for the preservation of refrigerated bluefin tuna (Thunnus thynnus) fillets,” *Int J Food Microbiol*, vol. 266, pp. 142–149, Feb. 2018, doi: 10.1016/j.ijfoodmicro.2017.10.003.

[47] S. Tang *et al.*, “Degradable and Photocatalytic Antibacterial Au-TiO2/Sodium Alginate Nanocomposite Films for Active Food Packaging,”

Nanomaterials, vol. 8, no. 11, p. 930, Nov. 2018, doi: 10.3390/nano8110930.

[48] Y. A. Arfat, M. Ejaz, H. Jacob, and J. Ahmed, "Deciphering the potential of guar gum/Ag-Cu nanocomposite films as an active food packaging material," *Carbohydr Polym*, vol. 157, pp. 65–71, Feb. 2017, doi: 10.1016/j.carbpol.2016.09.069.

[49] S. Mishra, P. S. Kharkar, and A. M. Pethe, "Biomass and waste materials as potential sources of nanocrystalline cellulose: Comparative review of preparation methods (2016 – Till date)," *Carbohydr Polym*, vol. 207, pp. 418–427, Mar. 2019, doi: 10.1016/J.CARBPOL.2018.12.004.

[50] R. Ikram, B. M. Jan, and W. Ahmad, "An overview of industrial scalable production of graphene oxide and analytical approaches for synthesis and characterization," *Journal of Materials Research and Technology*, vol. 9, no. 5, pp. 11587–11610, Sep. 2020, doi: 10.1016/J.JMRT.2020.08.050.

[51] K. Z. Donato *et al.*, "Graphene oxide classification and standardization," *Scientific Reports 2023 13:1*, vol. 13, no. 1, pp. 1–9, Apr. 2023, doi: 10.1038/s41598-023-33350-5.

[52] P. Cazón, M. Vázquez, and G. Velázquez, "Regenerated cellulose films with chitosan and polyvinyl alcohol: Effect of the moisture content on the barrier, mechanical and optical properties," *Carbohydr Polym*, vol. 236, May 2020, doi: 10.1016/j.carbpol.2020.116031.

[53] J. Z. Xu *et al.*, “Graphene oxide nanosheet induced intrachain conformational ordering in a semicrystalline polymer,” *Journal of Physical Chemistry Letters*, vol. 3, no. 4, pp. 530–535, Feb. 2012, doi: 10.1021/JZ300062Z/SUPPL_FILE/JZ300062Z_SI_001.PDF.

[54] P. Daripa and R. Mishra, “Modeling shear thinning polymer flooding using a dynamic viscosity model,” *Physics of Fluids*, vol. 35, no. 4, Apr. 2023, doi: 10.1063/5.0145061.

[55] P. Kumar, U. N. Maiti, K. E. Lee, and S. O. Kim, “Rheological properties of graphene oxide liquid crystal,” *Carbon N Y*, vol. 80, no. 1, pp. 453–461, Dec. 2014, doi: 10.1016/J.CARBON.2014.08.085.

[56] V. Agarwal and P. B. Zetterlund, “Strategies for reduction of graphene oxide – A comprehensive review,” *Chemical Engineering Journal*, vol. 405, p. 127018, Feb. 2021, doi: 10.1016/J.CEJ.2020.127018.

[57] A. S. Beliaeva and G. E. Romanova, “Design features of the glossmeter system,” *J Phys Conf Ser*, vol. 1421, no. 1, p. 012065, Dec. 2019, doi: 10.1088/1742-6596/1421/1/012065.

[58] H. Zhang *et al.*, “Conjugated polymer with dynamic and thermoreversible hydrogen bonding on the backbone,” *Polymer (Guildf)*, vol. 203, p. 122787, Aug. 2020, doi: 10.1016/j.polymer.2020.122787.

[59] J. Chen and L. Li, “Effect of oxidation degree on the thermal properties of graphene oxide,” *Journal of Materials Research and Technology*, vol. 9, no. 6, pp. 13740–13748, Nov. 2020, doi: 10.1016/j.jmrt.2020.09.092.

[60] Z. Peng and L. X. Kong, “A thermal degradation mechanism of polyvinyl alcohol/silica nanocomposites,” *Polym Degrad Stab*, vol. 92, no. 6, pp. 1061–1071, Jun. 2007, doi: 10.1016/J.POLYMDEGRADSTAB.2007.02.012.

[61] H. Akhina *et al.*, “Influence of reduced graphene oxide on flow behaviour, glass transition temperature and secondary crystallinity of plasticized poly(vinyl chloride),” *RSC Adv*, vol. 10, no. 49, pp. 29247–29256, Aug. 2020, doi: 10.1039/d0ra04560h.

[62] E. Sharifzadeh and K. Cheraghi, “Temperature-affected mechanical properties of polymer nanocomposites from glassy-state to glass transition temperature,” *Mechanics of Materials*, vol. 160, Sep. 2021, doi: 10.1016/J.MECHMAT.2021.103990.

[63] B. J. Holland and J. N. Hay, “The thermal degradation of poly(vinyl alcohol),” *Polymer (Guildf)*, vol. 42, no. 16, pp. 6775–6783, Jul. 2001, doi: 10.1016/S0032-3861(01)00166-5.

[64] P. Cazón, M. Vázquez, and G. Velazquez, “Novel composite films based on cellulose reinforced with chitosan and polyvinyl alcohol: Effect on mechanical properties and water vapour permeability,” *Polym Test*, vol. 69, pp. 536–544, Aug. 2018, doi: 10.1016/J.POLYMERTESTING.2018.06.016.

[65] Z. Tang, D. W. Hess, and V. Breedveld, “Fabrication of oleophobic paper with tunable hydrophilicity by treatment with non-fluorinated chemicals,” *J*

Mater Chem A Mater, vol. 3, no. 28, pp. 14651–14660, Jul. 2015, doi: 10.1039/C5TA03520A.

[66] C. C. de Foggi, A. L. Machado, C. A. Zamperini, D. Fernandes, A. F. Wady, and C. E. Vergani, "Effect of surface roughness on the hydrophobicity of a denture-base acrylic resin and Candida albicans colonization," *J Investig Clin Dent*, vol. 7, no. 2, pp. 141–148, May 2016, doi: 10.1111/jicd.12125.

[67] G. S. Gerlero, A. R. Valdez, R. Urteaga, and P. A. Kler, "Validity of Capillary Imbibition Models in Paper-Based Microfluidic Applications," *Transp Porous Media*, vol. 141, no. 2, pp. 359–378, Jan. 2022, doi: 10.1007/S11242-021-01724-W.

[68] B. Xue *et al.*, "Underwater superoleophobicity of poly(vinyl alcohol) gel-coated/micro-arc oxidized Al mesh for oil-water separation," *Mater Chem Phys*, vol. 292, Dec. 2022, doi: 10.1016/J.MATCHEMPHYS.2022.126817.

[69] F. Meng *et al.*, "Graphene-based microwave absorbing composites: A review and prospective," *Compos B Eng*, vol. 137, pp. 260–277, Mar. 2018, doi: 10.1016/J.COMPOSITESB.2017.11.023.

[70] H. Zheng *et al.*, "Antibacterial applications of graphene oxides: structure-activity relationships, molecular initiating events and biosafety," *Sci Bull (Beijing)*, vol. 63, no. 2, pp. 133–142, Jan. 2018, doi: 10.1016/J.SCIB.2017.12.012.

[71] S. Abazari, A. Shamsipur, and H. R. Bakhsheshi-Rad, “Reduced graphene oxide (RGO) reinforced Mg biocomposites for use as orthopedic applications: Mechanical properties, cytocompatibility and antibacterial activity,” *Journal of Magnesium and Alloys*, vol. 10, no. 12, pp. 3612–3627, Dec. 2022, doi: 10.1016/J.JMA.2021.09.016.

[72] A. M. Laury *et al.*, “Validation of a lactic acid- and citric acid-based antimicrobial product for the reduction of Escherichia coli O157:H7 and Salmonella on beef tips and whole chicken carcasses,” *J Food Prot*, vol. 72, no. 10, pp. 2208–2211, 2009, doi: 10.4315/0362-028X-72.10.2208.

[73] B. Khameneh, M. Iranshahy, V. Soheili, and B. S. Fazly Bazzaz, “Review on plant antimicrobials: a mechanistic viewpoint,” *Antimicrobial Resistance & Infection Control 2019 8:1*, vol. 8, no. 1, pp. 1–28, Jul. 2019, doi: 10.1186/S13756-019-0559-6.

[74] S. Roy *et al.*, “Synergistic effects of fresh garlic juice in cellulose based antimicrobial food packaging film,” *Mater Lett*, vol. 324, Oct. 2022, doi: 10.1016/J.MATLET.2022.132538.